Multipacting Electron Guns: Development and Results of a Test Setup for Experimental Characterisation Studies

Dissertation
zur Erlangung des Doktorgrades
an der Fakultät für Mathematik, Informatik und Naturwissenschaften
Fachbereich Physik
der Universität Hamburg

vorgelegt von

Christian Henkel

Hamburg

2021

Gutachter der Dissertation:	Prof. Dr. Wolfgang Hillert Dr. Klaus Flöttmann
Zusammensetzung der Prüfungskommission:	Prof. Dr. Daniela Pfannkuche Prof. Dr. Wolfgang Hillert Dr. Klaus Flöttmann Dr. Velizar Miltchev Prof. Dr. Robert Blick
Vorsitzende(r) der Prüfungskommission:	Prof. Dr. Daniela Pfannkuche
Datum der Disputation:	25.06.2021
Vorsitzender Fach-Promotionsausschuss PHYSIK:	Prof. Dr. Wolfgang Hansen
Leiter des Fachbereichs Physik:	Prof. Dr. Günter H. W. Sigl
Dekan der Fakultät MIN:	Prof. Dr. Heinrich Graener

Abstract Multipacting electron guns (MEGs) are micro-pulsed free electron sources based on periodically enhanced secondary emission inside a resonant microwave cavity. They controllably produce electron bunches in both, pulsed or continuous wave operation, whereby a stationary state of emission is achieved from the self-contained balance between energy gain and beam loading of the resonator.

This thesis presents the development process of a self-constructed test setup for experimental performance studies with a modular gun cavity operated at 2.998 GHz. With help of numerical particle tracking studies and field solver solutions the cornerstones of theoretically quantified design criteria in regards to the resonance condition are found. Charge collection measurements from our tailor-made MEG demonstrate the feasibility of current generation for cathode distances of 0.65 mm to 1.75 mm. Since the design of experiment also provides the option of other structural setup modifications, several parameter studies are performed to derive their dependencies on the multipacting process. It is found that average output currents of up to 278 μA can be achieved at the maximally adjustable cathode distance. The coupling strength of external power supply has a major influence on both, the multipacting onset and also the steady state resonance condition. Furthermore, the longitudinal energy spectrum of the beam is shifted towards higher energies with larger field gradients in a range of $\sim$100 eV. Measurements involving aluminium, copper and stainless steel as cathode materials show different emission behaviour, but all of them are suitable for stable MEG operation.

Zusammenfassung Multipacting Elektronenkanonen (MEGs) sind gepulste Elektronenquellen, die auf periodischer Sekundärelektronenvervielfachung in einem Hohlraumresonator basieren. In gepulstem oder Durchgangsbetrieb werden dabei kontinuierlich Elektronenpakete generiert, was durch externe Energiezufuhr zur Beschleunigung und interne Energieabfuhr durch die Last der Aufladung des Resonators geregelt ist.

In dieser Doktorarbeit werden die Arbeitsprozesse eines selbstentwickelten Aufbaus zu experimentellen Studien mit einem modular zusammengefügten Resonator präsentiert, der bei 2.998 GHz arbeitet. Designkriterien in Bezug auf die Resonanzbedingung sind mit Hilfe numerischer Simulationen zu Teilchenverfolgung und Feldverteilungen ermittelt worden. Messungen mit unserer maßgeschneiderten MEG zeigen Stromentwicklung für Kathodenentfernungen von 0,65 mm bis 1,75 mm. Weil die Versuchsplanung auch andere strukturelle Modifikationen erlaubt, wurden weitere Parameterstudien zum Verständnis des Multipactingprozesses durchgeführt. Es konnten gemittelte Elektronenströme von bis zu 278 μA bei größtmöglicher Kathodenentfernung gemessen werden, wobei insbesondere die Kopplungsstärke externer Energieversorgung einen hohen Einfluss, sowohl auf das Einsetzen von Multipacting als auch auf die stationäre Resonanzbedingung hat. Des Weiteren wurde beobachtet, dass sich mit höheren Feldgradienten auch die longitudinale Energieverteilung der Strahlpakete um bis zu $\sim$100 eV verschiebt. Messungen, die Aluminium, Kupfer und Stahl als Kathodenmaterial beinhalten, weisen zwar auf unterschiedliche Emissionseigenschaften hin, zeigen jedoch grunsätzlich Eignung für stabilen MEG Betrieb.

I would rather have questions that can't be answered than answers that can't be questioned.

– Richard P. Feynman

Contents

List of Figures

List of Tables

1 Introduction

This work is dedicated to the development and understanding of a free electron source based on the effect of resonant secondary emission. It is the amplification process of an electric current between two cold surfaces, where an oscillating electron cloud generates increasing numbers of secondary electrons in vacuum and under the influence of a time-harmonic external field. This method was first described by Farnsworth [1] in 1934, called *Secondary Electron Multipaction*. In 1969, Gallagher [2] proposed the application of a pulsed electron gun for particle accelerators specifically by using the effect of resonant multipacting.

A particle accelerator is a machine that transfers kinetic energy to charged particles like protons, electrons or ions by use of electromagnetic fields [3]. From the first officially called electrostatic accelerator, developed by Wilhelm Conrad Röntgen in 1895 for the creation of X-rays [4], particle accelerators underwent a constant development in technology and scientific advance [5, 6]. Nowadays, their great usefulness lies in the production of high-energy particle beams for e.g. collision experiments [7], the generation of hard X-ray radiation for photon science [8], or applications in medical radiotherapy [9]. Recent development thereby aims for high-brightness beams and large current densities [10]. Numerous other applications in research and technology, like material treatment or processing [11], require accelerated electron beams as well and therefore a source of particles as a central piece of them.

Electron generation can generally be provided by very specific sources based on various emission mechanisms involving heat, particle irradiation, or strong electric fields [12]. A description of the different underlying principles, together with basic design considerations for guns, is given in Chapter 2. However, the novel concept of multipacting for use in micro-pulse electron guns was re-addressed in the early 1990's, primarily by work from Mako, Peter and Len [13]. By the beginning of the 21st century they were able to generate average beam current densities of over $20\,\mathrm{A/cm^2}$ [14] with possible application in high-power klystrons, which was further pursued in more recent times [15]. Separate development in the field of multipacting electron guns (MEGs) has been started in 2013 at the Chinese Academy of Science [16]. Their experimental research indicates successful gun operation including a long lifetime and stable working conditions. Thereby, early characterisation studies of generated beams, regarding an average output current of about $1\,\mathrm{mA}$ with $10\,\mu\mathrm{s}$ RF pulses, could be performed at lifetimes over 360 minutes [17]. Further investigation of the MEG concept suggests a promising way in leading towards a reliable and easily accessible technology for micro-pulse electron beam generation of sufficient bunch charge and with high repetition rate.

From a constructional point of view the key component always consists of a metallic RF (radio-frequency) cavity, which enables energy transfer as well as the required geometrical conditions for the mechanism of resonant electron generation. A basic theoretical introduction of RF resonators and wave propagation is therefore given in Chapter 3, also considering the effects of electromagnetic fields on the motion of charged particles in general. To achieve steady state multipacting, and hence a continuously pulsed electron beam, newly created electrons have to fulfil resonance criteria synchronous to the external RF field between two emission surfaces. The so-called resonance condition is derived for a single particle, as well as for an electron cloud including internal space charge forces, in Chapter 4. Since the motion of electrons in a many-particle system and their effect on secondary emission can only be roughly estimated by analytical calculation, assisting particle tracking simulations were performed. The respective results in Chapter 5 verify the feasibility of an MEG numerically and describe a starting point for the design and construction of our tailor-made RF cavity, which is presented in Chapter 6 alongside a detailed description of the experimental procedure. Numerous iterations of design parameter studies and setup refinements resulted in a modular test stand for MEG performance measurements. In Chapter 7, the experimental results involving two specific cavity designs are presented. One prototype and an improved gun cavity, which acts as the basis of most empirical findings. Special consideration is thereby given to the average beam current and its longitudinal energy distribution with respect to the multipacting resonant condition in a variety of different adjustable measurement configurations. The MEG test setup could effectively be investigated in both, pulsed mode and continuous-wave operation involving three different cathode materials.

Besides the findings from our beginning efforts presented here, this work is supposed to encourage the general understanding and to give a starting point for future development of improved MEG designs and material related investigation, which might lead to applications in accelerator physics, or contribute to other fields of science.

2 Electron Sources for Particle Acceleration

For a classification of multipacting electron guns within the scope of this work, the following chapter introduces electron sources as one of the major components of electron guns in general. Furthermore, an overview and the physical phenomena of different types of sources based on various electron emission mechanisms are discussed. Great significance is dedicated to the principle of secondary electron emission, since it is the primary operating mechanism used in multipacting electron guns.

2.1 Generation of Free Electrons

Before a particle beam is injected into the accelerating structures of an accelerator, there must generally be some sort of particle source involving a specific generation mechanism. Since this work aims to present the development and characteristics of an electron gun for this purpose specifically, further discussion will mostly concern the physics of electrons as the charged particle of choice.

2.1.1 Work Function

The general concepts of free electron generation can only be explained in the context of surface electronic structure. For an electron to escape out of a bound state in given material, it needs to overcome its ionisation potential, often called work function ϕ. It is defined as the difference in potential energy of an electron between the vacuum and Fermi level [18], named E_0 and E_F, resulting in

$$\phi = -E_\mathrm{F} + E_0. \tag{2.1}$$

Figure 2.1 shows an illustration of the crystal potential, which is created by the electric charge density of the nearby crystal structure, close to a metal surface. The Fermi level E_F is the highest occupied electronic state inside the metal and equals the electrochemical potential μ

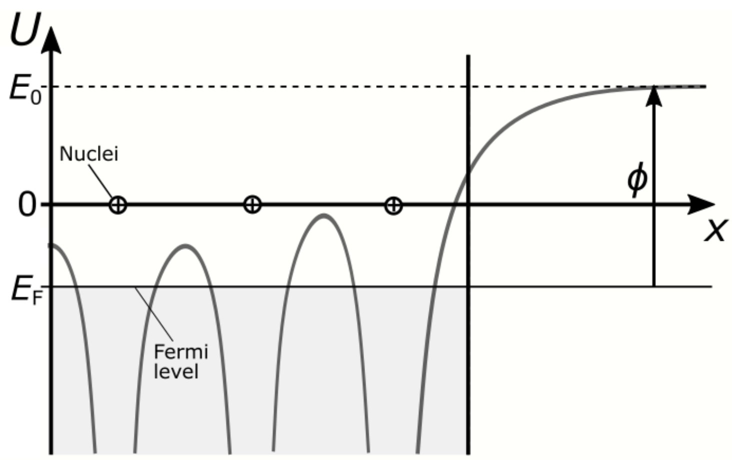

Figure 2.1: Electrostatic crystal potential U at the metallic surface inside (left) and outside (right) of the material. Figure made in consideration with [19] and [20].

[18]. In addition to E_F, also the energy difference to the vacuum level E_0 is needed to carry an electron through the electric field into the lowest level outside the material, where there is no interaction between both any more [19]. In that context, E_0 corresponds to the surface dipole potential [20]. The work function is typically in the order of 2 - 5 eV (1 eV = 1.602×10^{-19} J) and depends heavily on the kind of material and orientation of the exposed crystal face. A comprehensive list of important ϕ-values can be found in [21] for example.

2.2 Emission Mechanisms for Electron Guns

There are several mechanisms, that deliver a significant amount of energy to a number of electrons for them to be emitted. A schematic representation is given in Figure 2.2. It covers the primary stimuli for electron emission based on the already introduced model of the electrostatic surface potential and work function from Section 2.1.1. In the following overview including different electron emission schemes, they are divided into five distinct categories:

- **Thermionic Emission** (Emission after thermal energy transfer by heat)
- **Field Emission** (Quantum tunnelling through an external field induced potential barrier)
- **Photoemission** (Electron excitation and emission by photon absorption)
- **Schottky Emission** (Intermediate effect of electron excitation and barrier lowering)
- **Secondary Emission** (Emission after kinetic impact of electrons or ions)

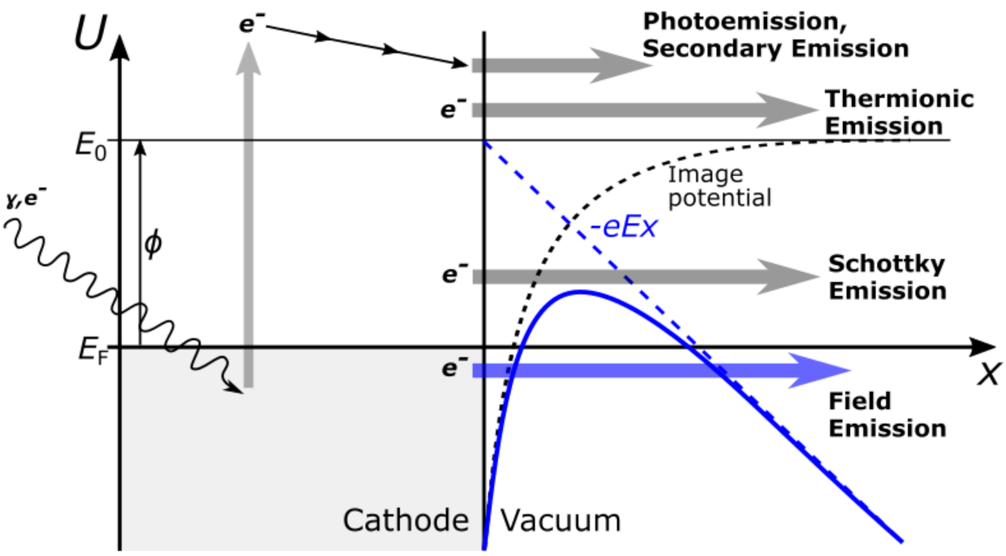

Figure 2.2: Stimulated electron emission mechanisms for an arbitrary cathode material, including the changed form of the potential barrier by application of a strong electric field E in blue. Figure made with regards to [22], combined with [23].

2.2.1 Thermionic Emission

In the case of thermionic emission a number of electrons gain sufficient thermal energy to overcome the work function. Theoretical descriptions are based on the electron distribution over energy states following Fermi-Dirac statistics, together with the principles of thermodynamics [24]. The amount ot charge flow per unit time and area (current density J_{th}) for thermionic emission of electrons is represented by

$$J_{\mathrm{th}} = AT^2 e^{-\phi/k_{\mathrm{B}}T}, \tag{2.2}$$

known as the Richardson-Dushman equation [25, 26]. It depends on the applied temperature T in Kelvin, the material work function ϕ and the Boltzmann constant $k_{\mathrm{B}} = 8.6175 \times 10^{-5}\,\mathrm{eV/K}$. The theoretical emission constant A is given by

$$A = \frac{4\pi e m_{\mathrm{e}} k_{\mathrm{B}}^2}{h^3} = 1.2 \times 10^6 \mathrm{Am^{-2}K^{-2}}, \tag{2.3}$$

with $e = 1.602 \times 10^{-19}\mathrm{C}$ and $m_{\mathrm{e}} = 9.11 \times 10^{-31}\mathrm{kg}$, being the electron charge and rest mass, together with the Planck constant $h = 6.63 \times 10^{-34}\mathrm{Js}$ [27].

The conceptual approach of electron guns in general can already be introduced by the technologically simple concept of a planar diode configuration with thermionic emitter as the particle source. Figure 2.3 shows an appropriate illustration of the setup schematically. A potential difference between two electrodes accelerates the constantly emitted electrons from the cathode side towards the anode. There, a hole or mesh allows the electron beam to propagate into the drift region and further accelerating structures of given machine. The emitting material is heated to high temperature $T > 1200\,°\mathrm{C}$ and therefore requires a high resistance to heat and a low work function for long term operation with large current output [22, 27]. Because of the

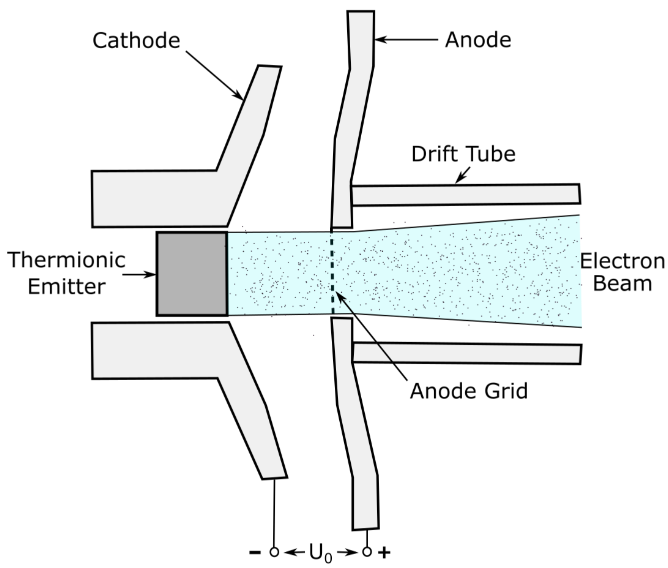

Figure 2.3: Electron gun with thermionic emitter and DC voltage gap, analogue to [27].

continuous nature of emission, electrons cannot easily be gated to a particular fraction of an RF period and therefore the gun suffers from degraded beam quality [28]. Limitations in efficiency are mainly induced by the electric self-fields from the emitted electron distribution, which will be covered in Chapter 4.2.3 with more detail.

2.2.2 Field Electron Emission

Field electron emission is the emission of electrons by application of a high electric field ($10^3 - 10^4 \mathrm{V}/\mu\mathrm{m}$) to the cathode surface [23]. It is the fundamental principle leading towards the development of the field electron microscope (FEM) in 1937 [29], for instance. Theoretical descriptions are based on the Fowler-Nordheim (FN) model [30], published in 1928. An external electric field thereby shrinks the electrostatic potential barrier at the emitter surface, indicated by the blue line in Figure 2.2, and enables the possibility of quantum tunnelling from the filled states on Fermi-level E_F into vacuum. One of the core assumptions of the FN theory is a triangular shape of the barrier. A detailed derivation of this method can be found in [23], amongst other theories for the analytical description of field emission.

Similar to thermionic emission, electrons that escape into vacuum are creating a charge density J. In the case of field emission after definition of Fowler and Nordheim, J can be expressed by

$$J_\mathrm{FN} = a_\mathrm{FN} \frac{E^2}{\phi} \exp\left(-\frac{b_\mathrm{FN}\phi^{3/2}}{E}\right), \tag{2.4}$$

with the FN field emission parameters

$$a_\mathrm{FN} = \frac{e^3}{16\pi^2\hbar} \approx 1.5414\ \frac{\mu\mathrm{A\,eV}}{\mathrm{V}^2}; \tag{2.5a}$$

$$b_\mathrm{FN} = \frac{4}{3}\frac{(2m_\mathrm{e})^{1/2}}{e\hbar} \approx 6.83089\ \frac{\mathrm{V}}{\mathrm{eV}^{-3/2}\,\mathrm{nm}}. \tag{2.5b}$$

The charge distribution of equilibrium states can be locally enhanced at the tip of geometrical features or defects on the material surface, when a macroscopic electric field E_M is applied [23]. Here, E stands for the locally increased electric field, including the field enhancement factor γ:

$$E = \gamma E_\mathrm{M} \tag{2.6}$$

According to [23], Eq. (2.4) is a sufficient but rough approximation of the current density J_FN, not including the image potential effect near the material surface. Therefore, the effective potential barrier has to change due to the presence of a mirror charge potential [31] and it is written as

$$U(x) = \phi - eEx - \frac{e^2}{16\pi\varepsilon_0 x}, \tag{2.7}$$

where $-eEx$ is the external field potential and $e^2/16\pi\varepsilon_0 x$ is the potential induced by image charges.

For a more precise description the Schottky-Nordheim (SN) model must be considered, which is supported by the numerical calculation of two correction factors ν_F and τ_F from dimensionless elliptical functions [32]. As a consequence, for a generalized triangular potential barrier as given by Eq. (2.7) and represented by the solid blue line in Figure 2.2 at the cathode surface, the charge density of electron emission then yields

$$J_\mathrm{SN} = a_\mathrm{FN}\tau_\mathrm{F}^{-2}\frac{E^2}{\phi}\exp\left(-\nu_\mathrm{F}\frac{b_\mathrm{FN}\phi^{3/2}}{E}\right). \tag{2.8}$$

With field electron guns the emitter is biased to its surroundings by a high-field gradient in a time-harmonic manner indicated by Figure 2.4. Electron emission will thus be symmetric around phase $\varphi = \pi$, where the threshold field is provided. Although the emission occurs periodic and bunched electron beams can be generated directly at the cathode, contrary to thermionic emitters, the resulting beam will typically have a large energy spread and poor transverse quality [28] due to the time-varying expression of emission probabilities within one RF period. This is unfavourable for most fields of application.

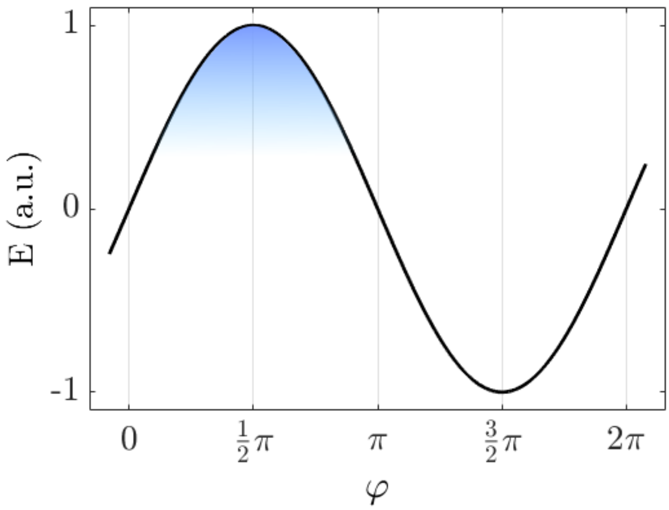

Figure 2.4: Time-harmonic electric field E as a function of the phase $\varphi = \omega t$. The probability of field emission within one RF period is indicated by an arbitrary threshold field strength in blue.

A major disadvantage of high-field gradients in general, necessary for beam acceleration, is the production of dark current due to field emission. This is especially significant in photocathode RF guns [33]. In the presence of a strong RF field gradient with regard to Figure 2.4, field electrons are preferably accelerated in forward direction. According to [34], the time-averaged emission current $\bar{I}_\mathrm{SN}$ in a macroscopic electric field of the form $E_\mathrm{M}\cdot\sin(\omega t)$, where E is the localised field strength, can be derived by time integration of Eq. (2.8) over the period T of one

RF cycle, following:

$$
\begin{aligned}
\bar{I}_{\mathrm{SN}} &= \frac{1}{T}\int_0^T A_{\mathrm{eff}} J_{\mathrm{SN}}(t)\,dt \\
&= \frac{1}{T}\int_0^T a_{\mathrm{FN}} \tau_{\mathrm{F}}^{-2} \frac{A_{\mathrm{eff}} E^2}{\phi} \exp\left(-\nu_{\mathrm{F}} \frac{b_{\mathrm{FN}} \phi^{3/2}}{E}\right) dt \\
&= \frac{1.54 \times 10^{-6} A_{\mathrm{eff}} E^2 \times 10^{4.52\phi^{-1/2}}}{\phi} \frac{2}{T} \int_0^{\frac{T}{4}} \sin^2 \omega t \exp\left(-\frac{6.53 \times 10^9 \phi^{3/2}}{E \cdot \sin \omega t}\right) dt \\
&= \frac{5.7 \times 10^{-12} \times 10^{4.52\phi^{-1/2}} A_{\mathrm{eff}} E^{5/2}}{\phi^{7/4}} \exp\left(-\frac{6.53 \times 10^9 \phi^{3/2}}{E}\right) \quad \text{Ampere}
\end{aligned}
\tag{2.9}
$$

It has to be mentioned that τ_{F} and ν_{F} have been substituted by 1 and $10^{4.52\phi^{-1/2}}$, respectively [34]. Also it is assumed that there is an effective area A_{eff}, where the emission of electrons occurs.

2.2.3 Photoemission

One of the two emission mechanisms, that include electron generation by the impact of external particles, is photoemission. Thereby, electromagnetic radiation shines onto the material surface and it may excite some of the electrons to sufficiently high energy, so that they are able to escape [35]. The mechanism behind it is well known as the photoelectric effect, initially interpreted by Einstein in 1905 [36].

More specifically, after the photo excitation of an electron by a photon of defined energy, the electron migrates to a higher-energy state and may diffuse randomly through the crystal lattice towards the surface [35]. From an number of collisions it thereby looses energy, which is pronounced differently for metals and semiconductors. Contrary to non-metallic materials, in metal, any optically excited electrons can suffer electron-electron scattering because of the presence of free electrons. For semiconductors, a finite band gap E_{g} separates the highest filled states in the valence band (VB) and the energetically lowest states in the conduction

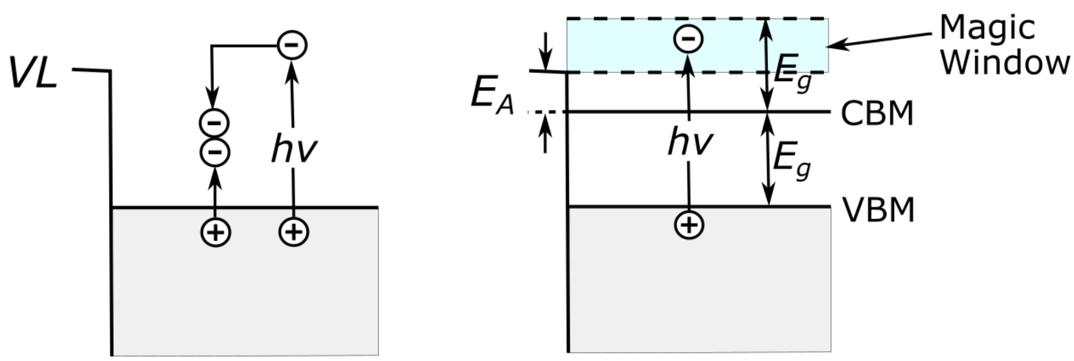

(a) Metal (b) Semiconductor

Figure 2.5: Optical electron excitation within the band structure of metals (a) and semiconductors (b) in comparison. Figure made in accordance with [37].

band (CB), like shown in Figure 2.5 [37]. There, one electron must have gained an energy of at least E_g above the CB for the creation of electron-hole pairs, which is forbidden for photon energies $h\nu < 2E_g$ [38]. If their energy falls into the region between $E_g + E_A$ and $2E_g$, whereby E_A is the electron affinity, there is sufficient momentum to escape, but not enough to create electron-hole pairs and photoemission becomes more likely. Within that "Magic Window", electrons loose their energy mainly due to phonon scattering, which generally has a minor influence on their kinetic energy [37]. Although metals are no efficient photoemitters, an escape of excited electrons into vacuum is still possible, if sufficient energy remains to overcome the work function. This is also briefly indicated in the overview graphic from Figure 2.2. The initial energy, which is absorbed by the excited electron, equals the photon energy:

$$E_{ph} = h\nu. \tag{2.10}$$

It depends on the photonic frequency ν and the Planck constant h. However, only a small fraction of electrons per incident photon is emitted because of light reflection at the surface and the above mentioned energy loss process of the excited electrons, that undergo pair-production. The number of emitted electrons per absorbed photon is called quantum efficiency (QE) and is highly material dependent [6], since the bulk absorption coefficient governs the excitation of photoelectrons [37]. A heuristic estimate of QE for photons of energy $h\nu$ is given by

$$QE = \frac{\frac{\alpha_{PE}}{\alpha} P_E}{1 + \frac{l_a}{L}}, \tag{2.11}$$

where $l_a = \frac{1}{\alpha}$ is the absorption length, L is the scattering length, and $\frac{\alpha_{PE}}{\alpha}$ is the fraction of electrons, which are excited above the vacuum level. Furthermore, P_E is the escape probability of electrons with sufficient energy, when reaching the surface. All these variables are functions of $h\nu$, leading to an estimate of the photoemission current due to incident light irradiation of intensity I_0, that is:

$$I_{ph} = I_0(1-R)\left[\frac{\frac{\alpha_{PE}}{\alpha} P_E}{1 + \frac{l_a}{L}}\right] = I_0(1-R) \times QE, \tag{2.12}$$

including the surface light reflectivity $R(h\nu)$. A detailed derivation of Eqs. (2.11) and (2.12) can be found in [37].

When the photo effect is used to create a bunched beam for electron guns, the emitter, here called photocathode, is irradiated by a focused laser beam of high-power [27]. This concept was first developed in Los Alamos in 1985 [39] and remains a state-of-the-art technology in large accelerator laboratories around the world [40]. A schematic drawing of such a gun is illustrated in Figure 2.6 exemplarily. Strong axial fields in the cavity cells of up to 100 MV/m [41] accelerate the electrons to high-energy ($\gtrsim$ 1 MeV) rapidly. Timing and length of the laser pulse are chosen to produce short electron bunches within the accelerating part of the RF cycle for high-brightness beams, which are of particular interest for advanced accelerator applications

[27]. For the photocathode, semiconducting substrates with high quantum yield, like caesium telluride (Ce_2Te), are widely used for their overall efficiency and ruggedness [42].

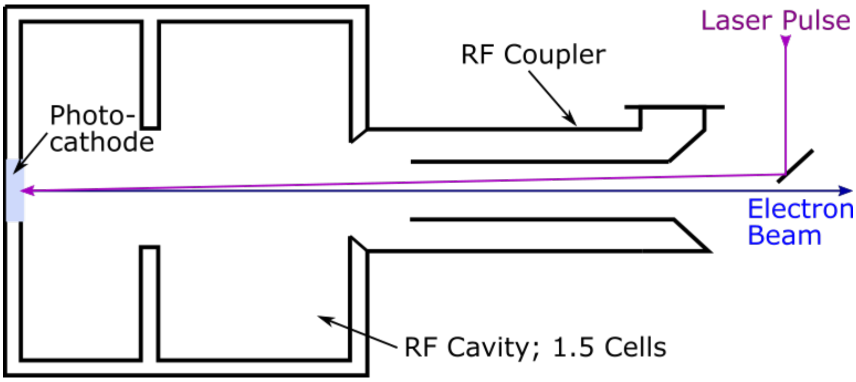

Figure 2.6: Electron gun with photo emitter inside a 1.5 cell RF cavity structure. The gun cavity is a significant simplification of the electron gun at the photoinjector test facility at DESY, Zeuthen site (PITZ), from [43, 44].

2.2.4 Schottky Emission

In the intermediate region in Figure 2.2, where thermionic emission is assisted by a decrease of the vacuum potential barrier, electron generation is governed by the Schottky effect [45]. As a consequence of temperature and field influences, Eq. (2.2) then translates into

$$J_{\text{th}} = AT^2 e^{-(\phi-\phi_\text{s})/k_\text{B}T}, \tag{2.13}$$

where ϕ_s is the reduction of the work function due to barrier lowering, which is quantified by $\phi_\text{s} = 0.012\sqrt{E_\text{M}}$ in units of V/cm [6].

Not only temperature, but also excitation with photons can lead to Schottky-enabled emission of electrons [46]. At its threshold for photoemission, the difference between work function ϕ and photon energy $h\nu$ equals the Schottky potential and can be written as

$$h\nu \approx \phi - \sqrt{4\pi\varepsilon_0 e^3 E}, \tag{2.14}$$

where E is the localised field after Eq. (2.6), ε_0 is the vacuum permittivity, and e is the electron charge [46, 47]. At this point it is pointed out that the application of strong electric fields contributes to the appearance of electron emission in a variety of charge generation mechanisms.

2.2.5 Secondary Emission

The second of two electron emission mechanisms involving particle irradiation, particularly including charged particles, is called secondary emission (SE) [48]. First reports on this phenomenon were authored in 1902 by Austin and Starke [49] after the observation of a higher number of reflected electrons from a metal surface, compared to the incident beam. In fact, more than one secondary electron can be generated per incident ”primary” electron under certain circumstances. This chapter focuses on the excitation and emission of electrons by the bombardment and interaction with other electrons, which is very different to the case of ion bombardment [48]. Electrons, similarly to photons, penetrate much deeper into the material bulk, whereas ions rather induce surface effects, when not reflected. However, when we speak about secondary emission, there are three underlying processes responsible for the three types of SE electrons as shown in Figure 2.7 [50].

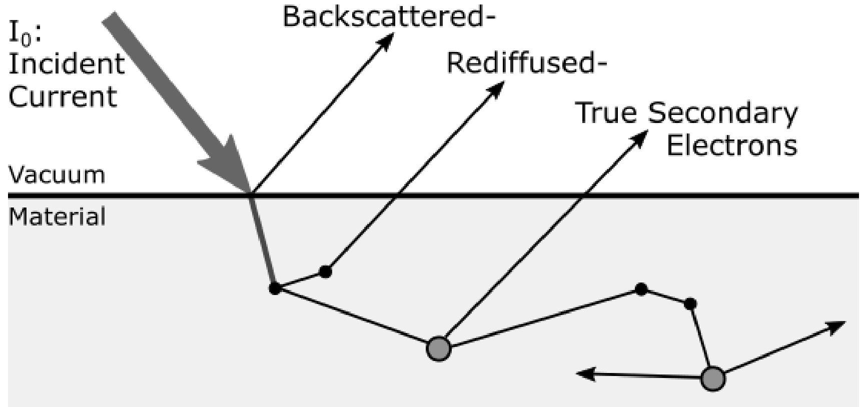

Figure 2.7: Interaction scheme of secondary electron generation including three different types of effects. The grey circles shall indicate interaction regions of true secondary electron creation, whereas dots represent interaction with the atomic crystal lattice.

(a) **Backscattered electrons** are not truly of secondary nature, since they are reflected elastically from the material surface.

(b) **Rediffused electrons** are the ones, that penetrate into the material and scatter from one or more atoms before they are reflected back out. They are termed SE electrons, but loose energy due to electron-phonon scattering without the generation of new particles.

(c) **True secondary electrons** are in fact created through inelastic electron-electron scattering by incident primary electrons in a more complicated way. Thereby, more than one SE electron can be generated if sufficient energy is available for the creation of more than one electron-hole pair.

All types of these electrons may contribute to the amount of the total emission current differently for different primary electron energy Σ [50]. For a multipacting gun, whose performance is heavily determined by its SE properties, Σ is tailored around a few tens to hundreds eV, based on the type of cathode material. Hence, it is expected that the SE process is mostly governed by the creation of true secondary electrons in that specific energy region.

Very similar as for the photoelectric effect, true secondary emission can be explained by a three-step model [51]. After the creation of internal secondary electrons by kinetic energy transfer of the primary electrons (1), they are travelling through the material bulk towards the surface (2), and may escape across the vacuum interface (3). The efficiency of secondary emission, in that regard, is described analytically by means of the *Secondary Electron Yield*.

Secondary Electron Yield

In order to describe emission based on secondary electron generation quantitatively in a simple representation, the secondary emission yield (SEY) can be defined by

$$\delta = \frac{I_\mathrm{s}}{I_0}, \tag{2.15}$$

where I_0 is the incident current striking the material surface and I_s is the emitted current of secondary electrons [50]. A yield $\delta > 1$ means that the total number of electrons is increased after interaction with the material. In reality, Eq. (2.15) is a complex function depending on the microscopic material properties, the incident angle of primary electrons and their kinetic energy Σ, as mentioned earlier [51].

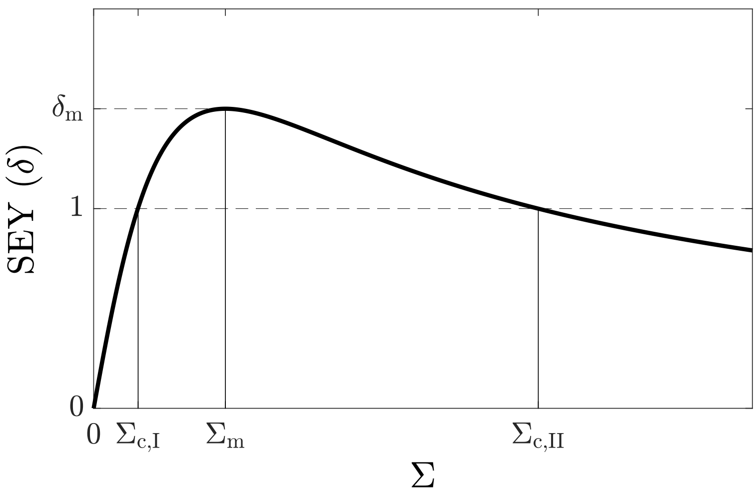

Figure 2.8: Schematic profile of the secondary electron yield δ as a function of the primary electron energy Σ. The height of the curve is determined by the maximum yield δ_m at energy Σ_m. If it exceeds the value of one, there are two cross-over energies $\Sigma_\mathrm{c,I}$ and $\Sigma_\mathrm{c,II}$, enclosing an energy interval, where statistically more electrons are emitted than absorbed. Figure made in accordance to [52].

Figure 2.8 shows a schematic of the typical form of $\delta(\Sigma)$ in the low-energy regime for primary electrons of up to 2 keV. According to experimental data from Baglin *et al.* [53], aluminium shows the highest overall SE yield of $\delta_\mathrm{m}(\Sigma_\mathrm{m} \simeq 370\,\mathrm{eV}) \simeq 3.45$ in comparison to other technical materials without surface treatment. The δ_m-values for titanium, copper (OFHC) and stainless steel revolve around 2, at primary energies from approximately 240 to 300 eV, in the course of their studies. In all cases, $\Sigma_\mathrm{c,I}$ was measured in the sub-100 eV region of Σ.

The shape of these curves is heavily affected by underlying scattering processes inside the material bulk (cf. Figure 2.7) and their spacial distance to the surface [51]. It primarily depends on the rate

$$n(x,\Sigma) = -\frac{1}{\varepsilon}\frac{dE}{ds} \tag{2.16}$$

of secondary electrons generated at a distance x from the surface, along the path s of a primary electron with energy Σ [54]. Thereby, it is assumed that $n(x,\Sigma)$ is proportional to the stopping power $-dE/ds$. The energy required to produce one SE is given by the excitation energy ε. In a first approximation, the energy loss $-dE/ds$ of the primary electron might be seen as constant within the penetration depth R [55], following

$$-\frac{dE}{ds} = \frac{\Sigma}{R}. \tag{2.17}$$

The SEY also depends on the probability $f(x)$ of secondary electrons travelling to the surface from depth x and escaping, given by

$$f(x) = Ae^{-x/\lambda}, \tag{2.18}$$

where λ is the effective escape depth, or mean free path, of an electron and A is a constant $\in [0,1)$ indicating the fraction of secondary electrons transported to the surface [56]. For the yield δ, integration of $n(x,\Sigma)$ and $f(x)$ over the penetration depth R leads to

$$\delta = \int n(x,\Sigma) f(x) dx \tag{2.19a}$$

$$= \int_0^R \frac{A}{\varepsilon}\frac{\Sigma}{R} e^{-x/\lambda} dx$$

$$= A \cdot \frac{\Sigma}{\varepsilon} \cdot \frac{\lambda}{R}(1 - e^{-R/\lambda}). \tag{2.19b}$$

There are slightly different approaches regarding the distance R, a primary electron of low-energy is assumed to penetrate into the bulk, by [51, 54, 56] for instance. However, they all mention a proportionality on R, given by

$$R \propto E_0^{n+1}, \tag{2.20}$$

which would be a direct derivation of the energy loss according to the power law $-dE/ds = B/\Sigma^n$ [51, 52]. Here, B is a constant containing several intrinsic material properties and n is a free parameter found to be 0.35 by [55] through empirical observations. It can be pointed out that the penetration depth of the primary electrons increases with increasing energy. Furthermore, with higher Σ, secondary generation originates deeper inside the bulk. This is even enhanced by an increased generation rate near the end of the primary path due to a longer interaction time, also including a lower particle velocity [51].

Consequently, the behaviour of δ in Figure 2.8 can be explained qualitatively with respect to the penetration depth R and the exponentially decreasing escape probability $f(x)$, including the characteristic escape depth λ, from Eq. (2.18). At low primary energies, for which $R \ll \lambda$, the rate of secondary generation starts low and grows with Σ due to the increasing penetration depth following Eq. (2.20), while the escape probability remains high for the relatively small R/λ-ratio. A maximum is reached when R approximately equals λ and the curve shape decreases in an exponential manner afterwards, since the escape probability falls stronger than the secondary generation rate rises by the greater value of R. In the end, combining Eqs. (2.19b) and (2.20), the curve levels off with a $\Sigma^{-n} \approx \Sigma^{-0.35}$ dependency.

After further elimination of material specific parameters, which is not covered here, a material independent formula describing the general shape of a SEY curve can be deduced, given by

$$\frac{\delta}{\delta_m} = 1.1 \left(\frac{\Sigma}{\Sigma_\mathrm{m}}\right)^{-0.35} \left[1 - \exp\left(-2.3\left(\frac{\Sigma}{\Sigma_\mathrm{m}}\right)^{1.35}\right)\right], \tag{2.21}$$

known as *the universal law for SE yield* [54]. In this expression δ_m is the maximum SEY value, reached at energy Σ_m. With reference to [53] and others, where the measured $\delta(\Sigma)$ for different technical materials is plotted, δ_m and Σ_m are unique for each cathode substrate and its treatment. While aluminium naturally has the highest δ_m compared to the other materials under investigation, its work function $\phi_\mathrm{Al} = 4.28\,\mathrm{eV}$ is small in comparison with copper ($\phi_\mathrm{Cu} = 4.65\,\mathrm{eV}$) for example [21]. Unlike the emission from thermal or field emitters, secondary electrons are influenced by the bulk of conduction band electrons [57]. The high collision probability within the conduction band, as well as with ions and other defects, together with a large minimum escape energy $E_\mathrm{F} + \phi$, results in a short escape depth and thus a small SEY found with metals [51]. In fact, the work function is not a valid indicator for SE properties in general.

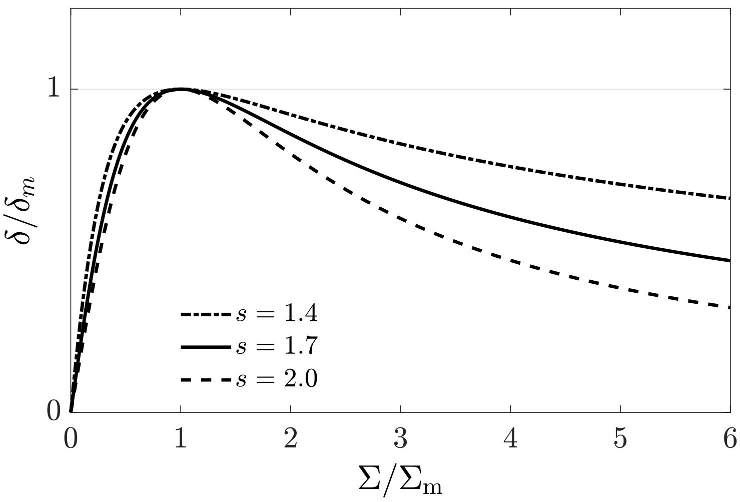

Figure 2.9: Development of the SE yield δ as a function of the primary electron energy Σ, based on Eq. (2.23). While δ_m and Σ_m are influencing the position and height of the global maximum, s defines the overall shape of the curve.

Several numerical models for precise predictions on secondary emission have been established. For this work, the probabilistic model of Furman and Pivi [50] is used, in which the energy and angular dependence of δ are fit semi-empirically by a scaling function

$$D(x) = \frac{sx}{s - 1 + x^s}, \tag{2.22}$$

where s is an adjustable parameter > 1 and $x = \Sigma/\Sigma_\mathrm{m}$, leading to the expression of

$$\delta(\Sigma) = \delta_\mathrm{m} \frac{\Sigma}{\Sigma_\mathrm{m}} \frac{s}{s - 1 + (\Sigma/\Sigma_\mathrm{m})^s} \tag{2.23}$$

for the prediction of the secondary yield. A visual representation is included in Figure 2.9 for a variation of the free fit parameters s.

2.3 Multipacting

The concept of multipacting (multiple electron impacting), or *Secondary Electron Multipaction*, as originally described by Farnsworth [1], essentially is the electric discharge between two surfaces by secondary electrons in the presence of a synchronized RF field [58]. Its appearance in RF components such as couplers, cavity walls, RF windows, or even cathode surfaces in conventional electron guns usually is an undesired effect, that can lead to vacuum breakdown [59], power loss [60], or mechanically damaged components [44].

Key phenomena are the generation of secondary emission at the two cathode surfaces and a resonant charge multiplication process, that sustains itself by phase conservation of the electron cloud around the impact times. Since electrons can thereby induce secondary emission at both surfaces, a condition may exist, where their drift time is a multiple of half an RF cycle and therefore the starting time is recreated for each half-period [58]. This is called resonance condition for multipacting. More specifically, for RF cavities, it can be written as follows [61]:

(1) An electron emitted from the cavity wall is driven by the electromagnetic fields and returns back after an integer number of RF cycles to the same point of the cavity wall;

(2) The impacting electron produces more than one secondary electron.

The latter case requires incident electrons, that must transfer primary energies Σ leading to $\delta > 1$ on average in terms of the yield curve from Figure 2.8. In addition to two-sided multipacting, it is also possible to build up the resonant condition at a single surface with multiple impacts

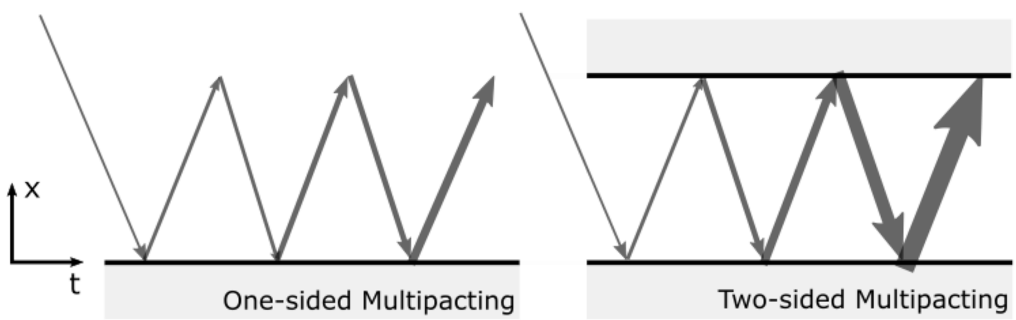

Figure 2.10: Schematic illustration of one-sided (left) and two-sided (right) multipacting at resonance in an alternating electric field of the form $E_\mathrm{rf} = E_\mathrm{rf,0} \cdot \sin(\omega t + \varphi)$. The amount of charge builds up with every impact on one of the surfaces, as indicated by the increasing arrow thickness.

around the same RF phase [62]. Figure 2.10 contrasts both types of multipacting schematically in a simplified geometry with respect to the temporal development in an alternating electric field. Because of repulsive forces from electrons inside the subsequently generated electron cloud of many particles, detailed theoretical description needs the help of computational methods. For single-sided multipacting, numerical particle tracking studies have been performed regarding its presence in photocathode RF guns [44, 63]. However, this work focuses on two-sided multipacting for its application in MEGs and is conceptually introduced in the following.

2.3.1 MEG Principle

Based on early experiments by Gallagher [2], multipacting discharge between two opposing surfaces can be used for the controllable generation of bunched electron beams. Thereby, the electron cloud oscillates inside a parallel plate configuration of the two cathodes with secondary yield $\delta_i > 1$, driven by the RF field, which is coupled into the surrounding cavity. A schematic illustration is presented in Figure 2.11.

The effect sustains itself by periodically enhanced secondary emission every half-cycle of the electric field around the synchronous phase of the electrons, as further described in Chapter 4.1. Steady state operation can be achieved, which is a result of cavity loading and space charge debunching of the electron cloud [58, 64]. Although space charge forces have an impact on the kinetic energy distribution of the particles, a self-bunching effect due to natural phase selection of the particles leads to small bunch sizes of the resulting beam [65]. In order to release a bunched electron beam from the gun cavity, one partially transparent cathode surface is used for the beam to pass through.

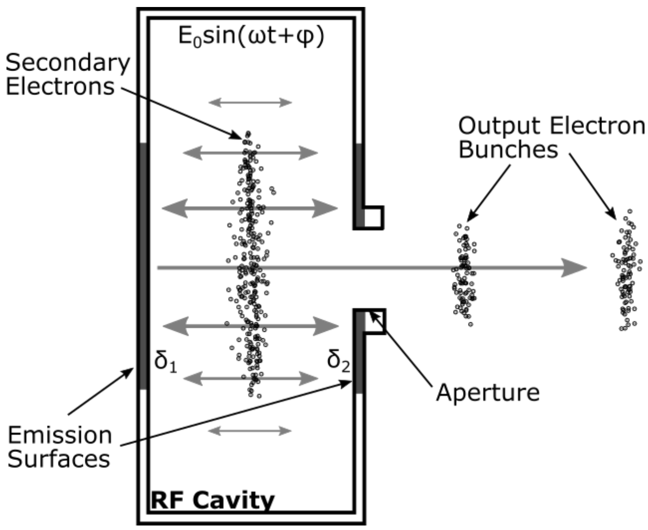

Figure 2.11: MEG principle.

The following chapters give a comprehensive theoretical background of the single-particle description of electron motion leading towards MEG operation and introduce the many-particle system for its importance in the understanding of numerical and experimental studies, presented in this work.

3 Charged Particle Acceleration and RF Structures

Interaction of charged particles, such as electrons, with electromagnetic fields is the primary topic of accelerator physics. Also, the driving mechanism behind the operation of an MEG lies in the acceleration of electrons inside of an RF cavity. Therefore, this chapter is about the basic theory of charged particles under the influence of electromagnetic fields in free space and RF waveguides. Furthermore, the mutual interaction of free charge carriers and the cavity itself plays an important role and therefore resonator theory will be covered in detail.

3.1 Motion of Charged Particles in Electromagnetic Fields

Since the particle motion in vacuum is mostly affected by electric and magnetic fields, their behaviour is governed by Maxwell's equations [66]:

$$\nabla \cdot \mathbf{E} = \rho/\varepsilon_0 \qquad \text{Coulomb's law} \tag{3.1a}$$

$$\nabla \times \mathbf{B} - \frac{\partial \mathbf{E}}{c^2 \partial t} = \mu_0 \mathbf{J} \qquad \text{Ampère's law} \tag{3.1b}$$

$$\nabla \times \mathbf{E} - \frac{\partial \mathbf{B}}{\partial t} = 0 \qquad \text{Faraday's law} \tag{3.1c}$$

$$\nabla \cdot \mathbf{B} = 0 \tag{3.1d}$$

Here, ε_0 and μ_0 are the vacuum permittivity and permeability, respectively. They are related to c, the speed of light in free space, by $c = \sqrt{1/\varepsilon_0 \mu_0}$. $\mathbf{E}$ and $\mathbf{B}$ are the time-dependent electric and magnetic field vectors. The continuity equation is implicitly satisfied by the current $\mathbf{J}$ and the space charge density ρ, such that

$$\frac{\partial \rho}{\partial t} + \nabla \cdot \mathbf{J} = 0. \tag{3.2}$$

Integration of Maxwell's equations leads to an expression for the fields of given charged particles or beams. Comprehensive derivation would exceed the scope of this work, thus [67] is referenced, giving an in-depth insight into charged beam dynamics from a general point of view.

3.1.1 Lorentz Force

In an electromagnetic field, the motion of a charged particle is only influenced by the Lorentz force $\mathbf{F}_\mathrm{L}$. Its trajectory can be determined in a classical form with Newton's equation of motion, written as

$$\frac{d\mathbf{p}}{dt} = \mathbf{F}_\mathrm{L} = q(\mathbf{E} + \mathbf{v} \times \mathbf{B}), \tag{3.3}$$

where $\mathbf{p}$ is the momentum, $\mathbf{v}$ is the velocity and q is the amount of charge carried by the particle. This force equation is also correct for velocities close to the speed of light, where $\mathbf{p} = m\mathbf{v}$

translates into

$$\mathbf{p} = \frac{m\mathbf{v}}{\sqrt{1-\beta^2}} = \gamma m\mathbf{v} \tag{3.4}$$

after transformation of the reference system according to the theory of special relativity [27]. Here, γ is known as the *Lorentz factor* depending on $\beta = v/c$, the particle velocity to speed of light ratio, and m denotes the particles rest mass.

At this point, however, it is to be mentioned that particle motion is generally affected by the direction of the Lorentz force with respect to the velocity vector $\mathbf{v}$, specifically in case of highly relativistic particles. Using Eq. (3.4), the equation of motion for a particle in an electromagnetic field yields

$$\frac{d\mathbf{p}}{dt} = \frac{d(\gamma m\mathbf{v})}{dt} = m\gamma\frac{d\mathbf{v}}{dt} + m\mathbf{v}\frac{d\gamma}{dt} = m\left(\gamma\frac{d\mathbf{v}}{dt} + \gamma^3\frac{\beta}{c}\frac{dv}{dt}\mathbf{v}\right), \tag{3.5}$$

hence for the two extreme cases $\mathbf{F}_\mathrm{L} \parallel \mathbf{v}$ ($\dot{v}\mathbf{v} = v\dot{\mathbf{v}}$) and $\mathbf{F}_\mathrm{L} \perp \mathbf{v}$ ($dv/dt = 0$), the motion can be described by [67]:

$$\frac{d\mathbf{p}_\parallel}{dt} = m\gamma^3\frac{d\mathbf{v}_\parallel}{dt}, \tag{3.6a}$$

$$\frac{d\mathbf{p}_\perp}{dt} = m\gamma\frac{d\mathbf{v}_\perp}{dt}. \tag{3.6b}$$

For its complexity in changing coordinate systems, the above mentioned Newtonian equations are often supplemented by a Lagrangian function $L(q_i, \dot{q}_i, t)$ of generalised coordinates q_i and velocities $\dot{q}_i$ leading to equations of motion, independent of the system. A review of the Lagrangian and Hamilton formalism can be found in [27] or [66] for instance.

3.1.2 Energy Gain

As in conventional accelerating cavity structures from linear or circular machines for example, acceleration is always due to particles gaining kinetic energy by external forces. For a particle under the respective presence of a non-zero $\mathbf{E}$- and $\mathbf{B}$-field, integration of Eq. (3.3) over the distance from a generic point $\mathbf{r}_1$ to $\mathbf{r}_2$ gives the change in kinetic energy ΔE_kin following

$$\begin{aligned} \Delta E_\mathrm{kin} &= \int_{\mathbf{r}_1}^{\mathbf{r}_2} \mathbf{F}_\mathrm{L}\, d\mathbf{r} = q\int_{\mathbf{r}_1}^{\mathbf{r}_2} [\mathbf{E} + (\mathbf{v}\times\mathbf{B})]\, d\mathbf{r} \\ &= q\int_{\mathbf{r}_1}^{\mathbf{r}_2} \mathbf{E}\, d\mathbf{r} + q\int_{\mathbf{r}_1}^{\mathbf{r}_2} \underbrace{(\mathbf{v}\times\mathbf{B})\, d\mathbf{r}}_{=0} \\ &= qU. \end{aligned} \tag{3.7}$$

Since the path element $d\mathbf{r}$ is parallel to the velocity vector $\mathbf{v}$ at all times, the magnetic field does not influence the absolute energy value. It may nevertheless deflect the particles trajectory to another direction, when $\mathbf{B}$ and $\mathbf{v}$ are not parallel to each other according to the vector product in Eq. (3.3). However, an increase in kinetic energy leading to straight-line acceleration is only due to the electric field $\mathbf{E}$, with $U = \phi_1 - \phi_2$ being the electrostatic potential difference between the two points $\mathbf{r}_1$ and $\mathbf{r}_2$, also called voltage [68]. In a system, where **E** and **B** are not explicitly time-dependent, the Lorentz force is conservative and the equation of motion in terms of total energy $E_{\mathrm{tot}} = \gamma mc^2$ is given by [27]:

$$\frac{dE_{\mathrm{tot}}}{dt} = \frac{d\mathbf{p}}{dt} \cdot \mathbf{v} = q\mathbf{E} \cdot \mathbf{v}. \tag{3.8}$$

3.2 RF Waveguides

Not only MEGs in the context of this work, but also most of the modern accelerator machines are using alternating voltages of high frequency for particle acceleration. The difference is that in MEGs only one cavity element is used for the electron generation in a low-energy regime repeatedly, whereas accelerators aim for highly relativistic energies using multiple cavities, of which all are designed to contribute to the net energy gain of the electron bunches passing through. However, the structure of these basic RF waveguides is quite similar, since electromagnetic waves with field components in the direction of particle propagation are needed. This is provided by electromagnetic waveguides with their specific boundary conditions originating from the geometry of conducting walls. In this section, emphasis is rather given to accelerating field distributions in RF structures, not so much to criteria of continuous acceleration inside of cavity modules by synchronisation of field and particle beam.

If not mentioned otherwise, this section and also 3.3 are based on various textbooks [66, 67, 68], which also give a much more detailed physical understanding of the RF systems beyond the scope of this work.

3.2.1 Wave Equation

In order to generate strong electric fields of high frequencies up to several GHz along the intended propagation path of the particle motion (z-direction in Cartesian coordinates), metallic waveguides are used preferably. The propagation of waves, coupled into the waveguide, obeys the homogenous wave equation, which for the electric field component $\mathbf{E}(\mathbf{r},t)$ is given by

$$\nabla^2 \mathbf{E} - \frac{1}{c^2}\ddot{\mathbf{E}} = 0. \tag{3.9}$$

The ansatz of looking for solutions in the form of an oscillating field with frequency ω, such that $\mathbf{E}(\mathbf{r},t) = \mathbf{E}(\mathbf{r})e^{i\omega t}$, eliminates the time dependency and Eq. (3.9) then yields

$$\nabla^2 \mathbf{E}(\mathbf{r}) + k^2 \mathbf{E}(\mathbf{r}) = 0 \tag{3.10}$$

with the wave number $k = \omega/c = 2\pi/\lambda$, including the wavelength λ.

3.2.2 Waveguide Modes

It is important to generate a wave pattern with an accelerating field component along the particle trajectory in z-direction. This can be achieved from certain geometric configurations of the metallic boundaries in waveguide or cavity structures.

Under considering of only the z-component E_z of the electric field in Eq. (3.10) and the ansatz $E_\mathrm{z}(x,y,z) = f_\mathrm{x}(x) f_\mathrm{y}(y) f_\mathrm{z}(z)$, in which E_z consists of amplitude functions f_i $(\mathrm{i} = \mathrm{x}, \mathrm{y}, \mathrm{z})$, the differential equation describing the electric field in waveguide direction is written as

$$\frac{\partial^2 E_\mathrm{z}}{\partial z^2} + k_\mathrm{z}^2 E_\mathrm{z} = 0 \tag{3.11}$$

with the wave number k_z in z-direction and the following relation:

$$k_\mathrm{z} = \sqrt{k^2 - k_\mathrm{x}^2 - k_\mathrm{y}^2} = \sqrt{k^2 - k_\mathrm{c}^2}. \tag{3.12}$$

Here, k_c denotes the cutoff wave number. Electromagnetic waves can have an undamped propagation in a given waveguide only if $k_\mathrm{c} < k$, then k_z is not imaginary. Otherwise the wave decays exponentially. In any case, the solution of Eq. (3.11) is given by

$$E_\mathrm{z} = E_0 e^{i(\omega t - k_z z)} = E_{0,z} f_\mathrm{x}(x) f_\mathrm{y}(y) e^{i(\omega t - k_z z)}, \tag{3.13}$$

where E_0 is the wave amplitude, or maximum field gradient. Analogue to the electric field, the longitudinal magnetic field B_z can also be calculated using this approach.

For simple geometric structures like rectangular or cylindrical shapes, boundary conditions can be framed to calculate the pattern of electromagnetic field configurations, satisfying these conditions, analytically. Because of the nature of standing waves propagating between the physical boundaries, also higher order modes are forming solutions of Eq. (3.11). In the following, mode spectra for basic waveguide geometries are discussed briefly. With regard to this work, in Chapter 6.1, two different geometric designs for MEG cavities are presented, that are generally based on these basic geometries. Detailed geometric modifications there, however, make the use of numerical calculation inevitable.

Rectangular Modes

The application of boundary conditions to the amplitude functions f_i in Eq. (3.13) leads to a complete solution of the wave equation in waveguides. For a rectangular geometry of side lengths a, b in x- and y direction, as indicated by Figure 3.1, general solutions are in the form of standing waves

$$f_\mathrm{x}(x) = C_1 \sin(k_\mathrm{x} x) + C_2 \cos(k_\mathrm{x} x), \tag{3.14a}$$

$$f_\mathrm{y}(y) = C_3 \sin(k_\mathrm{y} y) + C_4 \cos(k_\mathrm{y} y). \tag{3.14b}$$

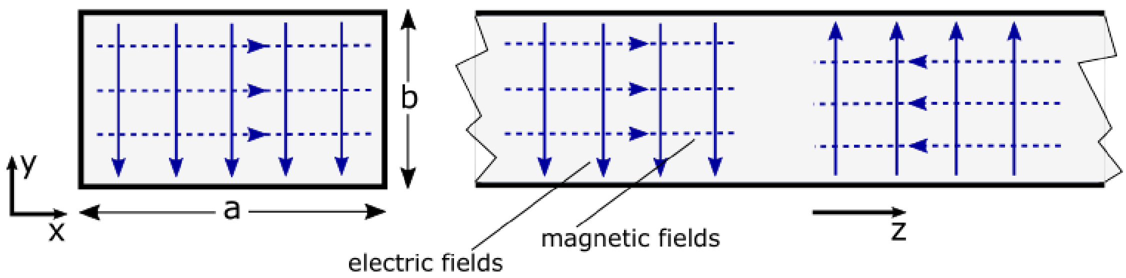

Figure 3.1: Rectangular waveguide section with illustration of the TE_{10} wave pattern in x-y (left) and x-z cross section (right). Figure made in accordance with [68].

The integration constants C_k ($k = 1,2,3,4$) are determined by the requirement that perpendicular electric field components must vanish at the conducting surfaces [$f_x(0) = f_x(a) = 0$ and $f_y(0) = f_y(b) = 0$], thus Eq. (3.13) becomes

$$E_z = E_0 \sin\left(\frac{m\pi x}{a}\right) \sin\left(\frac{n\pi y}{b}\right) e^{i(\omega t - k_z z)}, \tag{3.15}$$

where m and n are integer values defining different modes in transverse field directions according to the modes of a standing wave pattern [68]. Since the electric field is directed transverse to the wave propagation here, modes are called TE_{mn} (**t**ransverse **e**lectric) modes. The basic mode TE_{10} is marked in Figure 3.1 within one slice of the rectangular waveguide. For an expression of the magnetic field strength B_z, the boundary conditions require that the magnetic field component at the surface is equal inside and outside of the conductor [67], namely $\frac{\partial}{\partial x}B_z(x=0) = \frac{\partial}{\partial x}B_z(x=a) = 0$, and $\frac{\partial}{\partial y}B_z(y=0) = \frac{\partial}{\partial y}B_z(y=b) = 0$. Usually, rectangular waveguides are used as RF power transmission lines and are operated in TE modes.

Circular Modes

Especially for accelerating sections the use of cylindrical waveguides is seen foremost, since large longitudinal electric field components can be generated within TM modes in the resonator. This is schematically presented in Figure 3.2, showing the electrical field lines on beam axis

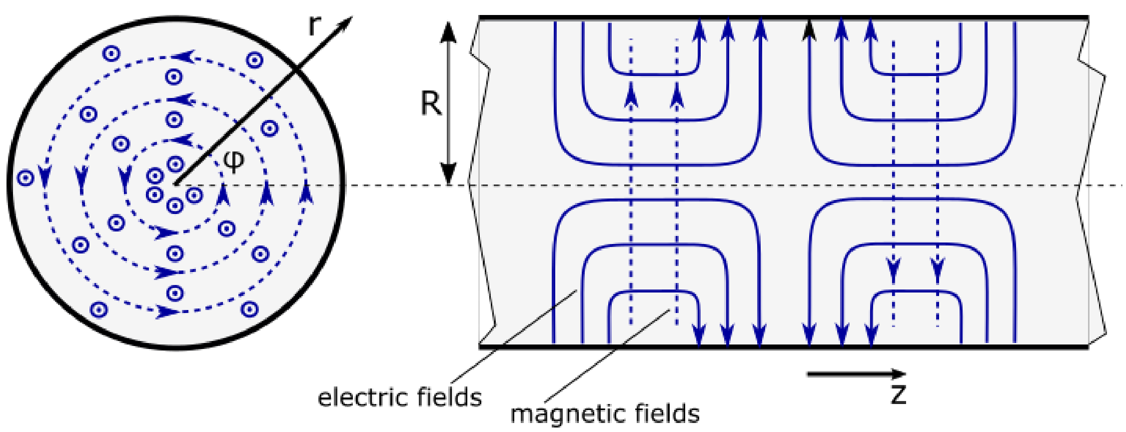

Figure 3.2: Cylindrical waveguide section of radius R with illustration of the TM_{01} wave pattern in r-φ (left) and r-z cross section (right). Figure made in accordance with [68].

and the magnetic field perpendicularly. The wave equation for the electrical field component in cylindrical coordinates is written as

$$\frac{\partial^2 E_\mathrm{z}}{\partial r^2} + \frac{1}{r}\frac{\partial E_\mathrm{z}}{\partial r} + \frac{1}{r^2}\frac{\partial^2 E_\mathrm{z}}{\partial \varphi^2} + \frac{\partial^2 E_\mathrm{z}}{\partial z^2} + k_\mathrm{z}^2 E_\mathrm{z} = 0. \tag{3.16}$$

In this system, based on the derivation for TM modes, the solution of Eq. (3.16) is given by Bessel's function J_m in the form of

$$E_\mathrm{z} = E_{mn} J_m(k_\mathrm{c} r) e^{i(\omega t - m\varphi - k_z z)}, \tag{3.17}$$

which meets the boundary condition of $E_\mathrm{z}(r = R) = 0$ for a cylindrical waveguide structure of radius R. Bessel's function of the order m must be zero at R, so that $J_m(k_\mathrm{c}R) = 0$ is the physical boundary in r-direction and thus the electric field strength reduces with distance to the centre. At this point, the index n in the field amplitude E_{mn} indicates, which root j_{mn} of Bessel's function is considered. If, for example, j_{01} is the first root at $k_\mathrm{c}R = 2.405$ (cf. Figure 3.3) the cutoff wavelength can be formulated as

$$\lambda_c = \frac{2\pi}{k_c} = \frac{2\pi \cdot R}{2.405}. \tag{3.18}$$

Along z-direction the field amplitude is the same for fixed $k_\mathrm{c}r$. For a much deeper mathematical understanding in RF engineering for particle accelerators beyond the scope of this work, [69] has a comprehensive description.

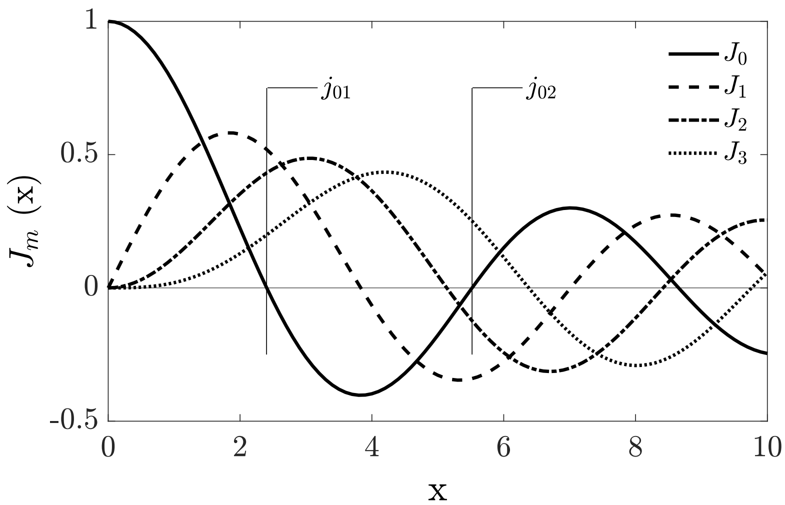

Figure 3.3: Plot of the first kind Bessel functions J_m developing with the distance x in cylindrical coordinates. Used for solving wave propagation in a cylindrical waveguide, $x = k_\mathrm{c}r$ denotes the radial position from the centre. The first two roots of J_0 are indicated by j_{01} and j_{02}, important for determining the cutoff wave number.

3.3 RF Cavities

Formation of a cavity results from the termination of a waveguide section with conducting faces at two points along z-direction, $z = 0$ and $z = L$ for instance. Then, an incoming wave is totally reflected at both additional faces and consequently a standing wave is formed in between. This changes the exponential dependency from Eqs. (3.13) and (3.17) in z-direction to a harmonic one, as in Eqs. (3.19a/b). A longitudinal boundary condition is required for the standing wave to be possible following $L = \pi p / k_z$, where p is an integer eigenvalue of the longitudinal mode order. The electric field in z-direction for the two geometries in TM configuration is then written as:

$$E_{z,\square} = 2E_0 \sin\left(\frac{m\pi x}{a}\right) \sin\left(\frac{n\pi y}{b}\right) \cos\left(\frac{p\pi z}{L}\right) e^{i\omega t} \qquad \text{Rectangular Cavity} \qquad (3.19a)$$

$$E_{z,\bigcirc} = E_{mn} J_m(k_c r) \cos\left(\frac{p\pi z}{L}\right) e^{i(\omega t - m\varphi)} \qquad \text{Cylindrical Cavity} \qquad (3.19b)$$

The mode spectrum shifts to a discrete set of modes referred to as TM_{mnp}, where at least m or n must be greater than one according to the boundary conditions for E_z.

Usually, the highest interest is dedicated to the fundamental TM_{010} mode for its performance in accelerating cavities [70]. Derivation of Eq. (3.19b) for $m = p = 0$ leads to

$$E_z(r) = E_0 J_0 \left(\frac{2.405 \cdot r}{R}\right) e^{i\omega_{010} t}, \tag{3.20}$$

giving the electric field component of a cylindrical cavity of radius R as a function of only the radial distance r from the centre. Here, ω_{010} denotes the systems eigenfrequency in vacuum following

$$\omega_{010} = \frac{2.405 \cdot c}{R}. \tag{3.21}$$

Besides this fundamental TM mode, higher order modes can be calculated similarly. With the help of field simulation software, design studies under consideration of varied geometries and much more complex boundary conditions are discussed in Chapter 6 for the purpose of MEG cavity development in this work.

3.3.1 Resonator Model

Accelerating cavities can be conveniently described by the model of a damped harmonic oscillator under externally driven excitation with electromagnetic waves, coupled into the interior. Analytically, such a system is described in the form of

$$\ddot{x} + 2\gamma\dot{x} + \omega_0^2 x = K e^{i\omega t}, \tag{3.22}$$

where ω_0 is the natural frequency of the system and $Ke^{i\omega t}$ is the externally applied force with amplitude K and oscillating behaviour. Damping occurs due to the wall resistance and also the energy transfer to particles inside the cavity and is expressed by the damping parameter γ.

A general solution to Eq. (3.22) can be achieved with the ansatz $x = Ae^{i\omega t}$ leading to a field amplitude of

$$\mathrm{Re}(A) = \frac{K}{\sqrt{(\omega_0^2 - \omega^2)^2 + 4\gamma^2\omega^2}} \tag{3.23}$$

inside the resonator. From this expression it can be seen that external excitation with ω around the resonance frequency ω_0 causes significantly higher energy transmission into the cavity for cases of weak damping ($\gamma < \omega_0$). Figure 3.4 compares resonance curves of the damped oscillator for varying damping parameters γ, according to Eq. (3.23).

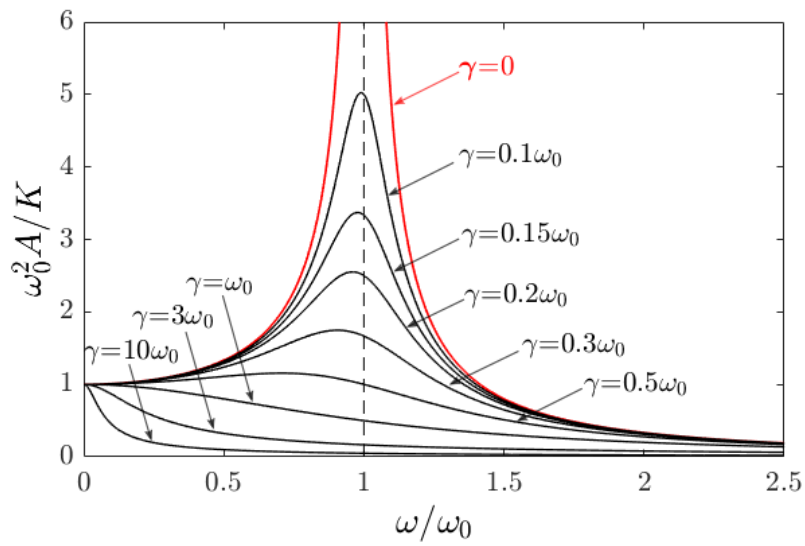

Figure 3.4: Resonance curves of a damped oscillator. The normalised oscillation amplitude A is plotted versus the excitation frequency ω for different damping constants γ.

Equivalent Circuit

Another way of describing a resonant cavity is by using an equivalent circuit, as presented in Figure 3.5. The cavity itself is thereby represented by passive circuit elements forming an RLC-circuit [71]. Here, R_s is the shunt impedance, L is the inductance and C the capacitance formed by the metallic faces creating a parallel plate configuration. The resonant radian frequency in a parallel RLC-circuit like this is given by

$$\omega_0 = \frac{1}{\sqrt{LC}}. \tag{3.24}$$

At that frequency the cavity impedance $Z_{cav}(\omega_0) = R_s$ is equal to the shunt impedance and of real value. Generally, and for no specific value of ω, the impedance is given by a complex notation following

$$\mathbf{Z}_{cav} = \frac{\hat{U}}{\hat{I}} = \frac{1}{\frac{1}{R_s} + i(\frac{1}{L\omega} - C\omega)}, \tag{3.25}$$

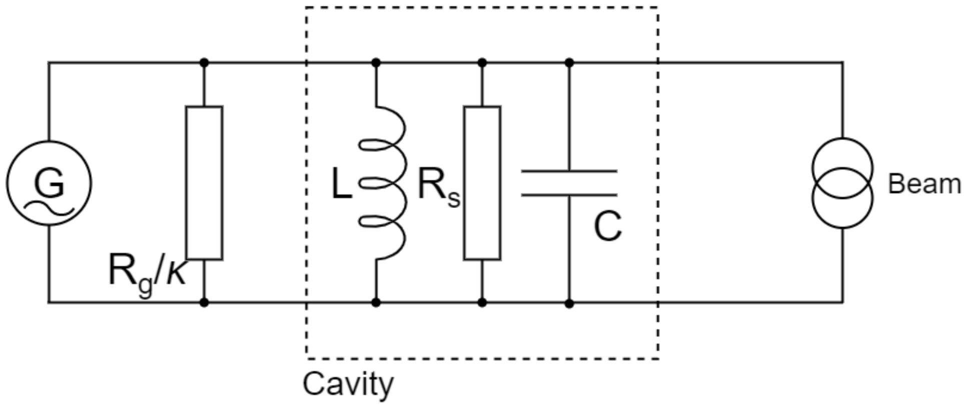

Figure 3.5: Equivalent circuit of a resonant cavity, including the generator G and possible beam loading. Figure made in accordance with [73].

equal to the effective voltage $\hat{U}$ divided by the effective current $\hat{I}$ flowing through the RLC-elements parallelly [72]. If a generator G including an inner resistance of R_g is included, it is coupled to the cavity according to the coupling factor κ. When $\kappa = 1$, the resistance of the power source is perfectly matched to the cavity [73]. Otherwise the coupling is sub- or supercritical and could be seen as another origin of damping, which will be discussed in Section 3.3.4 in more detail. Contrary to the resonant case, for excitation voltages with frequencies off resonance ($\omega \neq \omega_0$), the generator voltage is not in phase to the current any more [67]. In that case Eq. (3.25) can also be written as

$$\mathbf{Z}_\mathrm{cav} = \frac{R_\mathrm{s}}{1 + iQ_0\left(\frac{\omega}{\omega_0} - \frac{\omega_0}{\omega}\right)} \approx \frac{R_\mathrm{s}}{1 - i\tan\Phi}, \tag{3.26}$$

including the tuning angel Φ between current and voltage [73]. The hereby introduced quality factor Q_0 is an important parameter in regards to power dissipation, which is illustrated in the following section.

The possible presence of to be accelerated particles is included on the right side of Figure 3.5 as a current source counteracting the generator current, since power would be transferred into kinetic beam energy [73]. Additional influences by cavity-beam interaction on the circuit is content of Section 3.4. Both, coupling as well as beam loading, are important loss parameters for the operation of MEG cavities because of the oscillating electron cloud and an inconstant total beam charge, thus varying impedances.

3.3.2 Quality Factor

With regard to resonating cavities, one of the most important figures of merit for their efficiency is the quality factor Q. In terms of the equivalent circuit in Figure 3.5 for a cavity without externally sustained oscillation, the unloaded Q can be qualified by

$$Q_0 = \omega_0 R_\mathrm{s} C = \frac{R_\mathrm{s}}{\omega_0 L} = R_\mathrm{s}\sqrt{\frac{C}{L}}. \tag{3.27}$$

Generally, the unloaded quality factor is a quantity describing the energy loss of an oscillating system and therefore is a measure of damping. A large Q-value is equivalent to a small damping constant and might lead to the propagation of oscillations with high amplitude inside the system, as already indicated by Figure 3.4. In case of an RF cavity, the quality factor particularly characterises the ratio of stored to consumed energy per period, given by

$$Q = \frac{2\pi \cdot \text{stored energy}}{\text{energy loss/period}} = \frac{2\pi}{T} \cdot \frac{W}{P} = \frac{\omega_0 W}{P}, \tag{3.28}$$

where W is the stored energy, T is the oscillation period and ω_0 is the angular resonance frequency. The average rate of energy loss P is equal to the change in stored energy following

$$P = -\frac{dW}{dt} = -\frac{2}{\tau} \cdot W \tag{3.29}$$

with the time constant $\tau = RC = 2Q/\omega_0$ of exponentially increasing or decreasing fields inside the cavity [74]. A more detailed explanation of power losses is part of the following sections for the introduction of additional important figures of merit in fundamental cavity design.

Apart from that, there is stored energy within the excited mode of the electromagnetic field, which is transmitted into the cavity. It can be calculated from the volume integral of the squared average electric and magnetic field over the entire cavity volume V in vacuum as follows [73, 74]:

$$W = \iiint_V \left(\frac{\varepsilon_0}{2} |\mathbf{E}|^2 + \frac{\mu_0}{2} |\mathbf{H}|^2 \right) dV = \frac{\varepsilon_0}{2} \iiint_V \mathbf{E}^2(x,y,z)\, dV \tag{3.30}$$

According to [67, 75], for the fundamental TM_{010} mode of a circular cavity with length L and radius R Eq. (3.30), together with Eq. (3.20), yields

$$W = \frac{\varepsilon_0}{2} \iiint_V |E_z(r)|^2 dV = \frac{\varepsilon_0}{2} \iiint_V E_0^2 J_0^2(2.405)\, dV = \frac{\varepsilon_0}{2} E_0^2 L R^2 J_1^2(2.405). \tag{3.31}$$

3.3.3 Power Losses in Cavity Structures

There are several mechanisms leading to energy loss in an excited cavity. In vacuum and without the presence of free charged particles, ohmic losses are dominating due to the natural ohmic resistance of the conducting walls. More precisely, an electrical surface current $\mathbf{j}_\mathrm{A}$ is induced by the RF fields and thus some of the field energy is converted into heat. It can be derived from Ampere's law in Eq. (3.1b) and must be equal to tangential magnetic field strength $\mathbf{H}_\mathrm{t}$ near the surface. Then, the total power loss from the inner walls P can be calculated from integrating the power density along the total conducting inside surfaces [73, 74] following

$$P = \frac{1}{2} \int_A |\mathbf{H}_\mathrm{t}|^2 \frac{1}{\sigma\delta} \partial A, \tag{3.32}$$

where σ is the conductivity and δ is the penetration depth of the field and surface current, which is a property of the non-perfectly conducting material, called *skin depth*. Both, σ and $\delta = \sqrt{2/\mu\sigma\omega}$, are defined by the material as well as the condition it is in. Describing the wall losses in terms of an impedance, P can be expressed by

$$P_{\mathrm{cav}} = \frac{U_0^2}{2R_{\mathrm{s}}}, \tag{3.33}$$

including the voltage U_0, which is the integrated accelerating RF field a particle would experience, while it is located within the accelerating gap d inside the cavity at optimum phase [70]. Since in reality the particles are seeing a time-varying force while traversing the gap, a maximal possible energy gain $\Delta E = qU_0$ must be corrected by the *transit-time factor* T_{TTF} and $U_{\mathrm{acc}} = E_0 d T_{\mathrm{TTF}}$ is referred to as an effective cavity voltage [67]. The shunt impedance R_{s} generally is in the order of MΩ and depends on the cavity geometry, material properties and the operating frequency. A factor of 0.5 is added from looking at the average voltage $\sqrt{\langle U^2 \rangle} = U_0/\sqrt{2}$ to maintain the analogy to Ohm's law [74].

In MEG operation, however, only electrons with kinetic energies up to a few hundred eV are usually contributing to the multipacting process, hence particle velocities are not relativistic ($v \ll c$) and are much more affected by the RF field. Also the effectiveness of the RF driven accelerating gap is of minor importance, since efficient acceleration is not needed to maintain the multipacting resonance condition. As a consequence, R_{s} might as well have a smaller value, while the MEG can be powered sufficiently.

In any case, with larger Q, less external power is needed to sustain the stored energy inside the cavity with regard to Eq. (3.28). For design considerations however, a precise value of resistive wall losses is hard to calculate. By combining Eqs. (3.28) and (3.33) the ratio of R_{s} and Q can be formed, written as

$$\frac{R_{\mathrm{s}}}{Q} = \frac{U_{\mathrm{acc}}^2}{2\omega_0 W}; \tag{3.34}$$

a fundamental design quantity, independent of surface properties and only defined by the cavity geometry.

3.3.4 Coupling of an external RF Source

This section describes the situation specifically involving the power, generated by an external power source, that is transmitted into the cavity to sustain the field energy of the electromagnetic modes within. Thereby, power in terms of electromagnetic waves is guided from the generator to the electric loads through a transmission line, as already indicated by Figure 3.5.

At the cavity port, different ways of coupling energy into the resonator are possible via coaxial couplers, shown in Figure 3.6. There is coupling to the electric field by an antenna (a), coupling to the magnetic field by a wire, shorted to the wall and forming a loop (b), and coupling to the magnetic field lines of the excited mode using a waveguide (c) [76]. For minimum reflection at the coupling port, and thus small power losses, the line impedance Z_0 must be matched to the shunt impedance $Z_{\mathrm{cav}}(\omega_0) = R_{\mathrm{s}}$ of the cavity. With regard to the equivalent circuit, this can be realised by an impedance transformation through the coaxial coupler leading to $Z_{\text{cav}} = R_{\text{s}}/n^2$ [77], so that

$$\frac{Z_{\text{cav}}}{Z_0} = \frac{R_{\text{s}}}{n^2 Z_0} = \kappa \tag{3.35}$$

is equal to the ratio of power lost outside the cavity P_{ext} and power dissipated inside the cavity P_{cav}, known as the coupling factor κ. In that context, n can be seen as the number of windings in a transformer, coupled to the inductance of the corresponding resonator. Generally, there is a distinction of three different coupling scenarios:

- subcritical coupling ($\kappa < 1$)
- critical coupling ($\kappa = 1$)
- supercritical coupling ($\kappa > 1$)

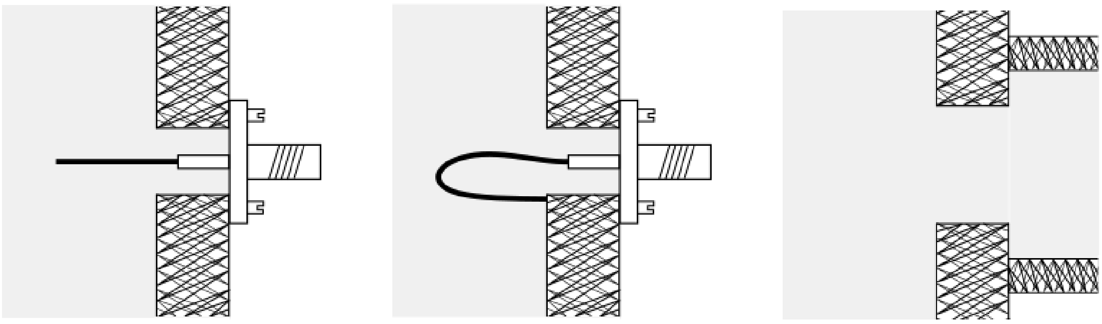

(a) Pin coupling (b) Loop coupling (c) Slit coupling

Figure 3.6: Different coupling mechanisms for power transmission into an RF cavity.

Loaded Q

Before the effects of power reflection due to non-critical coupling at the transmission line-to-cavity interface can be discussed in more detail, it needs to be stressed that from a cavity point of view, stored energy W also dissipates into the matched load of the generator [76]. Therefore, the resonator is loaded in addition to the inevitable wall losses P_{cav} resulting in a loaded quality factor Q_{L}, which yields

$$Q_{\text{L}} = \frac{\omega_0 W}{P_{\text{cav}} + P_{\text{ext}}} = \frac{Q_0}{1+\kappa}. \tag{3.36}$$

From this relation it can be seen that the coupling factor κ also describes the ratio of unloaded-to-externally loaded Q, following

$$\kappa = \frac{P_{\text{ext}}}{P_{\text{cav}}} = \frac{\omega_0 W}{Q_{\text{ext}}} \cdot \frac{Q_0}{\omega_0 W} = \frac{Q_0}{Q_{\text{ext}}}. \tag{3.37}$$

In fact, all possible power loss mechanisms, for example radiation through openings, discharge, or losses in dielectric materials inside the cavity, could technically be taken into account as well with this notation [73]. By adding up power losses P_i from different loss mechanisms for the calculation of a total loaded Q, as indicated with Eq. (3.36), the sum of all related Q_i then yields

$$\frac{1}{Q_\mathrm{L}} = \sum_{i=1}^{n} \frac{1}{Q_i} = \frac{1}{Q_0} + \frac{1}{Q_\mathrm{ext}} + \frac{1}{\dots}. \tag{3.38}$$

Especially the discharge at metallic surfaces, which is important for the achievement of a reasonably large current density in a multipacting gun, might have a high influence on the instantaneous Q_L of the gun cavity in an MEG.

Power Reflection and Transmission

Most of the aforementioned sources of power loss can be avoided by smart cavity design and accurate manufacturing. Reflection losses, however, are always crucial and important to understand, since they are influenced by environmental factors like heating or an unsteady power supply at the coupler, for instance. Furthermore, a variable coupling mechanism can give the opportunity for tuning of the loaded Q and thus controlling the temporal evolvement of cavity filling, as shown later with help of Figure 3.8.

In case of reflection at the coupler, a forward travelling wave with the effective voltage amplitude $\hat{U}_\mathrm{f}$ and a reflected wave $\hat{U}_\mathrm{r}$ in opposite direction are formed on the transmission line. Thereby, the complex reflection coefficient ρ gives the ratio of reflected to forward voltage [76], following

$$\rho = \frac{\hat{U}_\mathrm{r}}{\hat{U}_\mathrm{f}} = \frac{\kappa - 1 + iQ_0\delta}{\kappa + 1 + iQ_0\delta}, \tag{3.39}$$

where $\delta = \left(\frac{\omega}{\omega_0} - \frac{\omega_0}{\omega}\right) = \frac{\omega^2 - \omega_0^2}{\omega\omega_0}$ is equal to $2\Delta\omega/\omega$, when $\Delta\omega \ll \omega_0$. Here, $\Delta\omega$ denotes the frequency difference to the resonance peak $\omega - \omega_0$. For $\omega = \omega_0$, when the incoming wave would excite the cavity resonantly, Eq. (3.39) yields

$$\rho(\omega_0) = \frac{\kappa - 1}{\kappa + 1}. \tag{3.40}$$

Since ρ generally is a complex function of ω, the effective ratio of reflection and transmission can be obtained by its absolute value, written as

$$|\rho(\omega)| = \sqrt{\frac{(\kappa - 1)^2 + Q_0^2\left(\frac{\omega}{\omega_0} - \frac{\omega_0}{\omega}\right)^2}{(\kappa + 1)^2 + Q_0^2\left(\frac{\omega}{\omega_0} - \frac{\omega_0}{\omega}\right)^2}}. \tag{3.41}$$

For better visualisation of the reflection coefficient ρ of an incoming wave at the coupling port, Figure 3.7 is given to present ρ in the complex plane (a) and also the absolute value around ω_0 (b) for different coupling coefficients exemplary, in reference to Eqs. (3.39) and (3.41).

As mentioned earlier, control over the filling time, which is the same as for the decay time constant in Eq. (3.29), is an important experimental fine-tuning opportunity of Q in dependence of the coupling strength. Also in case of detuning by eventual beam loading, variable coupling

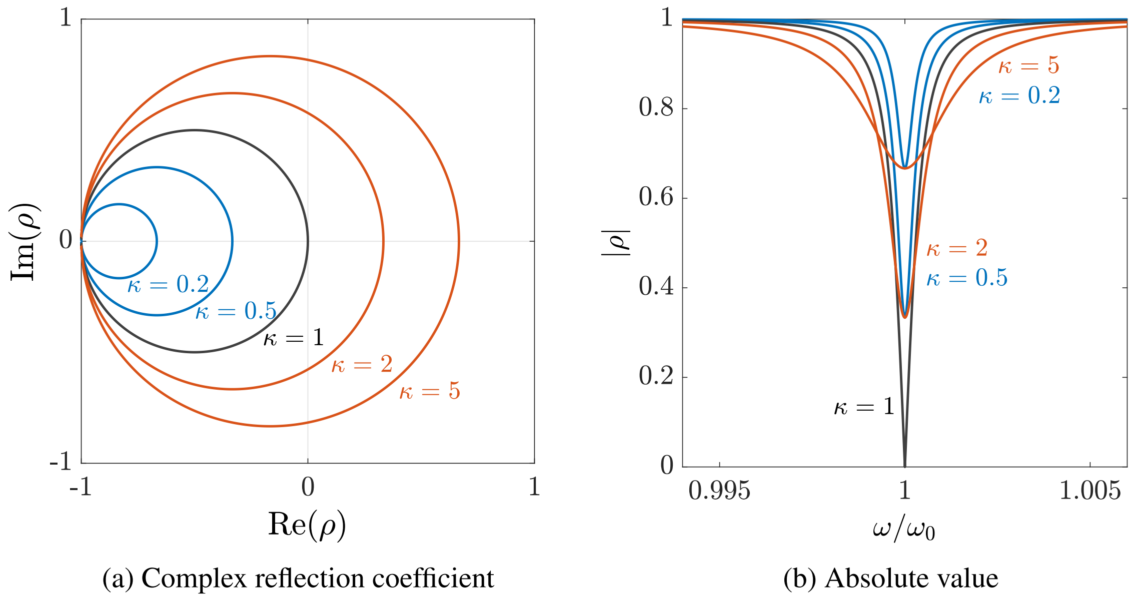

Figure 3.7: Reflection coefficient ρ, visualised in the complex plane (a), and with the absolute value for excitation frequencies around ω_0 (b). The colours represent different coupling situations: critical (black), supercritical (red), and subcritical coupling (blue).

is beneficial for the match between generator and cavity [78]. Under consideration of a steady voltage at the coupler, the backward and forward parts (U_r, U_f) relate to the total voltage U as

$$U = U_\mathrm{r} + U_\mathrm{f} = U_\mathrm{f}(\rho + 1) = U_\mathrm{f}\frac{2\kappa}{\kappa+1}, \tag{3.42}$$

by use of Eq. (3.40), assuming resonant excitation at ω_0 and a reflection of the incoming wave given $U_\mathrm{r} = \rho U_\mathrm{f}$. After switching on the voltage, an exponential increase in transmission into the resonator is assumed, so that the temporal evolution of the voltage in Eq. (3.42) can be described by

$$U(t) = U_\mathrm{f}\frac{2\kappa}{\kappa+1}\left(1 - e^{-t/\tau}\right). \tag{3.43}$$

Since $\tau \gg 2\pi/\omega_0$, the sinusoidal RF component can be neglected and only the envelope function of the forward voltage $\hat{U}_\mathrm{f} = \hat{U}_\mathrm{f} \cdot \sin\omega t = U_\mathrm{f}/\sqrt{2}$ is considered here. After taking also the time-dependent amplitude of the reflected voltage $U_\mathrm{r}(t) = U(t) - U_\mathrm{f}$ into account, the reflected power at the coupling port yields

$$P_\mathrm{r}(t) = \frac{U_\mathrm{r}^2(t)}{2R} = P_\mathrm{f}\left(\frac{2\kappa}{\kappa+1}\left(1 - e^{-t/\tau}\right) - 1\right)^2, \tag{3.44}$$

where P_f is the power in forward direction to the coupler and R is the line resistance. Consequently, for the ratio of power P_cav, that is transmitted into the cavity as a function of time, Eq. (3.44) derives into

$$\frac{P_\mathrm{cav}(t)}{P_\mathrm{f}} = 1 - \frac{P_\mathrm{r}(t)}{P_\mathrm{f}} = 1 - \left(\frac{2\kappa}{\kappa+1}\left(1 - e^{-t/\tau}\right) - 1\right)^2. \tag{3.45}$$

Figure 3.8 shows the transmitted-to-forward power ratio for different coupling constants k. With the beginning of power supply the cavity is filled according to Eq. (3.45). In case of critical coupling all of it is transmitted into the cavity, when a steady state is reached, in dependency of the filling time constant τ. For supercritical, as well as subcritical coupling ($\kappa \neq 1$), the steady state power transmission is smaller and some power is also reflected, whereas for $\kappa > 1$ a faster filling (or smaller τ) can be observed.

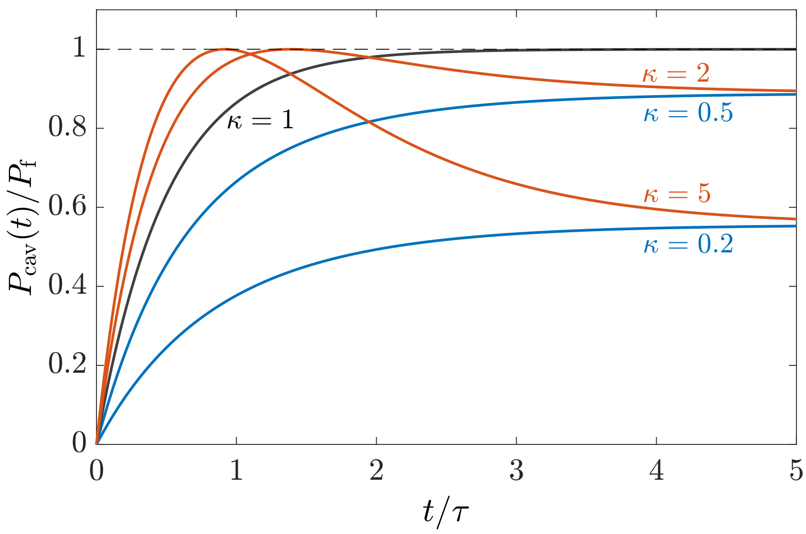

Figure 3.8: Power transmission ratio $P_{\text{cav}}/P_{\text{f}}$ into a coupled resonator for different coupling strengths κ as a function of time after beginning of the power supply. The colours represent different coupling situations: critical (black), supercritical (red), and subcritical coupling (blue).

3.4 Beam Loading

The last major power loss mechanism, which is discussed at this point, is related to the situation of actual particle acceleration inside the cavity, namely beam loading. In accelerating RF structures it is a consequence of the interaction of the waveguide or cavity itself with beam induced fields of significant magnitude, where the accelerating fields become modified by considerably large beam currents [67]. Thereby, and considering the circuit model in Figure 3.5, a charged particle beam acts as a current source like the generator G, but in opposite direction and therefore the cavity is loaded additionally.

After the fundamental theorem of beam loading, a charge carrier traversing the RF cavity sees exactly one-half of its own induced field whether or not a generator voltage component is present [79]. This can be seen equivalently to the deposition of this charge q on the capacitive part (capacitance C) of the cavity inducing a voltage $U_{\text{beam}} = q/C$. Together with Eq. (3.27) and the stored capacitive energy $\Delta E = CU^2/2$, the power loss $P_{\text{beam}} = dE/dt$ to an initially empty cavity can approximately be obtained from the energy left behind in the cavity

$$\Delta E_{\text{beam}} = \frac{1}{2} C U_{\text{beam}}^2 = \frac{1}{2} \frac{\omega_0 R}{Q_0} q^2 \equiv k_{\text{loss}} q^2, \tag{3.46}$$

where k_{loss} denotes a geometry related loss parameter that is different for each resonant mode. This expression is a single bunch approximation for very short bunches. In case of a bunch train of consecutive charge packages, where the time t_{b} between each passage is large compared to the cavity decay time τ, the total induced beam voltage is a result of the cumulative accumulation of induced fields by previous charges [67]. In this case, $U_{\text{beam},i}$ decays by $e^{t_{\text{b}}/\tau}$ after each traversing bunch and the successive one sees the voltage phase and amplitude modulated [80]. This situation, leading to a stationary state, is called transient beam loading. In linear accelerators it contributes to many important effects regarding efficient beam acceleration [81].

When power is consumed by beam currents, the coupled generator impedance is further mismatched to the cavity leading to a change in power transmission. Without going into detail, preservation of the required cavity voltage U_0 by minimum external power supply can be obtained through adjustment of the tuning angle between the generator voltage and the beam loaded cavity [67]. A detailed derivation is given in [80] for instance. However, in consideration of a beam loaded cavity, total power losses P are resulting from the conservation of energy [67], following

$$P = P_{\text{cav}} + P_{\text{r}} + P_{\text{beam}} + \sum_{i=1}^{n} P_i, \tag{3.47}$$

as the sum of wall losses P_{cav}, external reflection losses P_{r} ($P_{\text{r}} = 0$ for $\kappa = 1$), losses due to beam loading P_{beam} and other possible losses P_i of potentially minor impact.

At this point it has to be mentioned, that the expression in Eq. (3.46) and also the transient response are general simplifications to short particle bunches with efficient energy gain, which is not that easily applicable to the gun cavity of MEGs, where the charge per period is not necessarily constant. Additionally, the MEG, as will be seen in the following chapters, is not meant to maximise beam energy. Besides positive acceleration, particles are also decelerated for maintaining the multipacting condition. Therefore, numerical assistance is required for an accurate approximation of P_{beam} in the context of "unusual" particle distributions without aiming to maximise energy gain. The importance of beam loading for stable MEG operation is rather high in any case, since it acts as a self-stabilising mechanism in terms of suitable electron impact energies, together with the SE yield of the material (cf. Section 4.1). Implementation of beam loading, specifically considering two-sided multipacting in RF cavities with respect to stabilised beam currents, is discussed in Section 4.2.1.

4 Theory of Multipacting Electron Guns

This chapter is intended to bring together the physics of multipacting and the motion of electrons inside an RF gun cavity, particularly building up on the MEG principle from Section 2.3.1. Therefore, it will be given a single particle calculation in order to obtain a first approximation of the resonant multipacting condition in the desired electromechanical parameter space, also implying the effect of self-bunching (cf. Section 4.1.2). Additional changes due to many-particle interaction in terms of repulsive space charge forces are introduced, since high charge densities at low particle velocities are expected in reality. To this point, however, figures of merit for actual beam quality characterisation outside the gun are not included.

4.1 Resonant Multipacting

In reference to Section 2.3, the resonance condition in a two-sided multipacting electron gun describes a stationary situation, in which one or more electrons travel the distance d towards the opposing surface within one or more (up to N) half-cycle of the RF field after their creation. It also implies that for each impact the kinetic energy of the particles is sufficient to generate one or more electrons at the respective surface on average. After each half-cycle the recently created particles find the same starting condition as the particles of previous generations and thus the half-cycle may repeat in a resonant manner.

4.1.1 Single-Particle Resonance Condition

Before going into a qualitative analysis of the particle motion, some major quantitative geometric and operational parameters according to the model of multpacting electron guns need to be defined. Figure and Table 4.1 show a schematic illustration of the parameter space involving a point-like electron of charge e and mass m_e, which is accelerated in an RF field periodically, perpendicular to two plane-parallel surfaces. Here, the opposing surfaces are separated by the axial distance d in field direction z and have secondary electron yield coefficients δ_1 and δ_2, respectively.

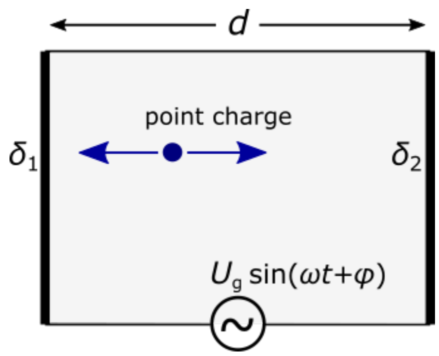

Figure 4.1: MEG operation scheme in the single-particle picture.

d	gap distance
$f=\omega/2\pi$	operating frequency
U_g	maximum gap voltage
$E_0=U_\mathrm{g}/d$	peak field gradient

Table 4.1: Operational parameters.

From the equation of motion, defined by the Lorentz force in Eq. (3.3), a one-dimensional charged particle trajectory in z-direction, according to the idealised model in Figure 4.1, is described by

$$\ddot{z} = \frac{e}{m_{\mathrm{e}}} E_0 \sin(\omega t + \varphi), \tag{4.1}$$

where $\omega = 2\pi f$ is the angular frequency of the external source and φ is the phase shift relative to the field. All calculations are based on the restriction that an operating frequency of $f = 2.998\,\mathrm{GHz}$ is fixed by design considerations.

For an electron released at phase φ with velocity v_0, carrying out the integral over Eq. (4.1) [82], once for the derivation of the velocity $v(t)$ and twice for the position $z(t)$, yields

$$v(t) = \frac{e}{m_{\mathrm{e}}} \frac{E_0}{\omega} \left(\cos\varphi - \cos\left(\omega t + \varphi\right)\right) + v_0, \tag{4.2a}$$

$$z(t) = \frac{e}{m_{\mathrm{e}}} \frac{E_0}{\omega^2} \left(\sin\varphi - \sin\left(\omega t + \varphi\right) + \omega t \cos\varphi\right) + v_0 t. \tag{4.2b}$$

Here, the zero phase convention for the origin of time is chosen, meaning that $t = 0$ is at the zero crossing of the RF field rather then the instant of emission. To achieve resonant behaviour, a single electron has to travel the distance $z = d$ within N half periods (N odd) of the driving RF force ($\omega t = N\pi$) [83]. In the following and for the sake of simplicity only the first half-cycle $N = 1$ is being focused on, leading to a resonant condition for the gap voltage of

$$U_{\mathrm{g}} = \frac{m_{\mathrm{e}} \omega d}{e} \frac{\omega d - \pi v_0}{\pi \cos\varphi + 2 \sin\varphi}. \tag{4.3}$$

Furthermore, the realisation of a steady multipacting condition reduces with increasing N [58, 84], making higher degrees $N > 1$ less viable for any controlled application. Emission energies for true secondary electrons are in the order of a few eV, according to [50] and others.

Besides the fixed parameters ω and v_0, here, the resonant gap voltage in Eq. (4.3) only depends on the emission phase φ and the gap distance d. In Figure 4.2a, U_{g} is plotted as a function of φ for a fixed cathode distance $d = 1.16\,\mathrm{mm}$ and an initial velocity $v_0 \simeq 1.2 \cdot 10^6\,\frac{\mathrm{m}}{\mathrm{s}}$, equivalent to $\simeq 4\,\mathrm{eV}$ of energy, exemplarily. It decreases from the point of electron emission at phase $\varphi = 0$:

$$U_{\mathrm{g},0} \simeq \frac{m_{\mathrm{e}} \omega d (\omega d - \pi v_0)}{e\pi}, \tag{4.4}$$

until reaching a minimum at $\varphi_{\mathrm{max}} = \arctan\frac{2}{\pi}$:

$$U_{\mathrm{g,min}} = \frac{m_{\mathrm{e}} \omega d (\omega d - \pi v_0)}{e\sqrt{\pi^2 + 4}}. \tag{4.5}$$

This voltage range $\Delta U_{\mathrm{g}} = [U_{\mathrm{g,min}}, U_{\mathrm{g},0}]$ is related to the appropriate initial phase range for stable MEG operation [85], since electrons created within $[0, \varphi_{\mathrm{max}}]$ are accelerated upon reaching the opposing surface resonantly, while also meeting the self-bunching criterion [64]. To be clear at this point, the maximum gap voltage $U_{\mathrm{g},0}$ is obtained at $\varphi = 0$ only for zero initial electron

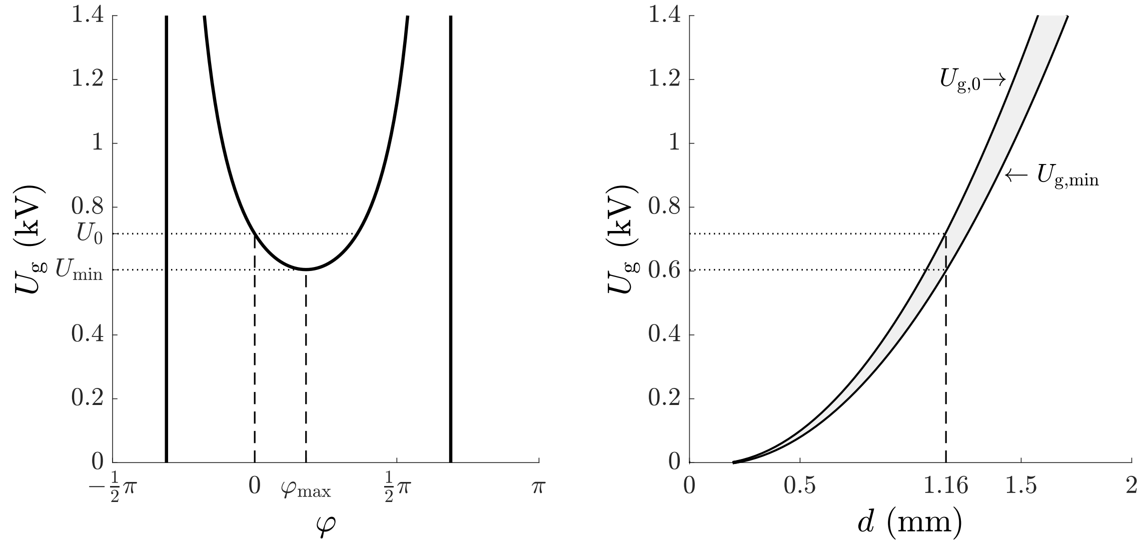

(a) Gap voltage versus emission phase for $d = 1.16\,\mathrm{mm}$

(b) Gap voltage versus gap distance for $\varphi = 0$, and $\varphi_{\max} = \arctan\frac{2}{\pi}$

Figure 4.2: Resonant gap voltage U_{g} as a function of emission phase φ (a), and gap distance d (b), for an operating frequency of $\omega = 2\pi \cdot 2.998\,\mathrm{GHz}$ and initial particle energy $E_{\mathrm{esc}} = 4\,\mathrm{eV}$.

velocities ($v_0 = 0$). A negative phase is possible for $v_0 > 0$, if the emitted electron at $\varphi < 0$ is reversing direction before striking the surface of origin [64]. To the authors knowledge no explicit formula exists, precisely covering $\varphi_{\min}(v_0 > 0)$, although an adjustment can be obtained numerically [86]. However, a presentation of the resonant gap voltage as a function of d is given in Figure 4.2b for the same parameters as used in (a).

In case the operating frequency is not predetermined, the cavity geometry, namely d, can be related to the RF voltage and frequency by susceptibility curves $U_{\mathrm{g}}(fd)$, as [58, 64] discuss in detail. Thereby, they also show the influence of small variations in v_0 on the achievable gap voltage. Since an exact v_0 is not easily predictable, the amount of its influence on the resonant condition is not particularly derived for this work, but it is considered in numerical calculations.

4.1.2 Self-Bunching Mechanism

Assuming that for the moment still no mutual interactions like scattering or Coulomb forces between particles are present, an extension of the single-particle model towards an electron distribution of charges with different longitudinal positions $z_i(t)$ can be described. Thereby, electrons at different positions within a bunch inside the cavity are related by the phase φ_i relative to the RF field, when they were created.

The earlier mentioned self-bunching mechanism is essential for resonant multipacting under any circumstances due to its counteracting on repulsive space charge forces between electrons in resonance. This can be visualised by looking at their travelling distance, presented in Figure 4.3. For an electrons' travelling length L during one RF half-cycle (*transit time* $t = T/2 = \pi/\omega$)

Eq. (4.2b), together with $E_0 = U_g/d$, translates into

$$L = z\left(\frac{\pi}{\omega}\right) = \frac{eU_g}{m_e\omega^2 d}\left(\pi\cos\varphi + 2\sin\varphi\right) + v_0\frac{\pi}{\omega} \tag{4.6}$$
$$= \frac{eU_g}{m_e\omega^2 d}\sqrt{4+\pi^2}\,\sin\left(\varphi + \arctan\frac{\pi}{2}\right) + v_0\frac{\pi}{\omega}.$$

By solving Eq. (4.6) for the emission phase φ, a synchronous phase φ_{sync} of the electron arriving at L after exactly $t = T/2$ can be derived, so that

$$\varphi_{sync} = \arcsin\left(\frac{\left(L - v_0\frac{\pi}{\omega}\right)m_e\omega^2 d}{eU_g\sqrt{4+\pi^2}}\right) - \arctan\frac{\pi}{2}. \tag{4.7}$$

The other crossing point of $d = L$ in Figure 4.3 ($\varphi = \theta$) corresponds to the second crossing point of any given resonant gap voltage $U_g(\varphi)$ on the other side of the minimum in Figure 4.2a. Its maximum is governed by the highest possible voltage $U_{g,0}$ at resonance. Although the phase range up to the second point of d-crossing satisfies the resonance condition from Eq. (4.3), electrons emitted at phases $\varphi > \varphi_{max}$ would disperse in longitudinal direction.

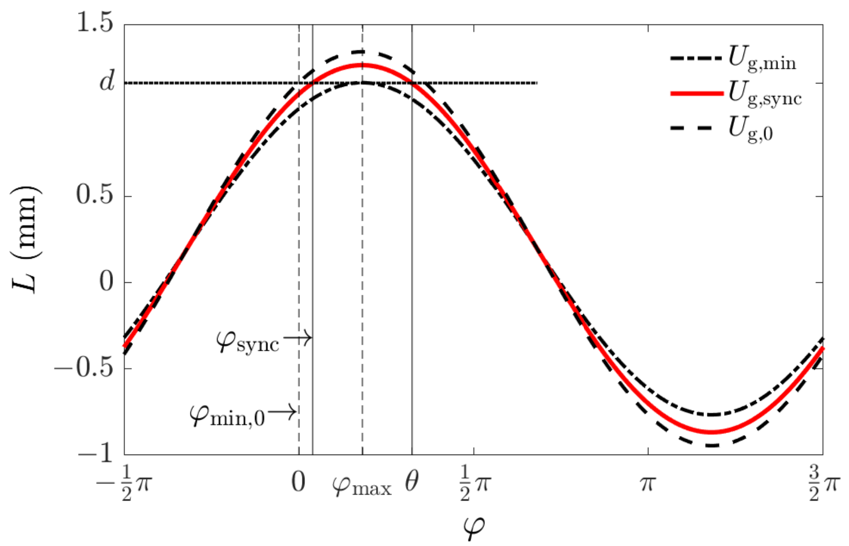

Figure 4.3: Travelling length L of an electron after one RF half-cycle as a function of its emission phase φ relative to $t_0 = 0$, according to Eq. (4.6), for different accelerating gap voltages U_g and fixed d. Here, the dashed lines represent voltages enclosing the resonant condition from Eqs. (4.4) and (4.5) in determination of the stable phase range $\Delta\varphi = [\varphi_{min,0}, \varphi_{max}]$. For a voltage $U_{g,min} < U_g < U_{g,0}$, φ_{sync} and θ indicate phases of an electron in synchronism to the driving RF field.

When considering the case of an externally applied voltage in between $U_{g,min}$ and $U_{g,0}$, the phase region of longitudinal bunch focusing is given by $\Delta\varphi = [\varphi_{min,0} \leq 0, \arctan\frac{2}{\pi}]$. Projection of the respective starting times $t_{0,i}$ of each electron to their corresponding emission phase φ_i in reference to a synchronous particle $t_{0,sync}$ concludes, that $\varphi_i < \varphi_{sync}$ can be associated with earlier emitted electrons and $\varphi_i > \varphi_{sync}$ with emission at later times. In regards to Figure 4.3, later emitted electrons in relation to φ_{sync} have a longer travelling length and thus are accelerated stronger, whereas earlier emitted electrons undergo weaker acceleration. Consequently, electrons generated prior and posterior (up to $\varphi_{\max}$) to the synchronous particle approach each other within the transit time $t = T/2$, given their respective trajectory. In the phase range between $\varphi_{\max}$ and $\varphi_{\max} + \pi$, the travelling length decreases with respect to earlier emitted electrons, hence their spacial distance increases.

The self-bunching mechanism in MEGs can be looked at similarly to bunch focusing as part of the longitudinal particle dynamics in large accelerator machines [87]. However, during MEG operation electrons inside the stable phase region, specifically at $\varphi_i > \varphi_{\text{sync}}$, are hitting the opposite surface when reaching $z = d$. For this analytical approximation no delay time of secondary emission is taken into account. It is shown that a stable phase-locked multipacting phase is conserved for small variation in the statistical noise of emission energy and delay time, even though it is proportional to rms fluctuations in the SE process [88].

4.1.3 Total Secondary Electron Gain

Sustainability of the multipacting process on a larger time scale is not only a consequence of satisfying the resonant condition and bunch focusing. An equally important factor is the total secondary electron gain G being above, or close to one as well. In an MEG one cathode surface needs to be partially transparent (cf. Figure 2.11) in order to release the electron beam to the outside. A condition for the total SE gain after N RF periods is therefore written as

$$G = [\delta_2 \delta_1 (1 - T)]^N > 1, \tag{4.8}$$

where T is the ratio of transmitted to incident electrons at the transmissive surface [83]. It is reasonable to develop boundary conditions for the controllable parameter space in Table 4.1, which also lead to $G > 1$.

Furthermore, in reference to Section 2.2.5, the SE yield coefficients δ_1 and δ_2 of the respective emission surfaces are heavily dependent on the impact energy Σ. For electrons meeting the resonance condition of two-sided multipacting, an equivalent impact velocity can be obtained by applying the same requirements ($z = d$ and $\omega t = \pi$) to Eq. (4.2a) [58]. Together with the relation for non-relativistic kinetic energy $E_{\text{kin}} = \frac{1}{2} m v^2$ and Eq. (4.3) [84], the equivalent impact energy Σ_{g} is given by

$$\Sigma_{\text{g}} = \frac{1}{2} m_{\text{e}} \left(\frac{2e}{m_{\text{e}}} \frac{U_{\text{g}}}{\omega d} \cos\varphi + v_0 \right)^2 = \frac{1}{2} m_{\text{e}} \left(\frac{2(\omega d - v_0 \pi)\cos\varphi}{\pi \cos\varphi + 2\sin\varphi} + v_0 \right)^2 \tag{4.9}$$

at those points U_{g}, that are enclosing the resonant condition for a certain gap distance d. Curves of the functions $\Sigma_{\text{g,min}} = \Sigma(\varphi_{\text{g,max}})$ and $\Sigma_{\text{g,0}} = \Sigma(\varphi = 0)$ are illustrated in Figure 4.4 with respect to d. For the fixed operating frequency $f = 2.998\,\text{GHz}$ and constant escape velocity v_0, in accordance with 4 eV mono-energetic release energy, a particular gap distance results in the

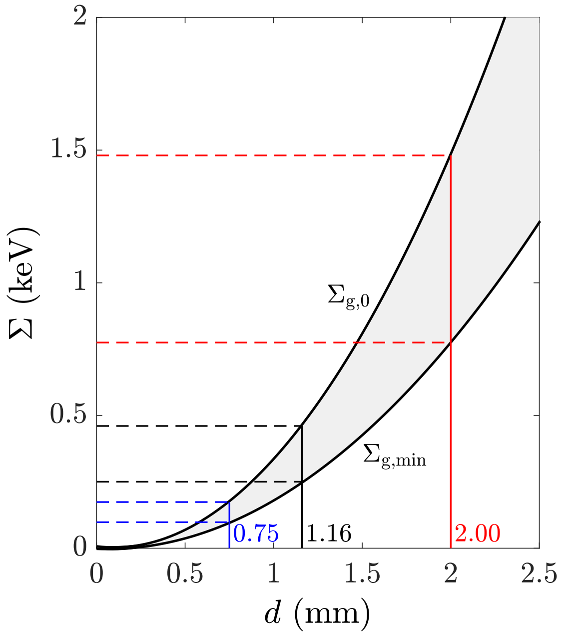

Figure 4.4: Equivalent maximum ($\Sigma_{\mathrm{g,0}}$) and minimum ($\Sigma_{\mathrm{g,min}}$) impact energy of an electron in fulfilment of the resonance condition for different gap distances d.

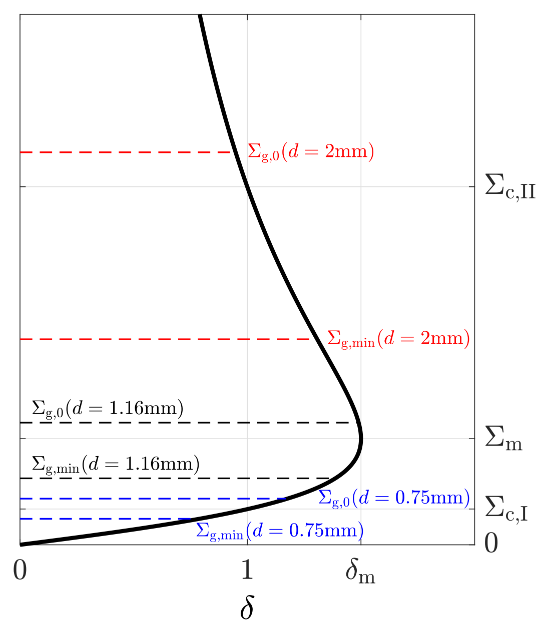

Figure 4.5: Generic secondary yield δ as a function of impact energy Σ, plotted on the x-axis, for the assignment of equivalent impact energies at different d.

necessary equivalent impact energy span $\Delta\Sigma_{\mathrm{g}} = [\Sigma_{\mathrm{g,min}}, \Sigma_{\mathrm{g,0}}]$. This can be compared to the corresponding SE yield δ of an associated material. Secondary electrons are generated according to the SEY at given impact energy Σ, illustrated in Figure 4.5. Thereby, charge amplification by periodic secondary emission in regards to Eq. (4.8), combined with power losses due to beam loading [89], can lead to a stationary multipacting condition resulting in a saturated beam current under the right circumstances. It is further described in the following.

4.2 Steady State Multipacting

When all necessary criteria described in Section 4.1.1 for resonant two-sided multipacting are fulfilled, a stationary state can be achieved. The level of MP current saturation is reached in about 20 ns, if the total SE gain G is above unity [58], which involves the accumulation of free electrons inside a narrow phase-region. Effects of accompanying beam loading and repulsive space charge forces between electrons on the resonance condition are subject to this section.

4.2.1 Power Saturation by Beam Loading

For the exemplary inclusion of a beam loaded cavity into the equivalent circuit model of two-sided multipacting inside the resonator, Kishek and Lau [89] implemented a sheet-like electron distribution of surface charge density σ to model the multipactor discharge. It can be seen as a more detailed version of the resonator circuit from Figure 3.5, also taking the mutual interaction of a time-dependent multipacting current $I_{\mathrm{m}}(t)$ into account. An illustration of the applied

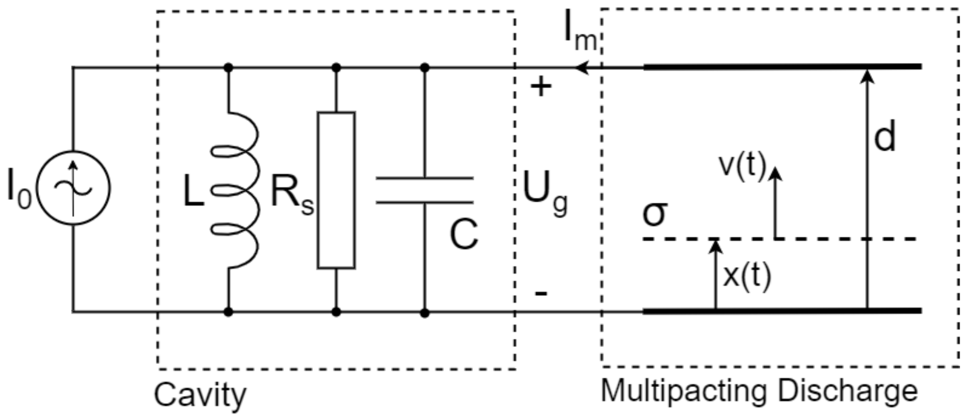

Figure 4.6: Equivalent circuit of a resonant cavity including the single-sheet model for a mutual interaction with multipacting discharge. Figure made in analogy to [89].

circuit diagram is given in Figure 4.6. In consideration of the RLC-circuit, the normalised gap voltage U_g is described by

$$\left(\frac{d^2}{dt^2}+\frac{1}{Q}\frac{d}{dt}+1\right)U_\mathrm{g}(t)=\frac{d}{dt}\left[I_0\sin(\omega t+\varphi)+I_\mathrm{m}(t)\right], \tag{4.10}$$

driven by the idealised cavity current of amplitude I_0 [89]. The current induced by multipacting discharge $I_\mathrm{m}(t)$ is directed oppositely and is responsible for beam loading of the cavity, so that an increase of I_m results in a decreasing gap voltage at constant external power supply. It is found that for quality factors $Q>10$ a stationary multipacting situation occurs, where the equivalent impact energy of the electron sheet approaches $\Sigma_\mathrm{c,I}$ asymptotically in time and the current thereby saturates as a result of loading [89].

To explain the resistive response of multipacting discharge and the transient interaction with the cavity, leading to steady state MEG operation, Figures 4.4 and 4.5 are consulted once more. There, three points assigned to different gap distances, which lead to distinct impact situations in regards to Σ_g, are selected illustratively:

I) $\Sigma_\mathrm{g,0}>\Sigma_\mathrm{c,II}>\Sigma_\mathrm{g,min}$ (red lines):
Electrons that are accelerated to equivalent impact energies greater than $\Sigma_\mathrm{c,II}$ generate a higher number of SE in comparison to the incident primary electrons each half-cycle. As a result, power losses due to beam loading (Eq. (3.47)) increase, thus the cavity voltage drops by a larger Q_L (Eq. (3.36)) and therewith the gap voltage U_g as well. Consequently, even more secondaries are created until Σ_g is out of resonance and the beam current vanishes. For impact energies smaller than $\Sigma_\mathrm{c,II}$, the total SE gain decreases, but Σ_g drops out of the resonance condition towards higher energies for increasing U_g with time.

II) $\Sigma_\mathrm{g,0}>\Sigma_\mathrm{c,I}>\Sigma_\mathrm{g,min}$ (blue lines):
For the same reason as described in (I), the available cavity voltage pushes U_g, hence Σ_g, towards $\Sigma_\mathrm{c,I}$ for all equivalent impact energies around $\delta(\Sigma)=1$. The total SE gain G saturates within that energy range, since it counteracts changes in beam power consump-

tion by alterations in the beam current, while also satisfying the resonance condition. As a consequence, $\Sigma_{c,I} \in \Delta\Sigma_g$ determines a stationary multipacting condition for MEG operation, formerly reported by [85] and others.

III) $\Sigma_{g,0} > \Sigma_m > \Sigma_{g,min}$ (black lines):
All equivalent impact energies within resonance are resulting in an increasing charge density, since $\delta(\Sigma_g) > 1$. The resulting voltage drop then leads to Σ_g falling out of the resonance condition, but charge amplification is fast due to the high overall SE yield. Potentially, there could be a quasi-stable working point, where sufficiently fast filling times are leading to an increased beam intensity, so that Σ_g remains inside the boundaries of resonant gap voltages.

4.2.2 Accessibility of the Steady State

While looking at steady state multipacting with equivalent impact voltages around the first cross-over point $\Sigma_{c,I} \in \Delta\Sigma_g$, according to [90], maximum gap voltages chosen inside the boundaries of $U_{g,min}$ and $U_{g,0}$ do not necessarily result in current saturation. Moreover, it is reported that steady state multipacting is not restricted to that voltage region in consideration of the transient build up of the gap voltage in the cavity, whose filling time constant τ largely depends on the quality factor Q (cf. Eq. (3.28)), following

$$\tau = 2Q/\omega_0. \tag{4.11}$$

On the time scale of τ, the process of raising field gradients in the surface gap is competing with the power loss P_{beam} by the increasing multipacting current, that builds up at a rate depending on the slope of the SEY curve $d\delta/d\Sigma$ around $\Sigma_{c,I}$ (cf. Figure 2.8). Steady state multipacting can be achieved, if both rates are comparable [90]. Thereby, the effective gap voltage, illustrated with help of Figure 4.7, has to transiently pass through the narrow range defined by the resonance condition and one of three situations might occur:

(a) The gap voltage U_g is leaving the boundary $U_{g,0}$ before a sufficiently large multipacting current is generated. Thereby, beam induced power losses are small in comparison to the fast energy storage accompanied by a rapidly changing gap voltage, which is the case for small Q factors.

(b) Filling time and charge amplification are of the same order, so that the cavity load reduces U_g sufficiently quick. As a result, voltage and multipacting current I_m are balanced and the steady state is sustained further on.

(c) Beam induced cavity loading is the dominating process, when the charge density growth rate (high δ_m, or low $\Sigma_{c,I}$) is large compared to the change in voltage. Consequently, I_m pushes the gap voltage down below $U_{g,min}$ and the electrons drift outside the allowed phase region. Subsequent voltage increase, as the cavity load disappears, then leads to a repetition of the whole process.

Multipacting driven electron guns are designed to reach steady state operation. For that purpose, cavity structures of large Q-values ($Q \sim 1000$) are proposed to be suitable for current saturation in the resonant voltage range [90]. However, high SE yield materials may offset smaller Q.

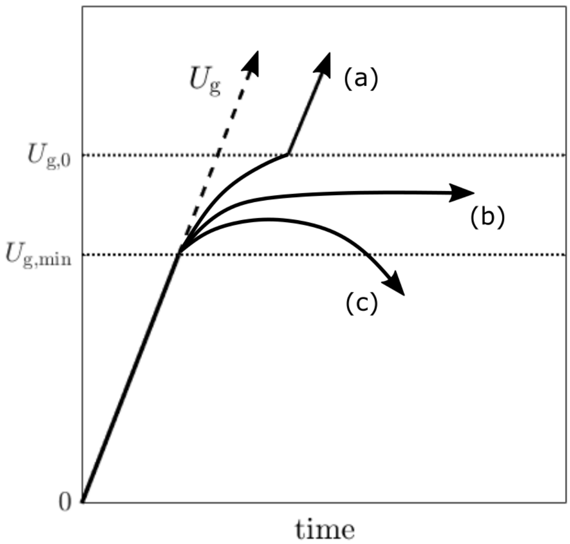

Figure 4.7: Build-up of the gap voltage U_g, influenced by an increasing charge density due to multipacting, with time. Three possible things can happen, dependent upon the rates of energy storage in the cavity and charge growth:

(a) Break-through
(b) Steady state multipacting
(c) Quench

According to [90], the temporal evolvement of U_g without multipacting is the same for all cases.

4.2.3 Inclusion of Space-Charge Forces

To this point no inter-particle interaction in terms of self fields inside the electron distribution is taken into account. This section describes the resulting forces between charged particles for the case of electrons inside a finite space between two planar metallic surfaces and gives insight into the maximal obtained current density following the law of Child and Langmuir [91, 92]. Furthermore, the influence of space charge fields on the resonant condition and charge density of two-sided multipacting in an MEG is calculated approximately.

In general, space charge forces are due to electromagnetic fields between uniformly charged particles of density $\rho(r)$ [27]. The fields are thereby exerting a force on the particle at radius $r = \sqrt{x^2+y^2}$, given by the Lorentz force from Eq. (3.3). On the one hand side, there is Coulomb interaction resulting in repulsive forces and on the other hand there are also attractive forces induced by the magnetic field of the particles (e.g. electrons) in motion parallel to each other with the velocity v. The resulting force acting on a charge q in radial direction, transverse to $\mathbf{v} = v_z$, can be expressed by [93]

$$F_r = qE_r(1-\beta^2) = \frac{qE_r}{\gamma^2}, \tag{4.12}$$

where $\beta = v/c$ and E_r is the radial electric field component

$$E_r(r) = \frac{1}{\varepsilon_0 r}\int_0^r \rho(r')r'dr'. \tag{4.13}$$

A detailed derivation, together with the inclusion of specific particle distributions, and also space charge effects on the beam dynamics in particle accelerators, can be found in [93, 94] for instance.

Equation 4.12 shows that for non-relativistic velocities ($\beta \approx 0$) the Coulomb term has a major influence on the particle distribution. Thus, a transverse blow-up of the electron beam inside an MEG is expected. However, for the MEG principle in Figure 2.11 it is intended as well, since transverse electron motion leads to transmission of the beam outwards of the gun cavity. Coming along with it is a reduced charge density each full RF cycle, affecting the steady multipacting state described in Section 4.2.2.

Child–Langmuir Law

Current limitations due to space charge fields have already been touched on basically by the introduction of electron sources in reference to the planar diode configuration from Figure 2.3. In fact, there is a maximum obtainable charge density in the vicinity of electron emitting surfaces with distance d, which can be accelerated by a given voltage U_0 [27]. For the geometrically simple cathode configuration of a conventional thermionic gun, as it is presented exemplarily in Section 2.2.1, the limiting current density J follows the law of Child-Langmuir [91, 92]:

$$J_{\mathrm{cl}} = \frac{4}{9}\varepsilon_0\sqrt{\frac{2e}{m_{\mathrm{e}}}}\frac{U_0^{3/2}}{d^2}. \tag{4.14}$$

The scaling of current density with the voltage to the power of 3/2 is a fundamental law in the field of vacuum electronics. A derivation can be found in [27] for example. However, since the law of Child-Langmuir describes an equilibrium state, but U_0 is constantly changing in the operation of an MEG and also the electrons' time of flight is different within one RF period, Eq. (4.14) is not applicable in the context of this work [95].

Further theoretical investigations on this topic, including finite initial escape velocities, relativistic applied voltage, and quantum mechanical effects, are described in [96] collectively. From multidimensional calculations they also show that non-uniform emitter structures enhance the peak current density and J is not longer a simple function of U_0 and d.

Influence of Space Charge Effects on the Resonant Condition

Besides the effect of space charge fields on the phase space in transverse coordinates, it also acts on the electron momenta in beam direction, thus the idealised model of a thin flat sheet of charges is upset [58]. Space charge forces on their own have a phase-dispersing effect longitudinally, pushing electrons away from the centre of the bunch. Inside an MEG specifically, the equation of motion (4.1) of a single electron can rather be described with an additional space charge field E_{sc} [13], so that

$$\ddot{z}_{f,t} = \frac{e}{m_{\mathrm{e}}}\left[E_0\sin(\omega t + \varphi_{f,t}) \pm E_{\mathrm{sc}}\right]. \tag{4.15}$$

In this representation, the subscripts f and t refer to electrons in the front and tail of the bunch, respectively. Under the assumption of a much larger beam extent in transverse direction, compared to the narrow phase region of resonant multipacting, the self-field on either side is approximately $E_{\mathrm{sc}} = \sigma/2\varepsilon_0$, whereby σ is the surface charge density of the electron sheet [58].

By solving Eq. (4.15), similar to Section 4.1.1, and applying the same resonance criteria ($\omega t = \pi$, $z = d$), the gap voltage with respect to the charge density σ for initial phases $\varphi_{f,t}$ yields

$$U_{\mathrm{g}}^{f,t} = \left(d - v_0 \frac{\pi}{\omega} \mp \frac{e\sigma\pi^2}{4\varepsilon_0 m_{\mathrm{e}}\omega^2}\right) \frac{m_{\mathrm{e}}\omega^2 d}{e\left(\pi\cos\varphi_{f,t} + 2\sin\varphi_{f,t}\right)}, \tag{4.16}$$

giving the resonance condition in consideration of space charge (cf. Figure 4.8). The available phase range is still determined by φ_{min} and φ_{max}, thus $\varphi_f \geq 0$ (for $v_0 = 0$) and $\varphi_t \leq \arctan\frac{2}{\pi}$ for electrons in the front and tail of the bunch, that satisfy Eq. (4.16).

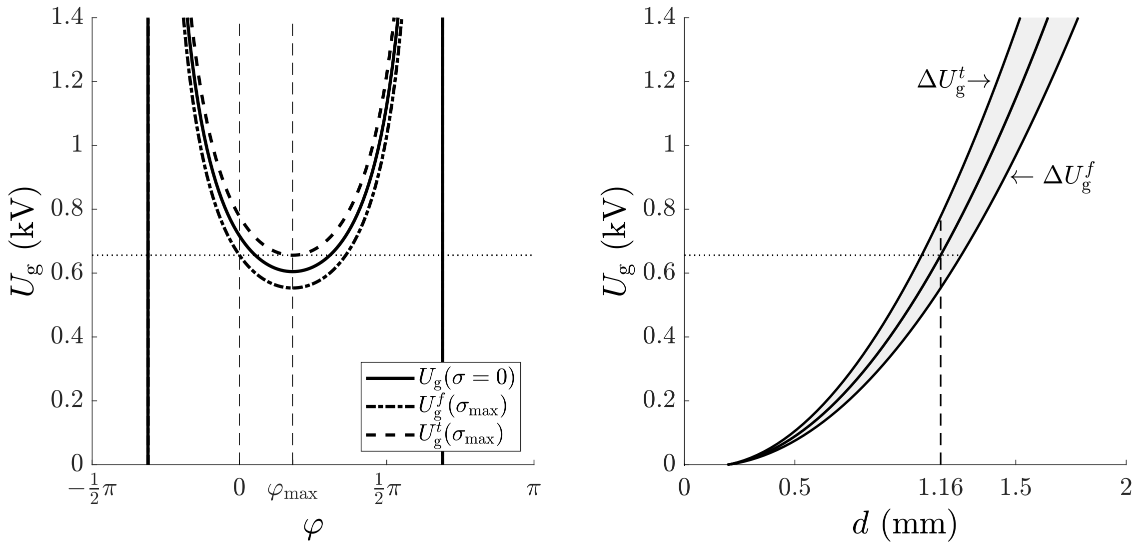

(a) Gap voltage versus emission phase for fixed $d = 1.16\,\mathrm{mm}$, including zero and maximum charge density

(b) Gap voltage versus gap distance for front (f) and tail (t) electrons, at $\varphi_{\mathrm{min}} = 0$ and φ_{max}, including maximum charge density

Figure 4.8: Resonant gap voltages $U_{\mathrm{g}}^{f,t}$ as a function of emission phase φ (a), and gap distance d (b), under the influence of space charge with up to the maximum density σ_{max}. Operational parameters are $\omega = 2\pi \cdot 2.998\,\mathrm{GHz}$ and $E_{\mathrm{esc}} \simeq 4\,\mathrm{eV}$, the same as for Figure 4.2.

Figure 4.8a shows that by raising the charge density σ, a point is reached eventually, where the resonance condition is cancelled for some electrons in the front ($U_{\mathrm{g}}^{f}(\varphi = 0)$) and tail ($U_{\mathrm{g}}^{t}(\varphi_{\mathrm{max}})$) simultaneously. There, it is indicated by the horizontally dotted line crossing both gap voltage variations for the particles widest apart from each other in phase. This is further highlighted in Figure 4.8b, presenting the resonant voltage ranges $\Delta U_{\mathrm{g}}^{f} = [U_{\mathrm{g}}^{f}(\varphi = 0), U_{\mathrm{g}}^{f}(\varphi_{\mathrm{max}})]$ and $\Delta U_{\mathrm{g}}^{t} = [U_{\mathrm{g}}^{t}(\varphi = 0), U_{\mathrm{g}}^{t}(\varphi_{\mathrm{max}})]$ for front (f) and tail (t) electrons separately as functions of the cathode distance d.

An approximation of the maximum charge density σ_{max}, beneath which a resonance condition for all electrons inside $\Delta\varphi = [0, \varphi_{\mathrm{max}}]$ could exist, can thus be obtained by solving

$U_g^f(\varphi_f = 0) = U_g^t(\varphi_t = \arctan\frac{2}{\pi})$ for σ:

$$\sigma_{\max} = \left(\frac{2(v_0\frac{\pi}{\omega} - d)}{\frac{\sqrt{\pi^2+4}}{\pi} + 1} - v_0\frac{\pi}{\omega} + d \right) \frac{4\varepsilon_0 m_e \omega^2}{e\pi^2} . \tag{4.17}$$

The result is quite consistent with Vaughan [58], or Yang *et al.* [84], who used slightly different methods. However, it is worth mentioning that $\sigma_{\max}$ and hence the current density J is a linear function of the gap distance d. Once $\sigma_{\max}$ is reached electrons occupy the full phase space $[\varphi_{min}, \varphi_{max}]$, which is also the case for even higher charge densities. Then, the effect of space charge debunching overcomes the self-bunching mechanism from Section 4.1.2 and the total SE gain reduces. Consequently, phase dispersion puts a limit on the space charge density [97].

It is found that space charge limitations generally have a minor impact on the saturation of multipacting discharge in comparison to the beam loading effect, concluded from numerical calculations [98]. The following charge tracking simulations regarding MEG performance and parameter studies are taking both effects into account.

5 Particle Tracking with ASTRA

”A space charge tracking algorithm” (ASTRA) is a program freely available for non-commercial use, that simulates movement of electrically charged particles under the influence of external and internal fields. It requires an initial particle distribution file as well as input decks containing information about general tracking instructions, beam line elements and settings for the space charge calculation. Furthermore, the possibility of secondary electron emission from beam line elements is implemented by Eq. (2.23), based on the model of Furman and Pivi [50]. A comprehensive documentation covering all user related issues is provided by [99].

However, the tracking is based on the integration of differential equations within discrete time steps by a Runge-Kutta method [100, 101, 102]. After each calculation the phase space information of all particles is stored and will be used for the subsequent integration step. All particles are treated as macro particles carrying an adjustable amount of multiple elementary charges and masses for better efficiency by reducing their number. Ultimately, the position and momentum of initially and newly created particles can be read out at specific times or locations, together with their status information.

With use of ASTRA, the content of this chapter is about proving the possibility of MEG operation in the numerical model and to provide an estimation of the mechanical parameter space, needed for the concrete cathode design, in our electron gun.

5.1 Starting Conditions of the ASTRA Simulations

Since the starting conditions of the tracking simulations must be reasonably comparable to an actual experimental procedure, the following sections give a statement on their implementation in ASTRA. That includes the external field configuration, the geometry of apertures and also the time-dependent power consumption of the cavity in regards to beam loading.

5.1.1 Cathode Geometry and Initial Field Distribution

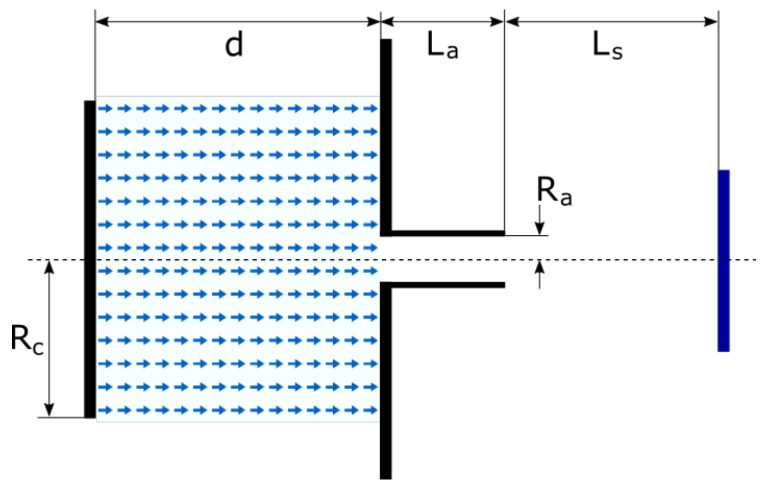

Figure 5.1: Cathode-aperture configuration with uniform field distribution for ASTRA.

The multipacting areas are set by radially symmetrical surfaces as schematically shown through the two opposing black walls in Figure 5.1. There, the left side with radius R_c remains impermeable, whereas an aperture of radius R_a and length L_a can be formed on the right side for electrons to pass through. Particles travel towards a screen at distance L_a, where they are detected. Between the two cathodes, separated by the gap distance d, a uniform electric RF field is applied initially to model the externally accelerating forces inside the gap. It is indicated by the blue arrows in Figure 5.1. Since the tracking studies in this chapter first and foremost aim for a qualitative understanding of the multi-particle resonance condition, a more accurate and realistic field distribution is avoided for the sake of simplicity and computation speed.

5.1.2 Beam Loading and Cavity Parameters

To model the field amplitude response to beam loading, it is necessary to estimate the stored field energy inside the cavity according to Eq. (3.30). Because of the more complex cavity designs in reality, with the fact that not only the space between both cathode surfaces will contribute to the mode propagation, this is a non-trivial issue. By looking ahead to Section 6.1, where actual design considerations are discussed, simulations including the model in Figure 6.2b, using *CST Microwave Studio®*, suggest an energy storage of $W_\mathrm{d} \simeq 4.06 \cdot 10^{-7}\,\mathrm{J}$ for a gap distance of $d = 1.2\,\mathrm{mm}$, a cathode radius $R_\mathrm{c} = 1.5\,\mathrm{mm}$ and a maximum field gradient of 1 MV/m. It is found that the stored energy W thereby scales with d^2, so it is set to

$$W(d) = 4.06 \cdot \left(\frac{d}{1.2\,\mathrm{mm}}\right)^2 \cdot 10^{-7}\ \mathrm{J} \tag{5.1}$$

per $(\mathrm{MV/m})^2$ for all simulations hereafter as long as R_c is not changed from 1.5 mm.

The other important parameters for ASTRA in this context are related to power transmission into the cavity. Most notably the filling time input parameter *C_Tau*(), which is used to configure the loaded quality factor following Eq. (4.11).

5.2 Numerical Determination of the MEG Resonance Condition

Besides the electromechanical parameters mentioned earlier, an initial particle distribution is another essential aspect. Within the settings of ASTRA it is possible to create such a starting distribution in a number of ways, either by positioning all macro particles at their respective starting locations, or originating at an emissive surface with certain time delay.

For the MEG case it is assumed that the charge build-up by multipacting avalanches is large compared to the number of initial electrons, thus a uniform distribution of pre-existing particles across the cathode gap volume with small total charge is implemented for the simulations. Additionally, the start of particle tracking is generally set to a point, where the maximum field gradient E_0 is reached already, so that the resonance condition can be obtained immediately. This behaviour is confirmed by the experimental observation of stable resonant multipacting, which occurs mostly after the cavity is already filled completely (cf. Chapter 7). To show the ASTRA tracking procedure Figure 5.2 is presented, where the trajectory of one initial probe particle starting inside the resonant phase region is shown exemplary. After the impact on either surface, secondary macro electrons are emitted based on the implemented material properties with a user defined initial kinetic energy of 4 eV isotropically and without delay time. Here, only the path of one SE particle out of subsequent generations is shown. Their overall increasing distance in r indicates a higher charge density towards the cathode centre. Since the algorithm considers all created particles individually, also higher multipacting orders including additional single-sided discharge, as described by [103, 104], can be taken into account. Parameter studies regarding the resonant condition in Section 5.2.1 imply the situation in Figure 5.1, but with closed aperture ($R_\mathrm{a} = 0$) for avoiding charge losses through the hole.

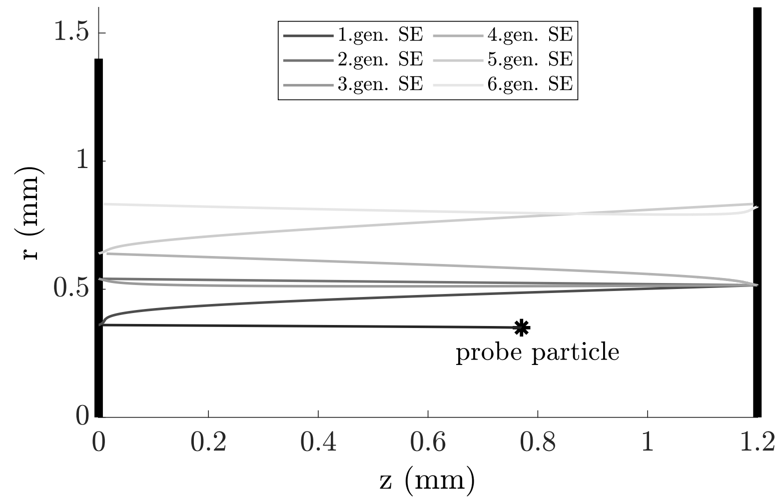

Figure 5.2: Trajectory of a probe particle satisfying the resonance condition. The distance to the cathode centre $r = \sqrt{x^2 + y^2}$ is plotted against the z-coordinate in beam direction. A secondary particle of subsequent generation is indicated by the brighter path, respectively.

5.2.1 Parameter Studies

The collective particle movement is investigated by variation of the listed input parameters in Table 5.1. When performing a certain set of simulations in regards to a specific input variable, the other parameters are included with their default value, whereas the operating frequency is always set to 2.998 GHz. As the figure of merit in evaluation of the simulation results, the amount of active charge is taken into account, as exemplarily presented in Figure 5.3. For the upper part the number of active particles at given time is directly related to the total charge q_g existing inside the cathode gap volume. Over the course of about 70 - 80 RF cycles the charge is evaluated at incremental time steps of multiple Runge-Kutta time intervals. The multipacting resonance condition can be derived from the momentary acceleration field gradient E during stationary multipacting, which is shown in the bottom part of Figure 5.3, accordingly.

Parameter		Default Value	
Cathode Distance	d	1.2 mm	Gap length between the two MP surfaces.
Max. Field Gradient	E_0	0.7 MV/m	Initial electric field strength $E_0 = U_0/d$.
Quality Factor	Q_L	100	Loaded cavity quality def. by $Q = \tau\omega_0/2$.
Max. SEY	δ_m	2.0	Maximum SE yield of given material.
Max. Yield Energy	Σ_m	400 eV	Impact energy at point of highest SEY.
SEY Curve Shape	s	1.7 (unchanged)	Free adjustment parameter from Eq. (2.23).

Table 5.1: Overview of key input parameters under investigation in the ASTRA tracking studies.

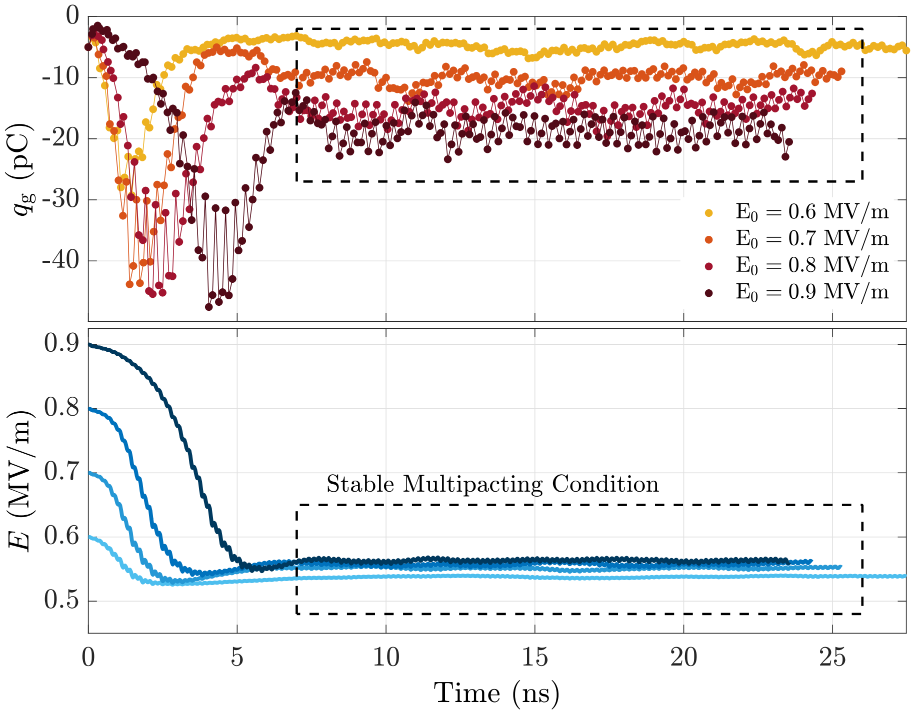

Figure 5.3: Total charge q_g (top) and field gradient E (bottom) inside the gun cavity as functions of time with the default settings from Table 5.1. Simulations including different initial gradients E_0 of 0.6 - 0.9 MV/m are compared.

This first example highlights four simulations with different starting gradients, which lead to steady state multipacting after a couple of nanoseconds. Larger fields in the beginning accelerate the particles to higher kinetic impact energies and thus their number increases significantly due to the SE yield. At the same time the cavity gradient is reduced because of beam loading until the charge density decreases again. Eventually the condition is met, where a steady state (cf. Section 4.2) is obtained and the total charge remains nearly constant with time. While doing so, the momentary field maintaining the stable multipacting condition is equal to the acceleration field inside the cavity E_{cav} and may draw conclusions from the actual resonant gap voltage. All excess energy is thereby transferred to the particles and consumed by the additional load on the system, meaning that at this point no other loss mechanisms are taken into account.

Cathode Distance Without paying attention to the RF properties or material characteristics, the resonance condition is mainly determined by the combination of field gradient and cathode distance at any operating frequency.

Simulation results of the resonant gap voltage U_{cav}, derived from the cavity field $E_{\mathrm{cav}} = U_{\mathrm{cav}}/d$, are plotted against d for different initial gradients in Figure 5.4. Only data leading to resonant multipacting is shown here. It is in good agreement to the overall shape of the expected gap voltage from Eqs. (4.3) and (4.16). However, a slight offset $a = 70\,\mathrm{V}$ as well as a correction factor $b = 0.82$ are included to fit the data more accurately. This is most likely due to the accumulation of several uncertainty factors, such as the assumed energy storage from *CST*, the set starting condition of the rapid charge increase, or its synthetic execution by the code. Different filling times are also affecting the accessible gap voltage range, since the ratio of power loss from beam loading - to - charge multiplication is changed. Besides this variety of influences, which can not be accounted for easily, all simulations are consistent relative to each other. Thus, the concept of a resonant multipacting condition is verified for ASTRA calculations in an MEG configuration, as it is presented here.

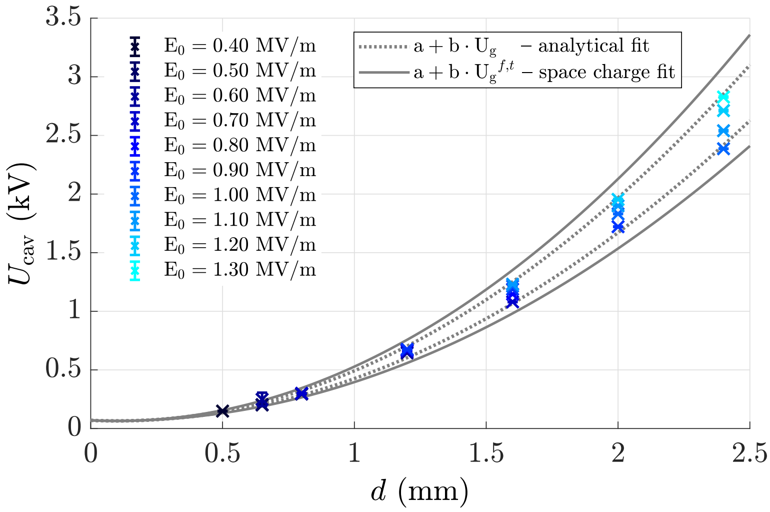

Figure 5.4: Gap voltage U_{cav} for several combinations of initial field gradient E_0 and gap distance d in presence of resonant multipacting. The grey lines represent a modified fit of the analytically derived gap voltage with ($U_{\mathrm{g}}^{f,t}$), and without space charge fields (U_{g}).

Figure 5.5 shows the corresponding total charge q_{g} inside the gap volume. For an easier reference to the cathode distance they are presented as functions of the initial RF gap voltage U_0. Thereby, the gun charge increases nearly linearly with U_0 due to the availability of more power for particle acceleration and thus better compensation of beam loading. Consequently, more particles, that are accelerated to sufficient equivalent impact energies, can exist in the phase space of resonant multipacting and will further generate secondary electrons. For distances between 0.5 and 0.8 mm, the simulated charge increase is constant, whereas it does not follow the same trend for larger d, including an offset. Even though the total charge increases for each d, its density scales down due to significantly larger bunch sizes. Together with Figure 5.6,

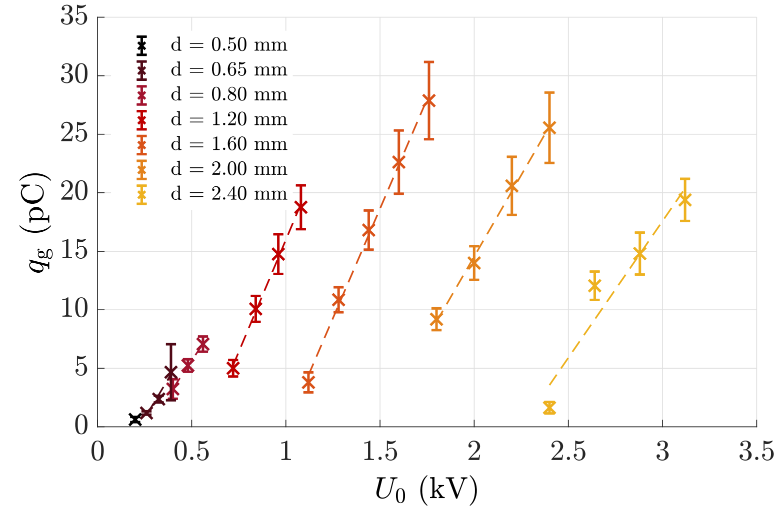

Figure 5.5: Total gap charge q_g as a function of the initial gap voltage U_0 for different cathode distances d. An error estimation is based on statistical variance of the raw data. The dashed lines are linear fits as a guide for the eye.

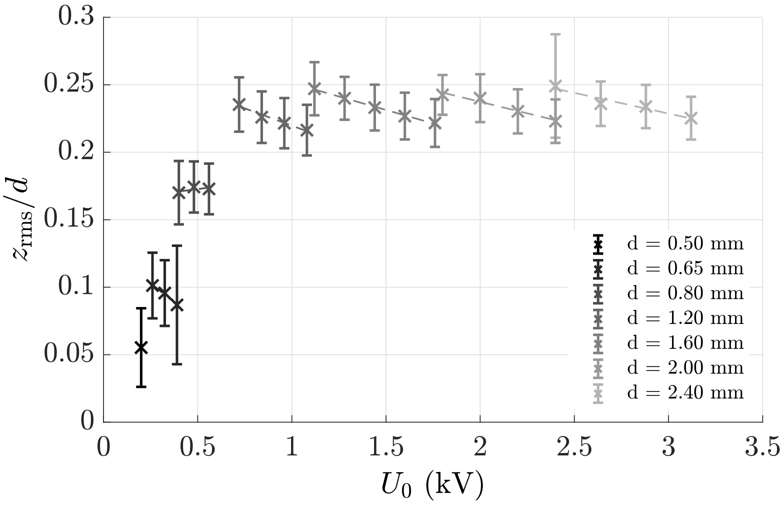

Figure 5.6: Ratio of rms bunch length z_{rms} to the gap size d as a function of the initial gap voltage U_0 for different distances d. The data presented in this figure corresponds to the aforementioned simulations in Figure 5.5.

which indicates how much space inside the gap is occupied by particles, this is hinting at a smaller contribution of the particles to further secondary generation at resonance. Starting from $d = 1.2$ mm, space charge forces blow up the bunch longitudinally above the phase limit given by the resonance condition. Thereby, multipacting can still be achieved at larger gap sizes, despite not being expected in regards to Section 4.1.3, since there can still be enough electrons with kinetic energy to keep the total SE gain above one. Also higher order multipacting modes could help keeping the resonance condition alive there, but it is not recognised.

Q Factor In ASTRA, time-dependent RF power coupling into a cavity structure is controlled by the filling time constant, which is connected to the loaded quality factor Q_L by Eq. (4.11), and the starting time of particle tracking within that time period. The loaded Q also holds information about the coupling strength in the absence of other external loss mechanisms via Eq. (3.36). A smaller Q_L, and thereby stronger coupling, will form the accelerating field gradient inside the structure faster.

The qualitative results of particle tracking, including various coupling situations, are presented in Figure 5.7. Upon reaching steady state multipacting the acquired gap charge is increased for smaller values of Q_L, whereas it is nearly equal for all Q_L during the initial build-up period within the first few RF cycles. It can also be seen that the responsive field gradient is higher at small Q_L-values in the steady state. This leads to the conclusion that faster cavity filling is able to compensate for power losses by beam loading earlier, thus building a sustainability of the cavity gradient when more charges are created. In the steady multipacting state more power is available for particle acceleration and their number increases similar to the case of larger initial gradients shown in Figure 5.3.

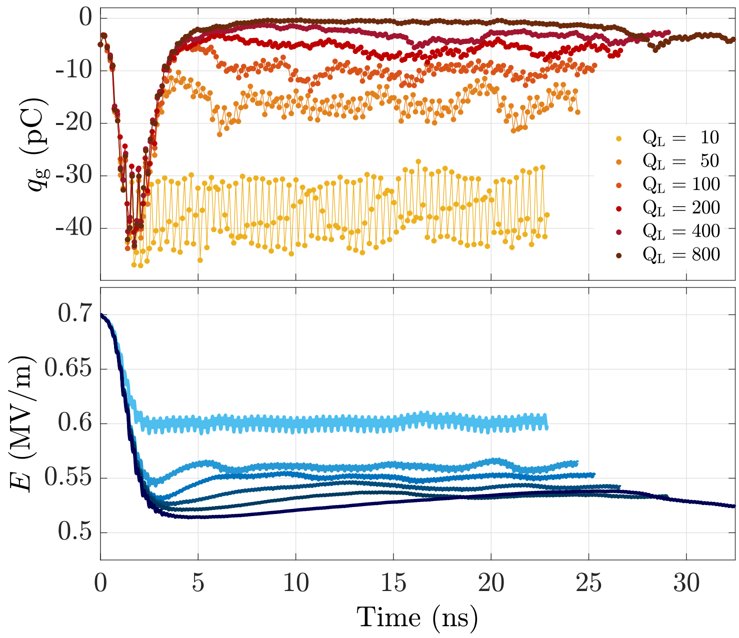

Figure 5.7: Total gap charge q_g (top) and corresponding field gradient E (bottom) simulated with time and for various values of the loaded quality factor Q_L in the range of 10 to 800. Other involved parameters are set to their default value listed in Table 5.1. Darker coloured curves in the upper frame belong to the darker colours in the bottom frame, respectively.

SE Yield In consideration of resonant multipacting in the steady state, tracking simulations regarding material depending characteristics were performed as well. Accessible parameters for the ASTRA calculations are the maximum SE yield δ_m and the primary energy value Σ_m of its appearance in the SEY curve in particular. Tracking results evaluating these two important parameters can be found in Figure 5.8.

By increasing the maximum yield up to $\delta_m = 5$, also the total charge builds up more and more rapidly, which results from the heavily increased SE probability in the cathode layer. In a consistent way the corresponding electric field strength falls off faster in response to increased beam loading. It is also remarkable that a smaller cavity gradient is sufficient for the preservation of higher total gap charge after the steady state is reached. Fitting into the picture of SE outside the resonance condition in case of large cathode distances ($d > 0.8$ mm), it seems likely that even more secondary electrons are created within a wider phase range of one RF half-cycle, or even travel for multiple periods. Additionally, the stationary secondary generation around $\Sigma_{c,I}$ is at smaller primary energy with greater δ_m and thus particles undergo weaker acceleration in general, which further enhances their number by mitigated beam loading.

Plotted in Figure 5.8b is the development of charge and gradient under variation of the impact energy Σ_m at a fixed maximum yield of $\delta_m = 2$. It highlights the form of accessing

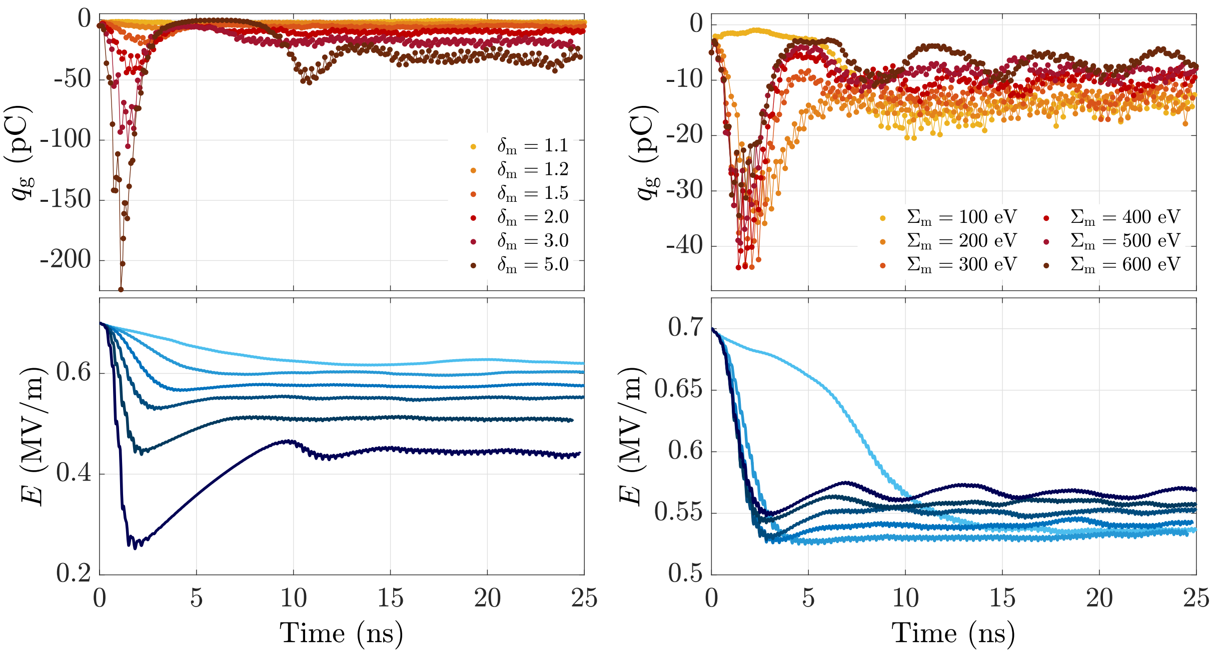

(a) Maximum SE yield δ_m (b) Maximum yield energy Σ_m

Figure 5.8: Total gap charge q_g (top) and corresponding field gradient E (bottom) simulated with time and for different maximum secondary electron yield δ_m (a), and a number of different maximum yield energies Σ_m (b).

into the steady multipacting state in different ways, since the shift of Σ_m influences the slope at $\delta(\Sigma_{c,I})$ more significantly than δ_m. At larger values, $\Sigma_m = 600\,\text{eV}$ most notably, particles need an overall higher impact energy to constantly maintain resonant multipacting. Thereby, the rates of charge increase and power loss move apart from each other, based on a slower charge growth around $\delta(\Sigma_{c,I})$. As a consequence, the cavity gradient destabilises. However, at very small values of Σ_m the steady state is eventually not reached at all, since power losses are slow compared to the charge growth rate and thus the acceleration field might not be reduced quickly enough to fulfil the resonance condition.

5.3 MEG Output Current in the Uniform Field Approximation

For the numerical estimation regarding the average output current in this MEG model, the aperture radius R_a (cf. Figure 5.1) is set to a positive value. During the course of a simulation, numerous macro charges are ejected out of the gap volume due to transverse space charge forces, as illustrated in Figure 5.9. Both, active particles (red) and those lost in material (black), are tracked for the whole simulation period. Hence, their position information can be used to distinguish a contribution to the output current. Default values of the more geometrical parameters, that are added for the decoupling condition of particles into free space, are listed in Table 5.2. The aperture dimensions in particular are tied to the MEG cavity design and are therewith not easily modifiable in the actual experiment. In regards to the ASTRA input decks, however, options to structural changes in the model are generally available.

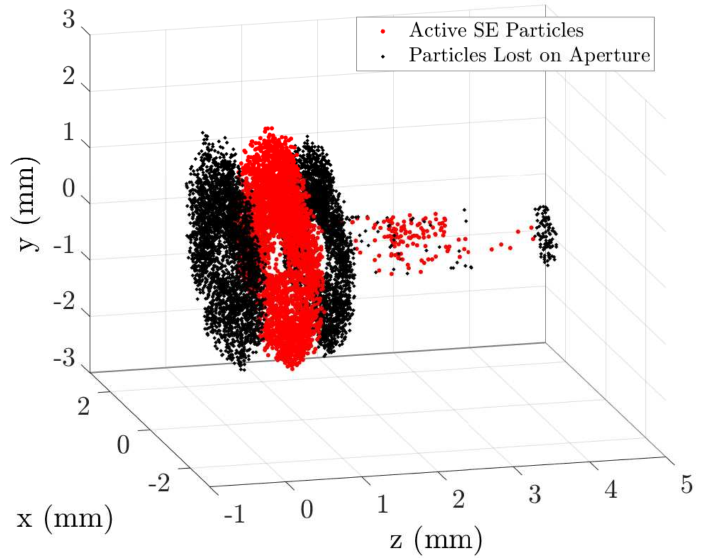

Figure 5.9: 3D snapshot of an oscillation particle distribution inside the cathode gap volume, including transmission through an aperture of 2 mm length. The colours differentiate if the charges are moving (red), or penetrated into the material for enabling secondary emission.

Parameter		Default Value	
Aperture Radius	R_a	0.5 mm	Transmissive part of the cathode surface.
Aperture Length	L_a	2.0 mm	Thickness of the transmissive surface.
Screen Distance	L_s	1.0 mm	Distance to the charge collection surface.

Table 5.2: Overview of additional geometric parameters for the MEG output current studies.

To illustrate the overall approach of tracking simulations under special consideration of output currents from the cavity, Figure 5.10 is presented. By opening the cathode aperture to $R_a = 0.5$ mm, the picture of total charge inside the gap (a) is supplemented by the amount of charge, that is collected on the screen, at distance L_s outside the gun (b). The derivative of that integrated output charge q_{out} leads to the respective current I_{out} (d), which has a peaked shape due to the bunched nature of the electron beam. Here, collective tracking data is shown for default settings under variation of the cathode distance d from 0.8 to 1.6 mm. It is indicating that the overall amount of gap charge strongly correlates with the output current. Further analysis including the variation of key input parameters is supposed to put this relation into a more quantitative context. An example of the corresponding input deck with $d = 1.2$ mm can be found in the appendix A.1, Figure A.1.

For the three distances $d = [0.8, 1.2, 1.6]$ mm, a current-voltage (I-U) characteristic is simulated by variation of the initial field gradient. The resulting curves are presented in Figure 5.11, whereby the current values are derived from the slope of the integrated output charge in the steady multipacting state. That gives the MEG current averaged over all electron bunches and RF cycles. Similar to the gap charge in Figure 5.5, also the output current increases with applied field gradient for all d separately. There is no clear functional dependency observable.

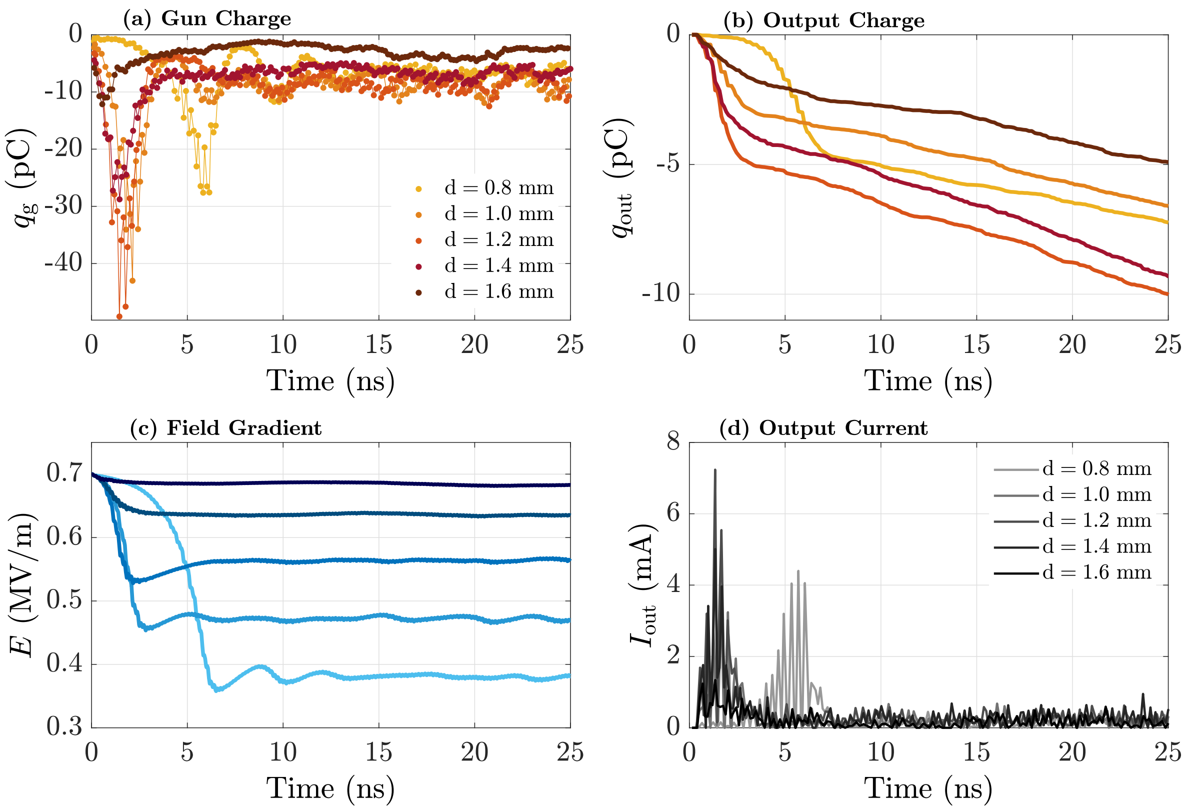

Figure 5.10: MEG simulation data under variation of the cathode distance d in default settings. The figure displays total gap charge (a), integrated output charge (b), the corresponding field gradient (c), and the output current $I_{out} = dq_{out}/dt$ (d) as a representation with time. Curves of the same colour level belong to the same simulation.

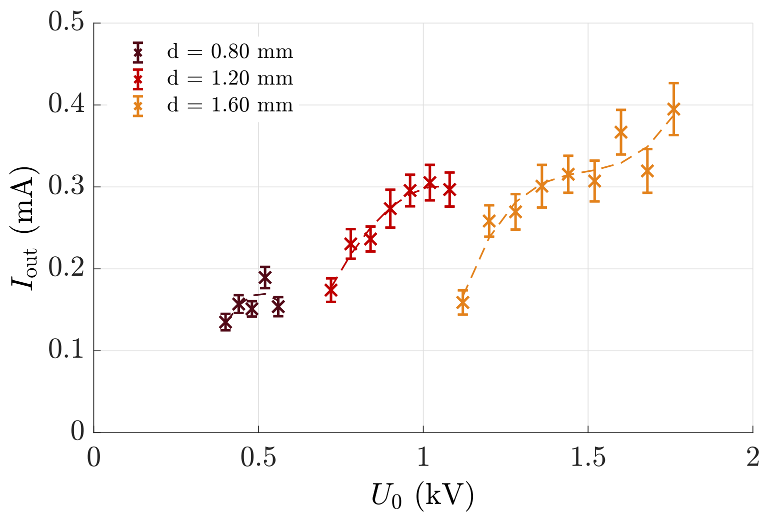

Figure 5.11: Simulated MEG output current I_{out} as a function of the initial voltage U_0 across the cathode gap for three different distances d. The dashed lines attached to each set are polynomial fits guiding the eye.

However, with larger gap voltage and therewith higher gap charge, the current growth rate is reduced. A possible interpretation could be that enhanced space charge fields at higher densities deflect the transverse particle motion stronger, thus single particles might get lost inside the aperture walls before leaving the gun. Furthermore, the cavity load gets reduced by increasing charge losses due to more leaving particles and a changed acceleration gradient could thereby impede the accessibility of steady state multipacting.

To test for current limitations caused by the aperture dimensions, simulations regarding R_a and L_a were carried out as an updated version with reference to [105]. Results involving the default settings of any other input parameter are given by Figure 5.12. At this point it has to be mentioned that $E_0 = 0.7\,\mathrm{MV/m}$ at $d = 1.2\,\mathrm{mm}$ does not generate gap charges significantly higher than $10\,\mathrm{pC}$, but the accessible longitudinal phase range of resonant multipacting must already be filled in accordance with Figure 5.6. Consequently, effects due to the presence of maximum obtainable charge densities are not taken into account on this occasion. This is moreover underlined by the simulations with changing aperture length L_a, where an increase from 0.5 to 3.0 mm has a minor impact on the output current. It can be expected that the number of particles lost on aperture will become more significant at considerably larger hole lengths with these specifications. On the other hand, an expansion of the aperture diameter has a much greater influence on the current. Its functional dependency is not entirely clear, but the trend follows a strong increase with R_a. In a similar way the circumference of the circular hole edge grows with R_a as well. One may conclude that the recorded multipacting current originates from SE around the inner part of the cathode-aperture configuration. A wider aperture would also lead to a bigger transverse beam size, because of the larger emission area.

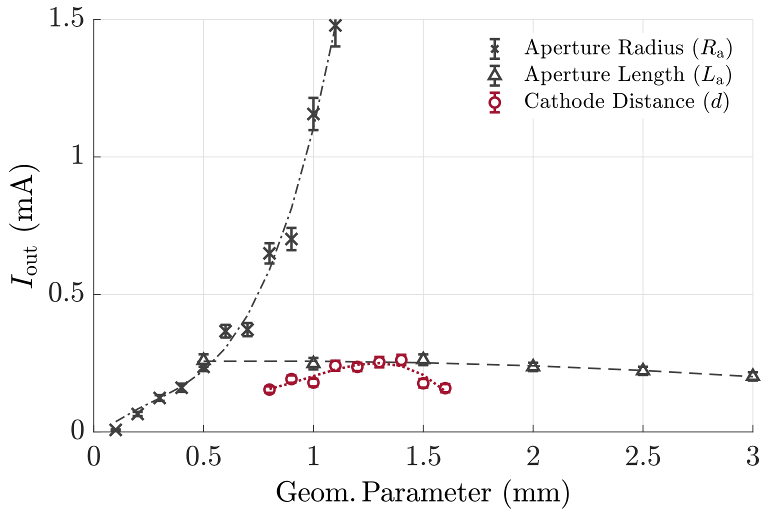

Figure 5.12: Simulated output current I_{out} in dependence of the size of key geometrical dimensions regarding the cathodes and aperture in the MEG cavity model.

At last, a simulation series including various gap distances is presented to illustrate its order of impact on the current in comparison to the aperture dimensions. Inside the gap volume, there is a higher current density for distances that are better adjusted to the resonance condition in terms of equivalent impact energies. Hence, more resonantly excited particles contribute to the charge amplification process. Towards smaller and larger values of d this effect is limited until the steady state can not be achieved as well.

5.4 Simulated Energy Spectra

Besides their number, particles at the screen just outside the cavity are also recorded with their momentum vector at the moment of impact. Since the MEG test stand aims for longitudinal energy characterisation as well, all impact energies of the tracked macro particles are read out at the screen position. Thereby, it is observed that particles originating from the initial charge blow-up in the first nanoseconds acquire an overall higher kinetic energy compared to particles from steady state multipacting conditions (cf. Figure 5.13). This is mainly due to the higher electric gradient before reaching stability. Additionally, the energy spectra show a peak in the low-energy range from near zero to $\sim$60 eV. A correlation is seen to simulations involving higher bunch charges, but no detailed investigation is made to fully explain this feature. Potentially, higher order multipacting processes, involving particles that travel for more than half an RF cycle, are involved.

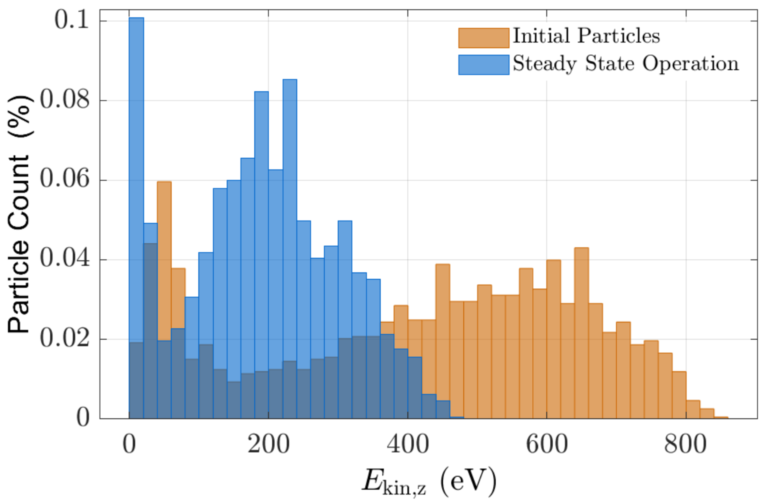

Figure 5.13: Histogram showing the percentage of beam particles within a specific longitudinal energy range. Colours distinguish between initial particles and those posterior to the onset of steady state multipacting. Results are from a simulation using default settings.

With help of Figure 5.11 it could be shown that a higher gun current is expected with increasing field gradient inside the cathode gap. Another interesting question revolves around the beam quality in regards to those different resonant multipacting situations. Most applications aim for high current and low energy spread. Therefore, Figure 5.14 is presented to show the recorded energy spectra in the steady state from simulations involving different combinations of d and E_0. When the acceleration voltage U_0 is high and therewith the total charge as well, particle energies are large compared to the low-gradient situation, which is the same for all gap sizes. A higher current also comes along with a wider energy spread due to larger deflecting space charge forces, together with the more crowded phase region inside the resonance condition. In general, the calculated energy spectra are rather broad in the respected regime, which is a consequence of the low particle velocities.

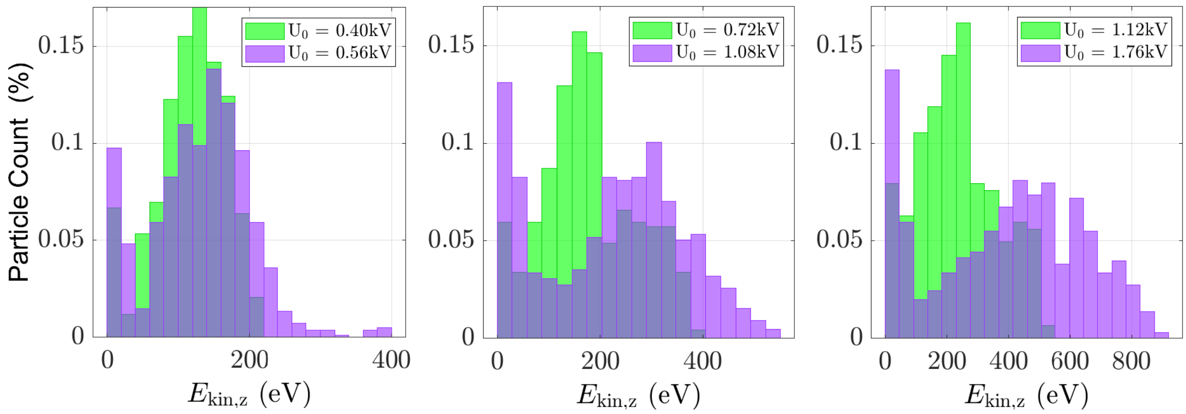

(a) $d = 0.80\,\mathrm{mm}$ (b) $d = 1.20\,\mathrm{mm}$ (c) $d = 1.60\,\mathrm{mm}$

Figure 5.14: Calculated longitudinal energy spectra with respect to two different initial acceleration voltages U_0 for three cathode gap sizes of 0.8 mm (a), 1.2 mm (b), and 1.6 mm (c).

Interim Conclusion

Even though some uncertain assumptions have been taken into account, the particle tracking results in this chapter draw a qualitatively consistent picture to the expected multi-particle motion in an MEG. Small cathode distances allow for the application of small initial field gradients, which lead to electron bunches of low charge and relatively small longitudinal energy spread. By increasing the accelerating gap voltage both, output current and energy deviation, are increased for all gap sizes similarly. A stable multipacting current might still be observed for distances much greater than the expected value of d, where equivalent impact energies within the resonance condition are usually tailored around a SEY of $\delta \simeq 1$. This coincides with the space charge dominated energy region, in which an electron bunch inside the cathode gap is blown up and also particles outside the resonant condition contribute to secondary generation in a significant amount.

6 Test Stand for Experimental MEG Performance Studies

After discussion of the primarily theoretical insight into work parameters and rough expectations on the current efficiency in the previous two chapters, the approach to feasible MEG operation in terms of constructional issues is described in the following. At the same time, it has to be mentioned that there is no straight forward procedure of one after the other, since all design phases are strongly connected, at least in the course of this work. However, the interplay of physical understanding and numerical simulations in regards to the cavity mode structure led to selected MEG designs as the main body of an experimental setup for practical MEG research.

6.1 MEG Cavity Designs

There are several objectives associated with the cavity design, that are needed to test the electron beam properties in dependence to a variety of physical tuning factors. The most important ones are:

- Propagation of the TM_{010} mode at $f_0 = 2.998\,\text{GHz}$ inside the RF cavity
- Adjustable cathode distance and therefore simultaneous frequency tuning
- Possible application of different power coupling conditions
- Minimisation of power losses other than external coupling and material resistivity
- Energy efficient maximum field gradient inside the cathode gap
- Increased chance of multipacting ignition at low field gradients
- A convenient way to change cathode materials and aperture dimensions
- Sustainability of less than 10^{-6} mbar internal pressure (high vacuum)

The calculation and construction of the cavity itself under consideration of the listed requirements turned out to be a non-trivial challenge. Since there was no blueprint available, the whole development process underwent frequent changes even until after the commissioning of the gun. As a consequence of many experimental difficulties, two different cavity designs were constructed and tested in the MEG setup. An early ”prototype” design is shown in the following, as well as the ”main” test cavity in representation of the fundamental design behind most of the successful measurements in Chapter 7.

Prototype Design

Bringing together the demand of a multipacting resonance condition, adjusted to the design criteria of a realistic RF cavity with proper wave propagation, requires the use of simulation tools. For the construction of an MEG involving the possibility of frequency tuning and variable measurement conditions *CST Microwave Studio*®[106] has been used specifically. Precise finite element method (FEM [107]) calculations are thereby able to solve the eigenmode spectrum for a given resonator geometry and material. They are strongly connected to the feasibility of constructing all parts individually and the experimental application, which is described in Section 6.3.

The early development process of an aluminium MEG cavity with adjustable cathode spacing led to the model illustrated in Figure 6.1a. Corresponding technical drawings are given in Figure A.2. Other approaches involving different overall cavity shapes, cathode geometries, or aperture dimensions are not described here. However, the general idea is about changing the cathode distance d by moving a linear translator (L1) towards an opposing aperture plate, while also maintaining the resonance frequency at 2.998 GHz. Attached to the tip of L1 is an exchangeable cathode plug, as presented in Figure 6.1b, including the designated emission surface of diameter $D_c = 2R_c$. Because of field leakage into the translator feed-through both, cathode plug and inner wall, are connected via clamped springs around the hole circumference. Power transmission into the cavity by pin-coupling leads to the formation of electromagnetic modes. The resulting electric field gradient inside the cathode gap volume from the TM_{010} mode is

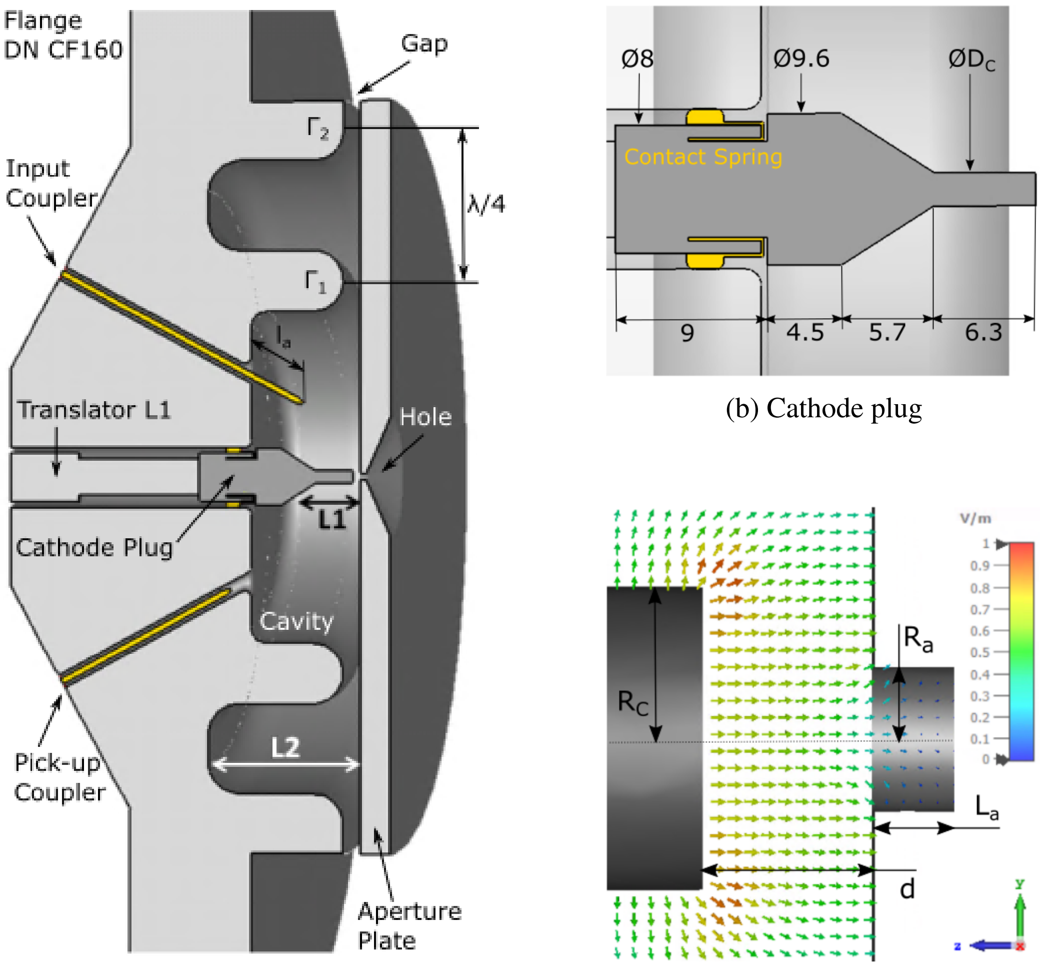

(a) Cavity model

(b) Cathode plug

(c) Electric gap field distribution

Figure 6.1: Prototype cavity design from CST with quarter-wave impedance transformer (a), dimensions of the cathode plug (b), and normalised field distribution in the accelerating gap projected onto the central plane (c).

displayed in Figure 6.1c. It can be seen that the maximum field strength is highly dependent on the shape of the cathode tip. Thereby, the oblique 5.7 mm middle part is introduced to weaken the effect of cavity detuning slightly, when the cathode plug is moved in and out.

Primarily, the detuning effect under change of d is compensated through shifting the whole cavity flange relative to the aperture plate with help of a second external translator (L2) and thereby changing the cavity width longitudinally. Via L1 the cathode can thus be moved relative to both, aperture and inner cavity, individually. Movement of L2 also effects the size of a gap, that is formed on an outer ring separating the cavity and the fixed aperture plate for gas evacuation. The edges are thereby supposed to be electrically terminated due to a quarter-wave impedance transformation. By the inclusion of two walls, a single-section waveguide line with length according to a quarter of the resonance wavelength and different characteristic impedance is formed between cavity and free space in radial direction. For termination of the incoming wave, a match is required, so the reflection coefficients Γ_i of both transformer steps must be equal [108]. Because of the rounded edges and the nature of hollow spaces, the transformer line impedance is imprecise, however, little radiation was registered outside of the slit.

According to the solution from eigenmode simulations presented in Figure 6.2a, very small field strengths are obtained in the outer cavity region with respect to the TM_{010} mode anyway. Maximum field gradients are rather seen in the cathode area, hence an efficient energy transfer for electron acceleration in the relevant gap can be expected. Simulations involving the pin-coupling mechanism as in Figure 6.2a, as well as the loop-coupling method with the second cavity model (cf. Figure 6.2b), show sufficient coupling strengths due to matched line impedances.

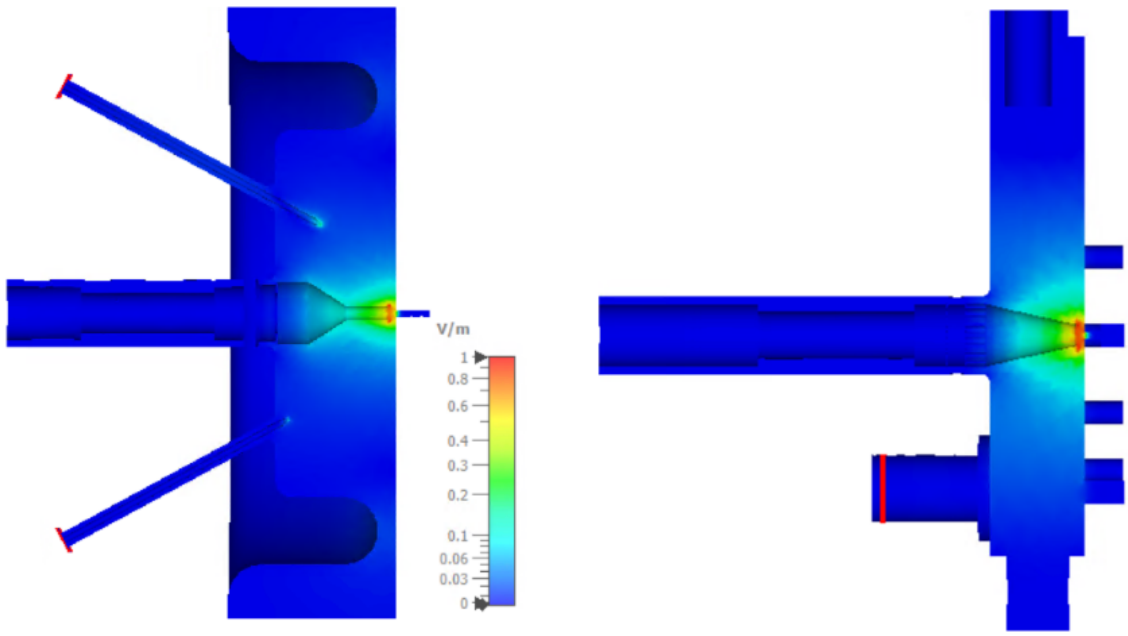

(a) MEG cavity prototype

(b) Main MEG test cavity

Figure 6.2: Cross-sectional electric field distribution of the TM_{010} mode at 2.998 GHz in the whole previous (a), and improved (b), MEG cavity design from CST calculations. In (a), the outer ring of the cavity is partially excluded. Illustrations are not of the same scale.

Main Test Cavity

After experimental investigation of the gun cavity prototype resulting in hardly reliable measurements, described in Section 7.1, it was decided to reinvent other fundamental designs. The modular requirements of our setup thereby led to a cavity scheme illustrated in Figure 6.3, where translator L1 is still used to adjust a cathode plug with respect to the opposing aperture. To tune the resulting frequency shift a rectangular plunger is moved in and out via the newly introduced second linear translator (L2). Since the beryllium copper springs have proven to accomplish sufficient electrical contact to the cavity, they are used for the plunger as well as for the cathode plug. As a result of the cavity being closed to all sides, additional holes had to be implemented for gas evacuation. Furthermore, a feed-through on the opposite side of the plunger is drilled as a guiding tunnel for possible UV light irradiation onto the cathode region, when the MEG is operated. Technical aspects are described in Section 6.3, Figure 6.9, where the focus moreover lies on constructional issues.

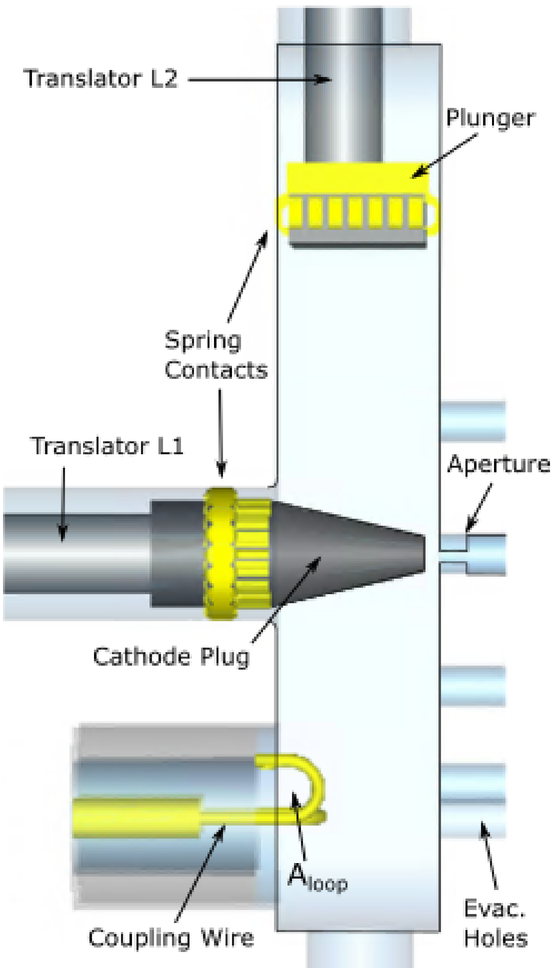

(a) Cavity model

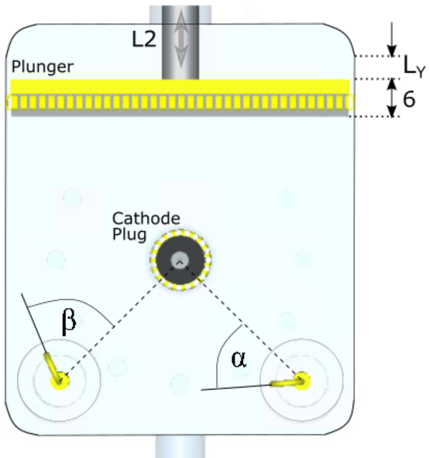

(b) Top view on couplers and plunger

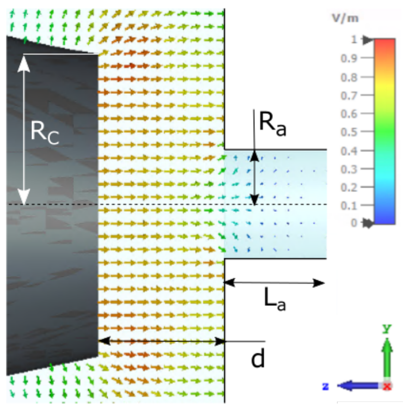

(c) Electric gap field distribution

Figure 6.3: Improved cavity design from CST with plunger tuning (a), the loop coupling method by variable angles α and β (b), and the normalised field distribution in the accelerating gap projected onto the central plane inside the cathode surfaces (c).

Coupling is provided by two loop wires, that are guided into the cavity through perpendicular holes with embedded N-connectors. Thereby, the coupling coefficient can be adjusted by rotation and size of the covered loop surface relative to the direction of the magnetic field lines. An angle $\alpha = 0$ of the input wire creates maximum coupling (cf. Figure 6.3b), the second loop is supposed to act as a pick-up port for probing of the transmitted cavity power. Both feed-through connectors are designed to be exchangeable in the experimental setup. A cross-sectional view on the simulated field distribution with coupling to the TM_{010} mode is shown in Figure 6.2b. It is demonstrated that maximum field densities are achieved inside the cathode gap and the field gradient overall decreases towards the lateral cavity walls.

6.2 Numerical Characterisation Studies using CST

For the rather complicated cavity geometries, simulations in regards to the cathode-aperture configuration are performed to evaluate the respective frequency tuning possibilities. That does not include influences of the surrounding cavity wall sizes, or cathode plug dimensions, even thought they have been regarded in defining the overall range of key characteristic parameters, mainly the resonance frequency. These global shapes were part of a fundamental design process, that was more result-oriented and less adequately documented. However, besides the frequency shift by changed gap size, or cathode radius, also the effect on power related cavity parameters is simulated and analysed. Since the coupling configuration plays an important role for the power transmission, simulations involving external coupling schemes are included as well. The following Table 6.1 lists main parameters involved in the illustrated characterisation studies, which focus on adjustable dimensions for both cavity designs.

Parameter		Default Value	
Cathode Distance	d	1.2 mm	Plug tip-to-aperture distance.
Aperture Radius	R_a	0.5 mm	Circle radius of the open aperture.
Aperture Length	L_a	2.0 mm	Lengths of the inner aperture part.
Cathode Radius	R_c	1.05 mm	Tip radius in previous cathode plug design.[a]
”	”	1.40 mm	Tip radius in main cathode plug design.[b]
Cavity Gap[a]	d_{gap}	2.8 mm	Evac. gap size between flange and plate.
Plunger length[b]	L_Y	2.0 mm	Distance from minimum plunger position.
Antenna Length[a]	l_a	8.0 mm	Length of input coupler pin inside cavity.
Probe Length[a]	l_r	3.7 mm	Length of pick-up coupler pin inside cavity.
Coupling Angle[b]	α	45°	Coupler loop angle relative to $\mathbf{H}_{cav}$.
Probe Angle[b]	β	70°	Pick-up loop angle relative to $\mathbf{H}_{cav}$.
Loop Surface[b]	A_{loop}	8.4 mm^2	Total enclosed loop surface inside cavity.

Table 6.1: List of adjustable setup parameters for the CST characterisation studies involving the cathode-aperture configuration (top), as well as tuning lengths (middle) and coupling mechanisms (bottom), which are different for the two designs[a,b]. They can be compared to Figures 6.1[a] and 6.3[b] respectively.

6.2.1 Influence of the Cathode Geometry on the Resonance Frequency

Geometrical sizes are changed separately in order to calculate their influence on the resonance frequency. In doing so, the other adjustable parameters are set to their default value according to Table 6.1, when they can be applied to the respective cavity model.

With the results from Figure 6.4, regarding the prototype design, it is found that changes to the aperture dimensions lead to a relatively small frequency shift in comparison to the size and spacial distance of the cathode tip surface. It concludes that the field inside of the aperture decreases strongly as a function of the length L_a, which is moreover expected with respect to Eq. (3.13). The cathode surface has a greater influence on the TM_{010} frequency, since it affects the mode at a position of peak field gradients. Adjustments to the evacuation gap d_gap up to sizes of 4 mm are able to compensate for the detuning by variable cathode distances in a range of ~0.6 mm within this cavity model. The resonance frequency f_0 is tuned to 2.998 GHz.

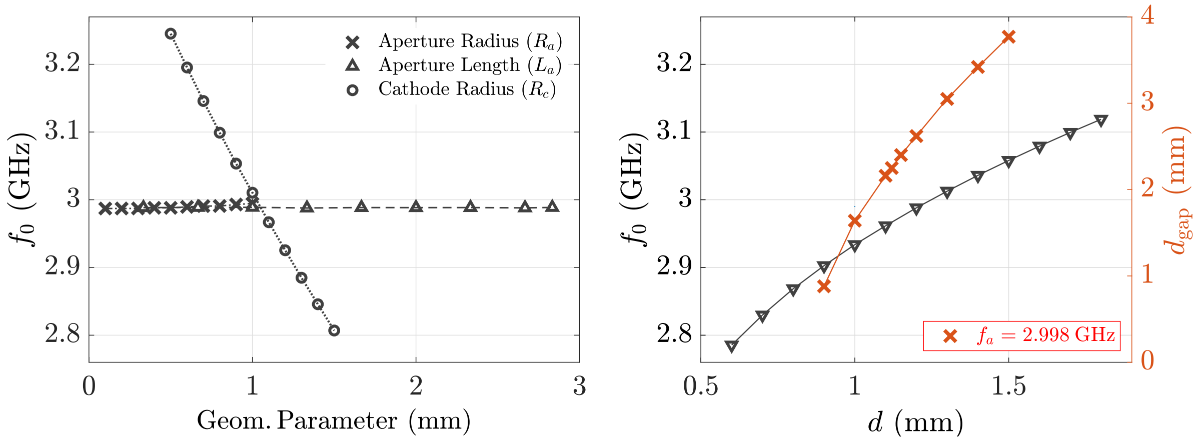

Figure 6.4: Simulated resonance frequency f_0 in dependence of variable parameters regarding cathode and aperture sizes for the prototype design (left), and the specific frequency shift by changing the cathode distance d (right), together with the corresponding tuning length d_gap preserving $f_0 = 2.998$ GHz (red). All lines are guides to the eye.

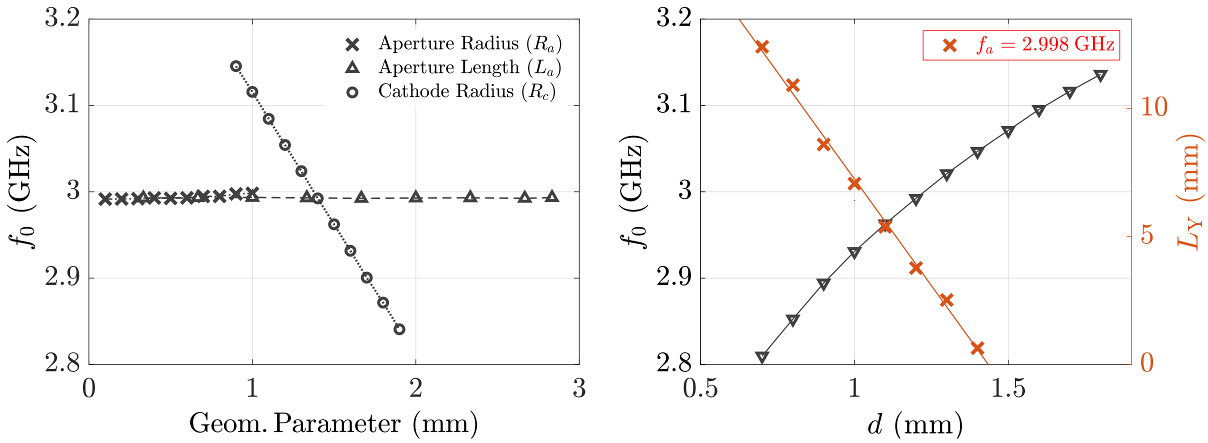

Figure 6.5: Simulated resonance frequency f_0 for variable cathode and aperture dimensions in the main test cavity (left), and the specific frequency shift as a function of the gap size d (right), alongside the corresponding tuning length L_Y preserving $f_0 = 2.998$ GHz (red).

An illustration of the parameter studies performed with the main cavity design is given in Figure 6.5. Evaluation of the simulation data shows very similar features as for the previous sets of calculations. Besides the overall different wall and cathode geometry, the highlighted feature is a larger tip surface area and therefore stronger detuning by altered cathode distance. For tuning of f_0 to the desired 2.998 GHz, the plunger is shifted further outside the cavity towards a minimally possible reference position $L_\mathrm{Y} = 0$ with increasing d. The distance thereby appears as a linear function

$$L_\mathrm{Y}(d) = [-16.67 \pm 0.06]\ \frac{L_\mathrm{Y}(\mathrm{mm})}{d(\mathrm{mm})}, \tag{6.1}$$

in which frequency detuning inside a range of $\sim$0.7 mm could effectively be compensated.

6.2.2 Calculation of Power Related Cavity Parameters

Material dependent power losses regarding the aforementioned eigenmode solutions are considered in post-processing steps. For the calculation of power dissipation, including dielectric losses P_D as well as wall losses P_W, the average total loss power yields

$$\begin{aligned} P_\mathrm{loss} &= P_\mathrm{D} + P_\mathrm{W} \\ &= \pi f \tan(\phi)\, \varepsilon_0 \varepsilon_\mathrm{r} \int_V |\mathbf{E}|^2\, \partial V + \frac{1}{2}\sqrt{\frac{\pi \mu f}{\sigma}} \int_S |\mathbf{H}_\mathrm{t}|^2\, \partial S \end{aligned} \tag{6.2}$$

at a specific frequency f [106]. Thereby, ϕ is the loss angle, $\mathbf{E}$ is the field distribution in the corresponding shape volume V, together with the dielectric constants ε_0 and ε_r, σ is the specified conductivity, μ the permeability value, and $\mathbf{H}$ is the magnetic field of a loss-free calculation, tangential to the surface S, similar to Eq. (3.32).

Key parameters with respect to the cavity geometry can therefore be calculated for an estimation of the electromagnetic cavity properties. Results from CST simulations for the presented designs with a TM_{010} eigenmode frequency of $f_0 = 2.998$ GHz are shown in Figure 6.6 for different tunable gap sizes d from the previous section. Without consideration of external losses due to coupling, the unloaded quality factor Q_0 is determined by Eq. (3.28) as a result of the internal loss calculation. The total energy, equal to the sum of electric and magnetic energy as in Eq. (3.30), is thereby normalised to 1 Joule for the entire amount of energy stored in the simulated structure. Furthermore, the shunt impedance R_s can be calculated from dividing the voltage square along z-direction by perturbation losses as introduced with Eq. (3.33).

For the simulations including both, the prototype (Figure 6.6a) and the main MEG design (Figure 6.6b), lossy aluminium is used as the material modelling all inner wall surfaces. The cavity volume thereby consists of perfect vacuum ($\varepsilon_\mathrm{r} = \mu_\mathrm{r} = 1$). Since no other loss mechanisms such as radiation or discharge are considered, and also no imperfections from material defects, surface roughness, oxide layers and water adsorption, or suboptimal spring contacts are included for the calculations, total power losses P_loss are rather small in both instances. Therefore, the consequently small surface resistivity is further expressed by a high Q_0 in general, as

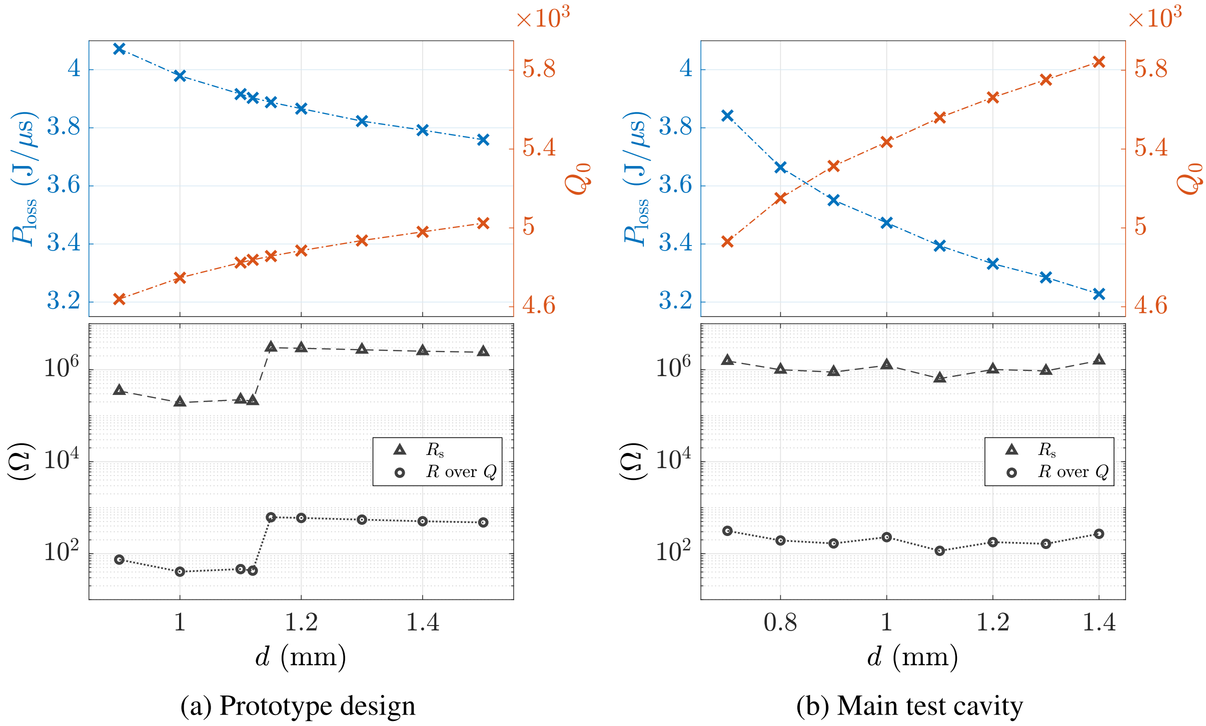

Figure 6.6: Comparison of results from CST power loss simulations involving the early (a), and the improved cavity design (b). The total loss P_{loss} and the unloaded quality factor Q_0 (top), as well as the respective shunt impedance R_s and R/Q_0 ratio (bottom), are thereby calculated with respect to the cathode distance d, which is tuned to $f_0 = 2.998\,\mathrm{GHz}$ in accordance with Figures 6.4 and 6.5. Other geometrical parameters are set to their default values (cf. Table 6.1).

well as large shunt impedances in the order of MΩ. However, the comparability of one simulation relative to the others should be ensured and an overall increase of Q_0 with d can be noticed. Involvement of the quality factor induces less variance, than the determined R_s-value, for the R over Q calculation regarding the cavity geometry. Given uncertainties from run to run seem to not only be dependent on $P_{\mathrm{loss}}(d)$ and might also be connected to systematic errors from the calculation of peak field gradients in the cathode tip region, that suffer from imprecisions due to the formation of numerical grid cells at small geometric features. As a result, the slightly inconsistent and widely inhomogeneous gap field distribution would affect the voltage calculation and therefore also the shunt impedance.

Where the R_s value in Figure 6.6b remains constant to some degree, a jump in the order of one magnitude is seen with the prototype cavity design between $d = 1.12$ and $1.15\,\mathrm{mm}$. Hence, it can be expected that the quarter-wave impedance transformer is not well matched for tuning gap sizes d_{gap} under approximately $2.4\,\mathrm{mm}$ and radiation losses outside of the cavity could occur in a more noticeable way.

6.2.3 External Coupling and S-Parameters

CST uses broadband frequency sweep techniques to derive the spectrum of field solutions in the frequency domain by transformation of Maxwell's equations, when a time-harmonic dependence of the fields and their excitation is assumed [106]. For studying the frequency dependence of the TM_{010} excitation in our MEG designs, a time-harmonic signal of 1 W intensity is transmitted through discrete waveguide ports at the two coupling pins and loops, respectively. The goal is to derive scattering parameter matrices (S-parameters), which are normalised to a source impedance of $Z_0 = 50\,\Omega$, and thereby test several situations with respect to the coupling factor κ for each port numerically.

S-parameters are used as a conceptual approach and practical way to describe RF circuits in terms of waves. A comprehensive description involving the implications in an n-port system can be found in [109] for example, whereby the MEG would be considered a 2-port system. The relation between an incoming power wave $a_i = (U_i + I_i Z_0)/2\sqrt{Z_0}$ and a wave $b_i = (U_i + I_i Z_0)/2\sqrt{Z_0}$, that is travelling away from port i, can be written as a system two ($i = 1,...,n$) linear equations [109]:

$$\begin{pmatrix} b_1 \\ b_2 \end{pmatrix} = \begin{pmatrix} S_{11} & S_{12} \\ S_{21} & S_{22} \end{pmatrix} \begin{pmatrix} a_1 \\ a_2 \end{pmatrix} = \mathbf{S} \cdot \mathbf{a}\,, \tag{6.3}$$

whereby $\mathbf{S}$ is the S-matrix. If no excitation is applied to both ports at the same time and they are also terminated by a matched load, S_{11} of a single impedance Z_L connected to Z_0 is equal to the input reflection coefficient

$$S_{11} = \frac{b_1}{a_1}\,|_{a_2=0} = \frac{U_1 - I_1 Z_0}{U_1 + I_1 Z_0} = \frac{Z_\mathrm{L} - Z_0}{Z_\mathrm{L} + Z_0} = \rho = \frac{(Z_\mathrm{L}/Z_0) - 1}{(Z_\mathrm{L}/Z_0) + 1} \tag{6.4}$$

from Eq. 3.39. In a similar fashion, S_{12} is the forward transmission from port 1 to port 2, S_{21} vice versa, and S_{22} is the output reflection coefficient at port 2, which is symmetric to the element S_{11} [109]. A coupling coefficient at resonance can thus be determined by S-parameters analysis.

The methodic aspects of power coupling into a resonating structure are already briefly introduced with help of Figure 3.6. For the two MEG designs here, different mechanisms are used in particular:

a) *Pin Coupling*: In the prototype cavity design (cf. Figure 6.1), pins serve as the inner conductors of a coaxial antenna at port 1 and a receiver at port 2. They are inserted into the cavity volume by the distance l_a and l_r, respectively, and the electric surface current is coupled with the electric field of the cavity mode.

b) *Loop Coupling*: In the second "main" design (cf. Figure 6.3), loops at both ports are able to couple with the TM mode by generation of a magnetic dipole $\mathbf{M}_\mathrm{loop}$, whose intensity is proportional to the enveloping loop area A_loop and the input power P_cav. The amplitude of the excited mode is, in turn, proportional to the scalar product between $\mathbf{M}_\mathrm{loop}$ and the magnetic field $\mathbf{H}_\mathrm{cav}$ in the loop region [76]. It can therefore as well be adjusted by the loop orientation.

To test the range of possible coupling strengths in a forthcoming setup, κ is determined with respect to the adjustable settings of l_a, α and A_loop. Thereby, κ_{22} is dedicated to the pick-up port of power probing and l_r, as well as β, remain unchanged throughout the calculations under far subcritical coupling conditions. Results including the prototype design in Figure 6.7, and the main cavity in Figure 6.8, are based on S_{11} and S_{22} parameter evaluation, whose underlying data sets can be found in Figures A.7, A.8 and A.9. The simulation series under alteration of the respective coupling parameter show a significant influence on the coupling constant for all cathode gap sizes d in both designs. Whereas the first one for the prototype design indicates an almost exponential increase with l_a, the second one suggests an angular-harmonic shape due to the loop surfaces component $A_t \simeq A_{loop} \cdot \cos(\alpha)$ tangential to $\mathbf{H}_{cav}$. From subcritical

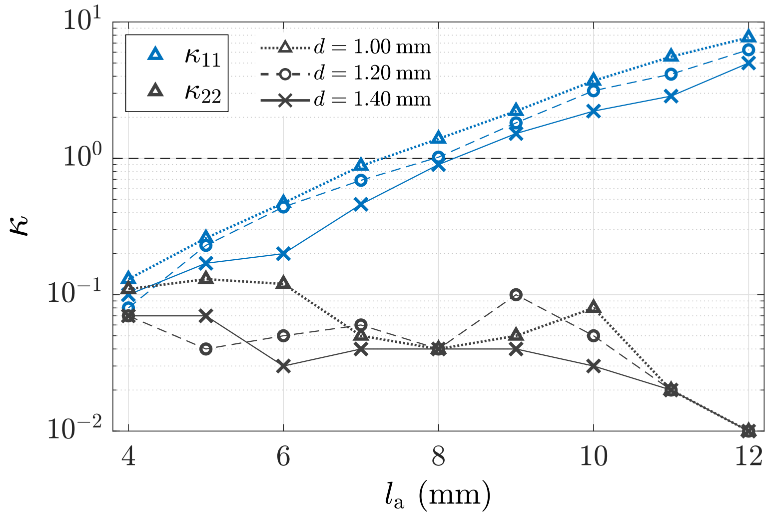

Figure 6.7: Coupling constant κ extracted from S-parameter simulations with respect to the antenna pin length l_a at port 1, for three distinct gap sizes d tuned around 3 GHz, in the prototype design. Thereby, blue indicates power reflection at port 1, whereas the black data represents coupling at port 2 with a constant receiver pin length $l_r = 3.7$ mm. A horizontal dashed line at $\kappa = 1$ marks the point of critical coupling, respectively.

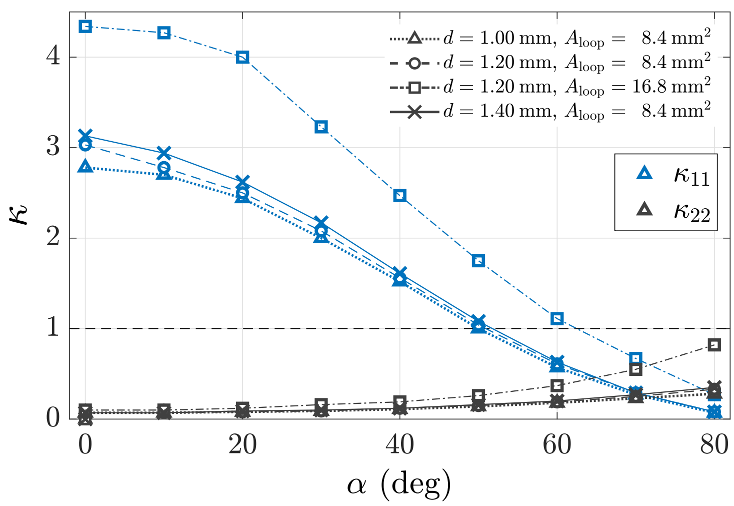

Figure 6.8: Coupling constant κ extracted from S-parameter simulations with respect to the loop angle α at port 1, for three distinct gap sizes d and two enclosed loop surfaces A_{loop}, in the main cavity design. Blue thereby illustrates κ obtained from S_{11} at the coupling port 1, and black gives the corresponding κ from reflection at port 2 (S_{22}) under fixed angle $\beta = 70°$.

to supercritical coupling conditions, proper settings can be achieved for power transmission regarding the filling of both cavities. In the case of extreme situations at port 1 ($l_a > 1$ cm, or $\alpha > 60°$), the corresponding parameter at port 2 must eventually be adjusted within the experimental procedure, since S_{22} would otherwise not be suitable for a probe signal, in that specific configuration, because of its high transmission ratio.

Interim Conclusion

In the framework of CST, both presented designs are working in terms of adjustable cathode distance, their frequency shift compensation, and power transmission including different coupling mechanisms. It needs to be emphasised that they were not modelled and constructed at the same time and because of severe experimental limitations with the prototype design (cf. Section 7.1), the posterior cavity is supposed to have many advantages over it. Among them are the prevention of a not well understood $\lambda/4$ transformer, an easier way to change the coupling strength, a wider tuning range with respect to d, larger emission surfaces overall and most importantly the possibility to shine UV light onto the cathode area through an external window. Also it is demonstrated that sufficiently high quality factors can be achieved to store field energy for electron acceleration, even though the results are based on perfect material properties and interfaces as they are hardly approachable in reality.

6.3 Experimental Setup

This section is about the structure and development of the experimental test setup of our multipacting guns, as well as the general measurement procedure. Thereby, crucial components in the assembly, as they are illustrated in Figure 6.9, are discussed. The main focus lies on the MEG cavity based on the improved "main" design (8), since it could be used to obtain more meaningful experimental results (cf. Sections 7.2 and 7.3). Detailed drawings regarding the cavity dimensions are illustrated in the appendix, Figure A.4. Due to the modular connection between the upper cavity flange (grey) and the opposing aperture plate (orange) via vacuum sealing, an electrical RF contact is accomplished by a small 200 x 200 μm edge on top of the plate directly, which can be seen in Figure A.5 in detail.

Inside of the MEG cavity, linear translators (1,3) are used to adjust the cathode and plunger positions, with a precision of 50 μm, respectively. The whole cavity assembly is placed on top of a bulk translator (2), that has been necessary to modify the tuning gap distance of the "prototype" gun cavity. Generally, it is also part of the vacuum section and its interior is evacuated by the turbo pump stand (7). To determine important electromagnetic cavity parameters, a vectorial network analyser (5) measures S-parameters magnitudes. Measurements in regards to the multipacting gun current are performed by a fast oscilloscope (10), which is supposed to detect an induced Faraday Cup voltage guided through the SMA connector at (4). A gate potential can be applied in front of the cup by a common DC power supply (11). In addition to two RF amplifiers (15,16), the power system in operation of the MEG mainly consists of two

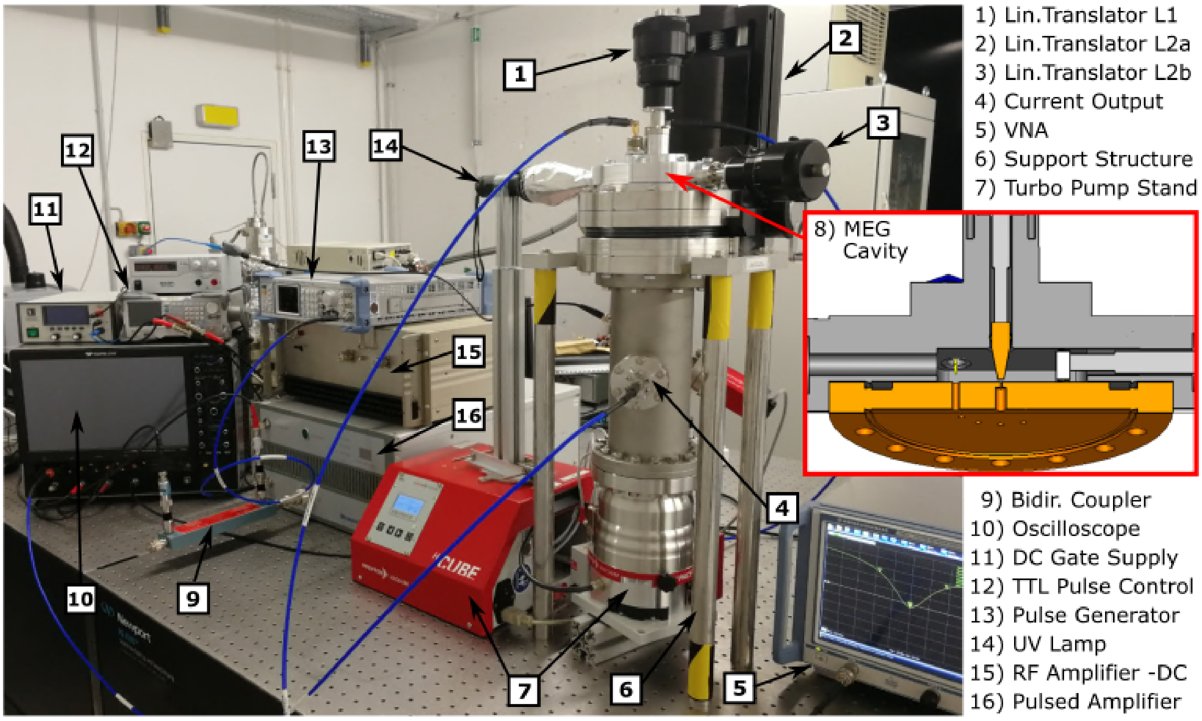

Figure 6.9: Picture of the experimental setup as a whole.

function generators (12,13), which are providing the RF signal and pulse information. Generator power is therewith transmitted through a bidirectional coupler (9) towards the cavity input port. Finally, the addition of a commercial UV lamp (14), or laser pulses potentially, enables irradiation of the cathode area from the window side, whereby the window itself consists of fused silica (SiO_2). In the course of the construction and commissioning of the gun setup, most cavity parts as well as the supporting structure (6) and the Faraday Cup were manufactured by the mechanical workshop of the Universität Hamburg at DESY site.

6.3.1 Procedure and Adjustable Parameter Space

The experimental procedure is generally divided into four stages, which are discussed in the following sections. In short, after installation of the entire setup, presented in Figure 6.9, adjustments to the cathode distance with respect to the corresponding tuning length under consideration of the external coupling situation are made. This is monitored by simultaneous VNA analysis. Secondly, the multipcating condition including a detectable amount of output current is searched and measurements with a variety of electromechanical parameter studies can be performed. Therefore, the inside pressure is pumped down to values of 10^{-6} to 5×10^{-8} mbar. After given measurement series, cavity related quantities such as the loaded quality factor, or the coupling constant, are taken in a third step. The fourth stage is rather optional and is about the overall measurement performance and its improvement by constructional modifications to the setup components in general.

Frequency Tuning Analogue to the numerical approach in Section 6.2.1, the frequency tuning is tested at resonance with respect to the cathode distance involving both cavities. Results regarding the cavity prototype assembly are shown in Figure 6.10. It is observed that moving the bulk translator (L2a) over a span of $\sim$1.5 mm compensates for the frequency shift from a changed cathode gap size of around 0.3 mm. The functional dependency is thereby congruent with the simulation from Figure 6.4 to some extent, but systematic errors play an important role for a precise assessment here. Especially distances in translator direction are error-prone, since they are slightly changed with every dismantling of the cavity flange.

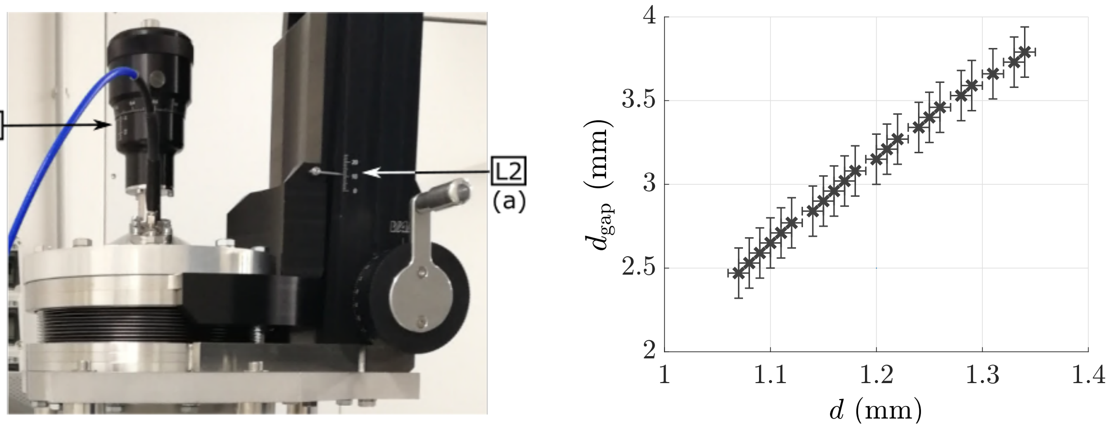

Figure 6.10: Picture of the cavity prototype assembly (left) and the measured frequency detuning compensation (right), where the tuning length d_{gap} is plotted versus the cathode distance d at $f_0 = 2.998\,\mathrm{GHz}$, accordingly.

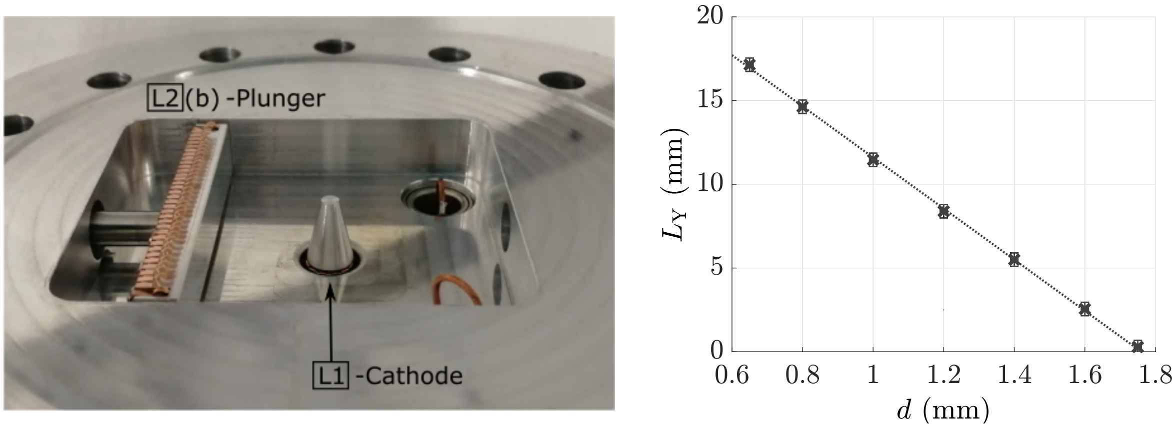

Figure 6.11: Picture of the main test cavity (left) and the measured frequency detuning compensation (right), where the tuning length L_{Y} is plotted as a function of the cathode distance d at $f_0 = 2.998\,\mathrm{GHz}$. The dotted line is a linear fit to the data.

The same is true for the other cavity assembly, whose tuning measurements are presented in Figure 6.11, together with a picture of the inner cavity. Under a fixed resonance frequency of $f_0 = 2.998\,\mathrm{GHz}$, the tuning length L_{Y}, which is connected to translator L2b, is registered with changing cathode distance. The resulting slope of the curve thereby yields

$$L_{\mathrm{Y}}(d) = [-15.22 \pm 0.15]\ \frac{L_{\mathrm{Y}}(\mathrm{mm})}{d(\mathrm{mm})} \tag{6.5}$$

from a linear fit. It turns out to be comparable to the calculated tuning function (6.1) derived from Figure 6.5 and demonstrates sufficient detuning compensation for parameter studies with respect to d. Another systematic inconsistency, however, concerns abrasion of the contact springs and inner surfaces due to frequent movement of the translators, which might generally influence the fundamental cavity properties at some point.

Generator Power System To power the MEG and therewith provide necessary acceleration criteria in terms of the multipacting resonance condition, a system consisting of RF signal generation and amplification (cf. Figure 6.9) is used. In our setup, the possibility of up to 10 W continuous-wave (CW) power supply was later added to the already existing 5 kW pulsed amplifier model AM96/3S-57-67R from *microwave amps* [110], which operates at a frequency of 2.998 GHz $\pm$ 5 MHz and a maximum pulse width of 10 μs at up to 100 Hz repetition rate. Whereas the CW amplifier is simply driven by a continuous RF source provided through the SMB-100A signal generator from *Rohde & Schwarz*, the pulsed one needs an additional TTL (transistor-transistor logic) pulse control signal in synchronisation with the external RF pulse. Timing of the latter is schematically shown in Figure 6.12. A square wave pulse generator is thereby used to both, trigger an RF pulse from the source, and also give the TTL control signal to the amplifier. At any point after the required delay due to the rise time of the amplifier, an RF output can be triggered inside the TTL command window and becomes intensified as long as the amplification is enabled. The enhanced wave pattern of controllable amplitude P_g is then sent towards the MEG input port, where it excites the fundamental cavity mode.

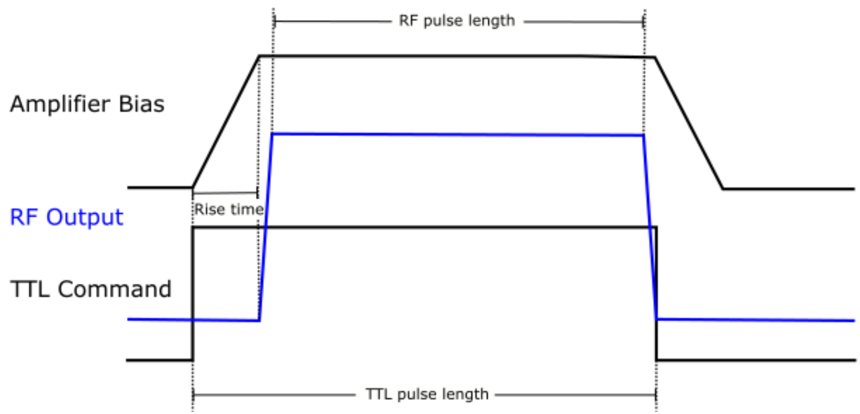

Figure 6.12: Timing of an RF pulse (blue) with the application of a TTL command, biased to the amplification period, according to the manual of [110].

Input Power Coupler At the aforementioned input ports, coupling is provided as it is proposed in Section 6.1 by realisation of the pin and loop coupler method for the respective designs. Figure 6.13a shows, how the pin is implemented into the previously manufactured cavity. Customised antennas are guided into the cavity under consideration of a 50 Ω line impedance for the coaxial path. They are connected to an integrated SMA feed-through and sealed with CF 16 flanges on the outside. Since no method to easily alter the coupling lengths was developed in

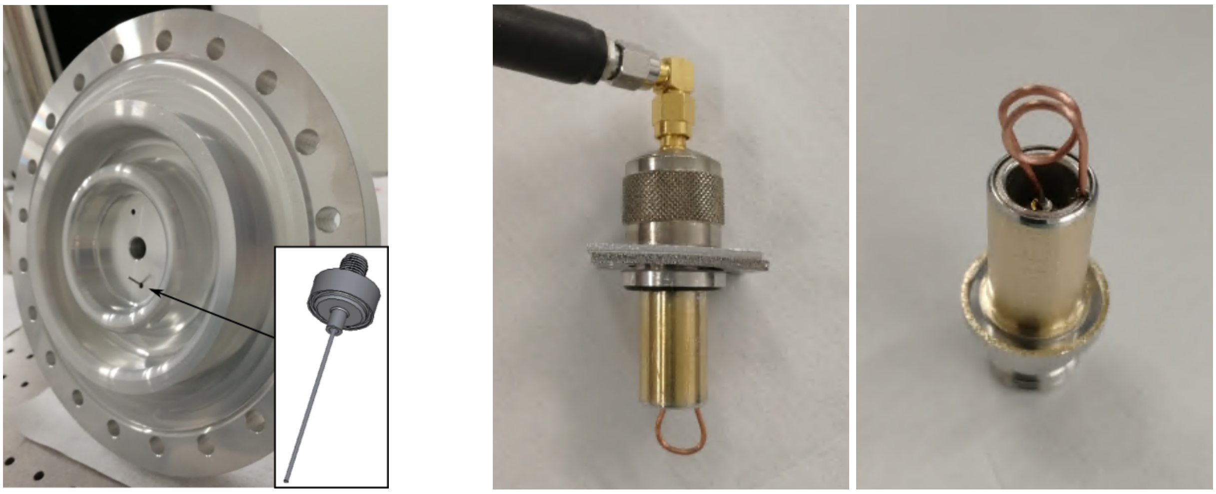

(a) Cavity with inserted pin (b) Connector with loop (c) Double-loop config.

Figure 6.13: Pictures of the coupling mechanisms regarding the MEG cavity prototype (a) and connectors as inserts into the sockets of the main cavity structure including different types of loop wiring (right), whereby a single-loop (b) is installed most of the time.

this case, it was decided to couple sub-critically and use metallic attachments for increasing the pin length, thus obtaining larger coupling constants in regards to the transmitted power. Despite its functionality, this method is not well suited because of uncertain changes in the cavity quality and loose connections, that sometimes lead to fluctuations with the power transmission on a short time scale.

An improved coupling method is therefore developed for the main test cavity, as pictured in Figure 6.13b for instance. Commercial N-connectors are milled off to fit into the corresponding sockets in the main cavity structure. Even though vacuum sealing is provided by rubber O-rings, inside pressures of $< 10^{-7}$ mbar can be achieved within a couple of hours. Rectangular clamps are used to fix the connector, whereby the radial-symmetric fit of the feed-through allows for 360° rotation inside the hollow deepening. In the single-loop configuration, longer wires and therewith larger loop surfaces A_{loop} than calculated had to be installed for proper coupling, which might be due to suboptimal soldering joints. However, sufficient coupling conditions could be achieved, as it is presented in the experimental Sections 7.2 and 7.3. The modular coupler design also gives rise to measurements with unusual wire configurations (cf. Figure 6.13c), which would eventually enable faster coupling and could also be tested out of curiosity.

6.3.2 VNA Characterisation

There are many measurable parameters determining key properties and performance indicators of waveguides and cavities. The most important values in regards to RF power transmission into our MEG are the coupling constants κ at both ports, the loaded quality factor Q_{L}, and also the resonance frequency f_0, which can all be obtained by a vectorial network analyser (VNA).

For control of the coupling strength, and therewith information about the power that is transferred to the oscillator, a Smith chart [111] is used to determine κ with each current measure-

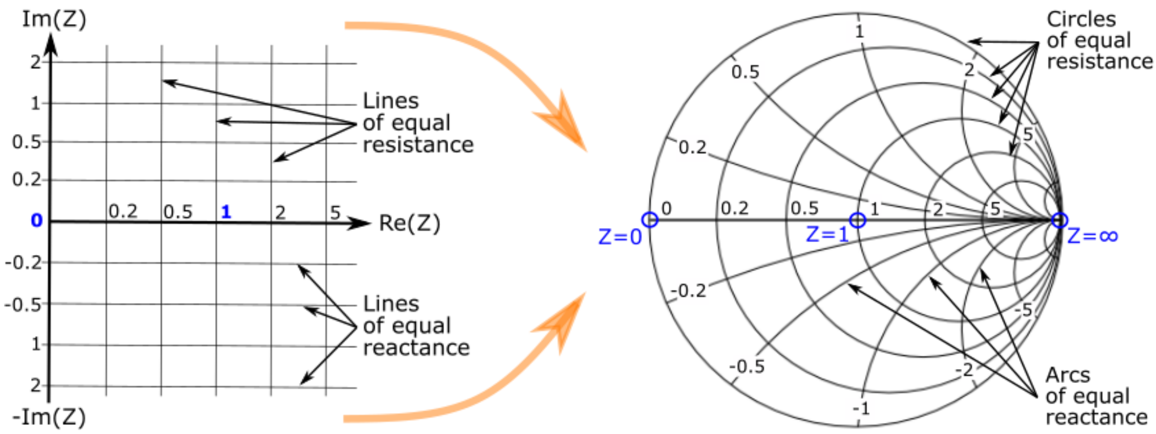

Figure 6.14: Projection of the complex impedance plane Z (left) onto the complex reflection plane, called Smith chart (right), by a bilinear Moebius transformation.

ment series. It provides a valuable representation of the complex reflection coefficient, given by Eq. (6.4), hence indicate the impedance match of a device under test [112]. A graphical illustration is therefore given in Figure 6.14, that shows its construction from the complex impedance plan ($Z = R + jX$) by reshaping, so that the area with positive resistance is mapped into a unit circle. An in-depth discussion on the properties and navigation on the diagram can be found in [112] for example. The basic properties, however, follow from the transformation, where the horizontal axis (ReZ) corresponds to zero reactance and the centre represents zero reflection ($Z/Z_0 = 1$). At the left and right intersection points, impedances are zero (short) and infinite (open), whereby the outer circle corresponds to zero resistance with $Z = jX$.

The power transmission in terms of coupling into the gun is effectively determined from the complex reflection coefficient $\rho = S_{11}$, as illustrated in Figure 6.15. In the course of the experiments it is found that reliable data could be obtained after MEG current measurements, rather

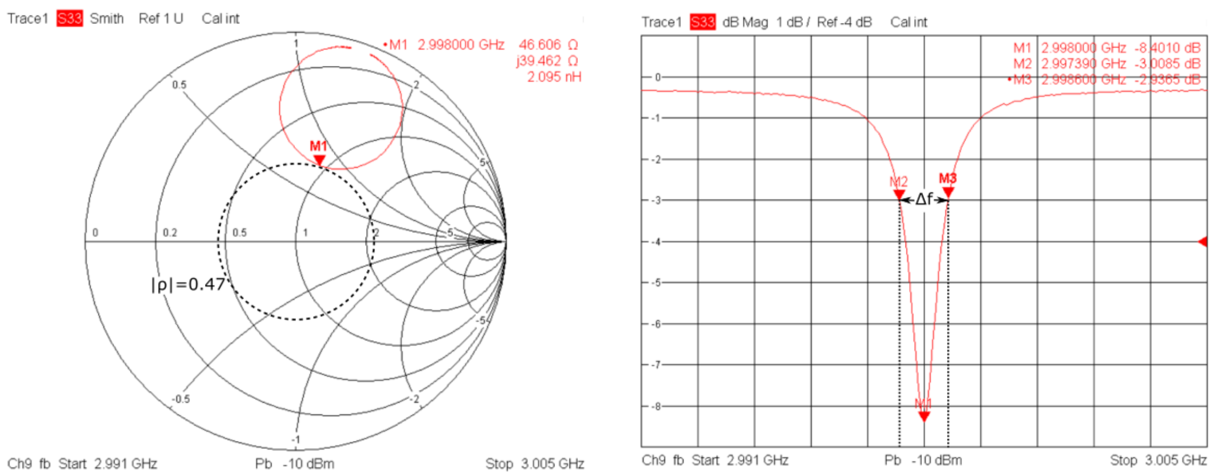

(a) Smith chart

(b) S_{11} Magnitude

Figure 6.15: Explanatory VNA measurement of the reflected S_{11} signal from the MEG cavity in a complex impedance view (a) and as a representation of the magnitude in dependence of the frequency stimulus (b).

than before. The RF field possibly stabilises metallic contacts with the springs, that become slack after translator movement, or dismantling of the cavity assembly. Figure 6.15a shows the example of a typical reflection measurement in the Smith diagram with the resonance circle in red. Since its extent does not exceed the point of zero reflection, the device is considered sub-critically coupled to the source impedance in this case. From the intercept with an $|\rho|$-circle, where points of constant reflection factors are displayed, the coupling coefficient κ can be read off. In case of supercritical coupling, $\kappa \widehat{=} 1/|\rho|$ is used accordingly. The loaded quality factor is then obtained from the scalar quantity of S_{11} (cf. Figure 6.15b) following

$$Q_\mathrm{L} = \frac{f_0}{\Delta f}, \tag{6.6}$$

where Δf is the full width at half maximum and f_0 is once more the resonance frequency. Because of external losses, the magnitude of half maximum power transmission is found at

$$|\rho(\Delta f)| = \frac{\sqrt{\kappa^2+1}}{\kappa+1}, \tag{6.7}$$

as a consequence of Eqs. (3.36) and (3.41), respectively.

The raw S_{11} data from VNA characterisation was generally not saved within the measurement procedure and is therefore not presented alongside corresponding MEG performance studies in Chapter 7. Resulting tables categorise key quantities in regards to the respective cavity parameters for each measurement series instead.

6.3.3 Data Acquisition

The measurement system, schematically illustrated in Figure 6.16 by means of a basic circuit diagram, is the integral part of data acquisition concerning the experimental MEG performance studies. It mainly consists of hardware components, that are used to detect the output gun current I_out from charge collection on a Faraday Cup and simultaneously measure the time-dependent power consumption of the gun cavity. The central piece is a four-channel digital

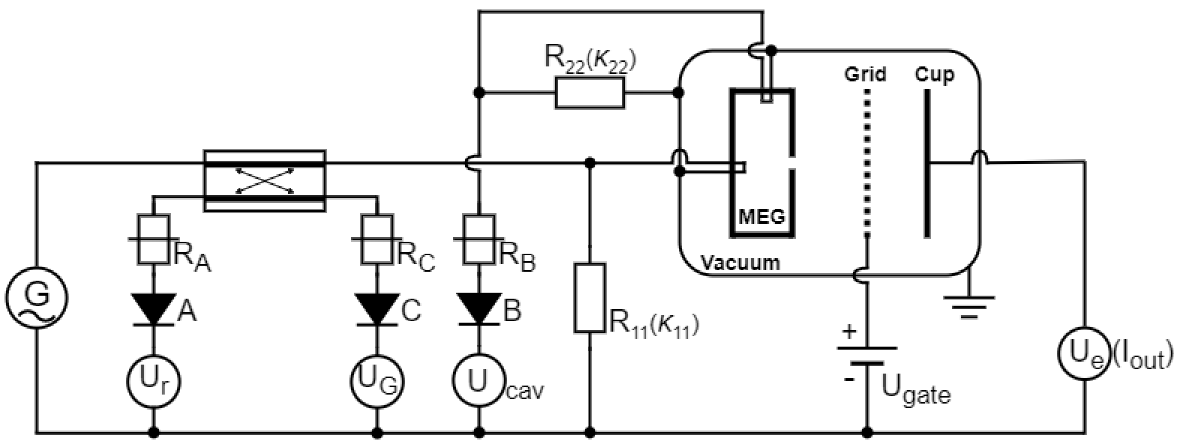

Figure 6.16: Schematic overview of the MEG measurement system.

oscilloscope not only recording the waveform signal of the collected multipacting current U_e, but also the rectified RF power signals from the generator U_g, reflection at the input port U_r, and transmitted power detected inside the cavity U_cav.

Power Probing Generator power from the RF amplifier first passes a bidirectional coupler through the transmitted port before it is coupled into the MEG cavity. Impedance mismatch is thereby indicated by the resistor R_{11}, which represents the generator impedance in analogy to Figure 3.5. A part of the total power (-20 dB) is also diverted to the coupled port of the directional coupler, where it is then further attenuated at R_C and rectified by the Schottky diode detector C. The resulting DC voltage U_G is recorded with the scope, and on the same trigger as the reflected power signal U_r from detector A, respectively. Power detected inside the cavity is measured in an analogous manner through detector B, but the signal is directly transferred from port 2 and has an additional impedance mismatch, indicated by R_{22}, due to coupling with κ_{22} or rather κ_out. For the calculation of an instantaneous cavity power P_cav, the wave amplitude must consequently be determined by the limit of Eq. (3.45), where now the forward power comes from inside the cavity.

Schottky diode detectors, as they are used for RF power detection at positions A, B and C, are typically operated in their square-law region, where the respective output voltage is proportional to the input RF power. Since exact dependencies deviate from the data sheet, the voltage response of all three utilised detectors is examined with an RF test signal of known amplitude. The results of these calibrations are shown in Figure 6.17, whereby the test signal power P is presented on the y-axis. Determination of the resulting power-voltage relations are found to be following a general fit model:

$$P(U_\mathrm{det}) = u_0 + u_1 \cdot \ln(U_\mathrm{det}) + u_2 \cdot U_\mathrm{det} + u_3 \cdot U_\mathrm{det}^2 + u_4 \cdot U_\mathrm{det}^3 \,. \tag{6.8}$$

It is used to determine the corresponding power value from voltage measurements with the detectors, hence probing the power indicators of the forward (P_g), reflected (P_r) and transmitted wave (P_cav) within the execution of an MEG current measurement. The fit coefficients u_i from Eq. (6.8), associated with the voltage response U_det of the three detectors, are listed in Table 6.2 for this purpose.

Det.	u_0	u_1	u_2	u_3	u_4
A	14.99	3.923	104.9	-630.2	1642
	(14.71, 15.28)	(3.881, 3.965)	(97.66, 112.1)	(-721.1, -539.2)	(1299, 1985)
B	15.73	4.131	93.33	-538.3	1383
	(15.53, 15.94)	(4.100, 4.161)	(88.34, 98.32)	(-598.9, -477.6)	(1160, 1606)
C	16.91	4.111	100.6	-576.9	1407
	(16.58, 17.25)	(4.062, 4.160)	(90.74, 110.4)	(-722.5, -431.4)	(763.4, 2051)

Table 6.2: Fit coefficients from the diode detector calibration (with 95% confidence bounds).

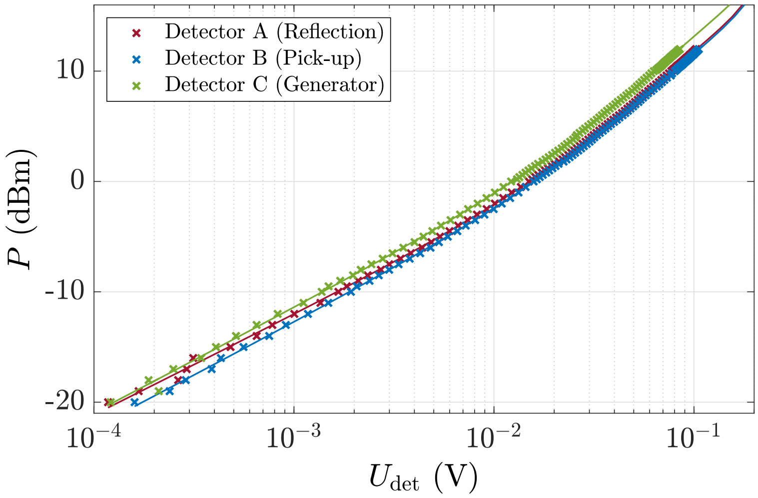

Figure 6.17: DC voltage response U_{det} from three different Schottky diode detectors under application of an RF test signal of power P. Solid lines indicate a general fit model for the calibration of power probing with respect to P_{r} (red), P_{cav} (blue) and P_{g} (green).

Output Current Besides the aforementioned power indicators, the main observable in all experimental MEG studies of this work is related to the amount of charge, that is collected by a specially designed Faraday Cup. It is placed outside the gun cavity in front of the transmissive aperture on top of a supporting structure under vacuum conditions. The cup assembly including a grid attachment is pictured in Figure 6.18, together with a schematic representation of the charge accumulation at the metallic surface from an incident electron beam. Electrons passing the grid thereby hit the cup surface and may, depending on their kinetic energy, also create secondary electrons in addition to their penetration into the material, thus generating holes for a more positive net charge accumulation (cf. Section 2.2.5). To repulse most of the SE, a negative gate voltage U_{gate} of usually -15 V is applied to the grid on a floating potential. Additionally, an

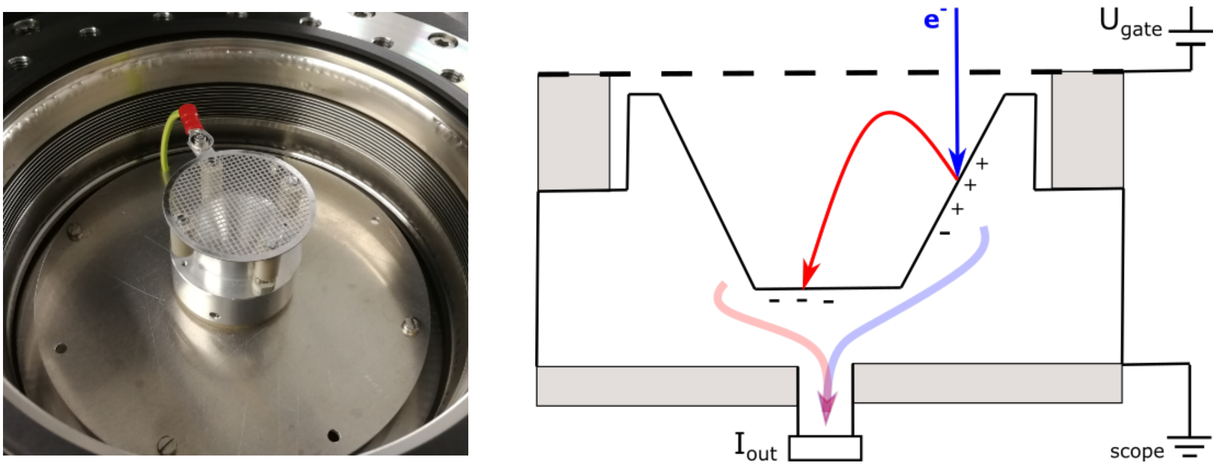

Figure 6.18: Picture of the Faraday Cup including grid, mounted onto a supporting structure inside the vacuum tube (left), and a schematic drawing of the charge accumulation from an incident electron beam at the cup (right). If a negative potential U_{gate} is applied to the grid, more secondary electrons (red) from the cup surface may contribute to the detected current I_{out}.

oblique cup wall orientation is supposed to influence the presumably isotropic emission angle and therefore capture SE electrons more efficiently. Precise drawings of the installed measuring cup are illustrated in the appendix (cf. Figure A.3) for the sake of completeness.

Via a built-in SMA connector at the rear side of the cup, accumulated charges are conducted towards the scope potential, where an electronic voltage U_e is measured from the induced signal. Thereby, U_e drops off over the inner scope resistance of $R = 50\,\Omega$ and is converted into a respective current profile following Ohm's law:

$$I_\mathrm{out} = \frac{U_\mathrm{e}}{R}. \tag{6.9}$$

The corresponding waveform data is saved and analysed with respect to given test conditions. A comprehensive presentation of different experimental studies, in regards to the MEG output at steady state resonance criteria, is the primary aspect of the following Chapter 7.

Measurement Uncertainties There are several systematic error sources that need to be discussed in order to evaluate the acquired measurement data. Not the entire amount of output electrons can be collected, first and foremost, because approximately 25 % of the cup surface is covered by the grid bracing on top. Hence, a large portion of the current I_out is not even registered. Furthermore, the measuring cup with all connectors is not optimised in terms of bandwidth, so that current detection might not be fast with respect to the beam pulses at a 2.998 GHz transmission rate. However, both loss mechanisms should influence each measurement in a similar way, thus currents are comparable relative to each other, but not absolutely.

Added voltage standing wave ratio (VSWR) with every passive component, like connectors, attenuators, or diodes for instance, is another issue. Consequently, power waves are continuously attenuated to some degree until they reach a voltmeter. Precise power indication therefore deviates slightly from the real value. Other constructional error sources can not be accounted for that easily as well. With each reconstruction of the assembly, adjustment of mechanical dimensions, or changing wear parts, the test conditions are changed in a complicated way. Abrasion and also the result of imperceptible misalignments in the translator lengths impede a 100 % reproducibility in the measurement procedure. Thus, great care and accuracy must be ensured to minimise subsequent effects on each measurement in this highly experimental MEG composition.

7 Experimental Results

The hereby presented results from practical MEG performance studies are the basis of all empirical findings in connection to prior theoretical and numerical aspects. In doing so, the main focus lies on the data from experiments with the improved ”Main MEG Test Cavity” in Sections 7.2 and 7.3. Since a decent amount of effort went into the investigation of prior cavity designs, also charge collection measurements from the ”Prototype Cavity Design” are presented beforehand. All in all, research connected to the findings in this chapter is supposed to build a deeper understanding of the resonant multipacting process with our tailor-made MEG test setup including a variety of reasonable operating conditions.

7.1 Experiences with the Prototype Cavity

Besides successful proof-of-principle results of stable gun operation over a period of some microseconds, workings with the early cavity design are rather part of elementary learning processes. The experimental procedure lacks consistency and reproducibility because of systematic malfunctions by design. Therefore, selected data leading to major improvements and changes to the fundamental setup are presented in the following.

Data Interpretation and Systematic Procedure

The most common drawback in the commissioning and operation of the MEG cavity from Figure 6.1 is in finding resonant multipacting, and thereby a visible Faraday Cup signal, in general. Considering needed gap voltages in the order of a few hundred volts (cf. Figure 4.8), a first approximation of the transmitted power P_{cav} can be estimated with respect to wall losses following Eq. (3.33). Large shunt impedances of about $1\,\text{M}\Omega$, found with CST, suggest a rather small input power not higher than 27 dBm. Even if in reality the shunt impedance was as low as $\sim 10\,\text{k}\Omega$, power transmission into the cavity of more than 45 dBm would not be expected to fulfil the resonance condition. However, steady state multipacting could not be observed in this low input power range, while operating in pulsed mode. Most likely it is the consequence of a very small probability to ignite initial SE sufficiently at small gradients, where field emission is strongly suppressed as the source of first free electrons to begin with.

At higher cavity fields the presence of some sort of multipacting has been detected on a regular basis, as shown in Figure 7.1 for example. This illustration mainly demonstrates the raw data acquisition of the output current signal, as well as the respective power information, over the pulse duration in general, as described in Section 6.3.3. At that time the generator power had not been recorded simultaneously. Also more precise ways of determining the most important experimental conditions, concerning power consumption, were still in development. For the specific measurement in Figure 7.1, however, the gap distance was set to $d = (1.15 \pm 0.05)\,\text{mm}$. Loaded cavity quality and the coupling strength were determined as $Q_{\text{L}} \approx 1100 \pm 100$ and $\kappa \simeq 0.40 \pm 0.02$, respectively.

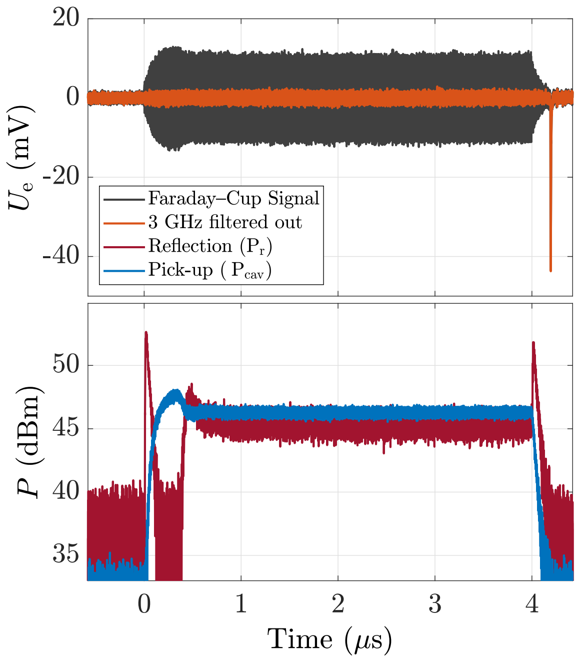

(a) Stable multipacting situation

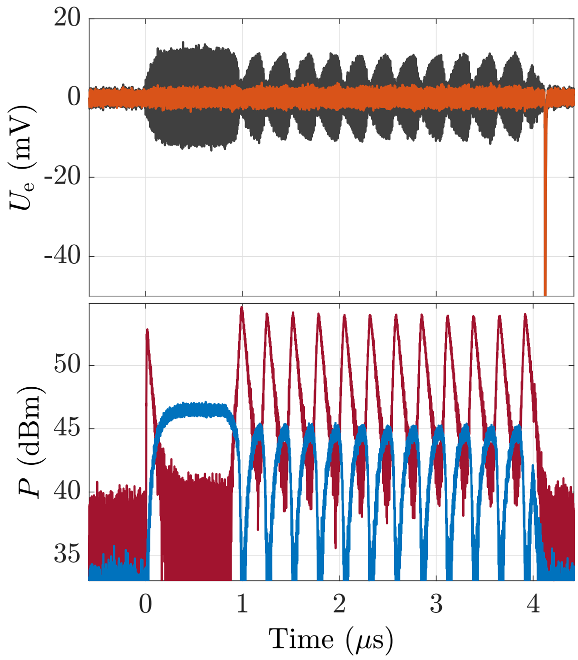

(b) Sequential multipacting quenches

Figure 7.1: Illustration of two multipacting scenarios with the prototype cavity. The induced voltage U_e in the Faraday Cup (upper part) is presented during the RF time period, together with the associated reflected (P_r), and transmitted power P_{cav} (bottom part), measured after coupling into the cavity.

As the field starts to build up inside the cavity at $t = 0$, also the induced voltage at the measuring cup increases. This is significantly visible because of radiation leakage through the outside slit at the cavity border, which should have been avoided by quarter-wave impedance transformation. In fact, the effect happened to be highly influenced by the slit size and additional shielding of the cup itself. The signal, subsequently reduced by its 3 GHz component, shows a substantially lower noise amplitude after post-processing.

Whenever any electrons are accelerated after secondary generation, the additional load on the cavity results in a decreased amplitude of the recorded power inside, visible in both situations, (a) and (b). Simultaneously, the measured power reflection increases since the exiting wave pattern interferes with the reflected wave to a minor degree. With that in mind, Figure 7.1a denotes a passive measurement of steady state multipacting until the end of the RF pulse without charge collection on the Faraday Cup. In Figure 7.1b, no output current is detected as well, but many successive phases of multipacting describe a different situation. No active changes to the experimental conditions between both measurements were made. Thus, sudden changes in the measurement observables, together with lacking reproducibility, indicate an overall unstable configuration. Worth mentioning at this point are the peaks in signal at $t > 4\,\mu$s, when the cavity field is reduced. With hindsight, this demonstrates electron emission through the cavity aperture at much smaller field gradients. The presence of a decent amount of free electrons for starting the resonant multipacting process in the cathode region is mandatory, at least in pulsed mode operation, where the ignition must be obtained within the first few microseconds.

7.1.1 First Proof-of-principle Results

Besides the common observation of steady state multipacting indicated by the power probe signal, also a simultaneous increase in cup voltage could eventually be measured. An illustrative visualisation of the raw data is presented in Figure 7.2, accordingly. Similar to the demonstration in [113], it can be seen that when the SE generation process is ignited at $t \simeq 0.8\,\mu$s, charge collection at the Faraday Cup results in a negative voltage increase with the additional drop in field strength due to beam loading. Since the measuring cup has a small bandwidth compared to the presumably pulsed electron signal, the induced voltage is detected uniformly during the steady state multipacting process.

A closer look into the onset region shows a damped oscillation of the electronic signal U_e before entering the steady state. It can well be explained with the model of equivalent impact energies (cf. Figure 4.5) resulting in a higher SE yield, when the accelerating field causes large primary energies. After the charge density increases significantly, the overall yield decreases due to the reduced gradient, as validated numerically in Chapter 5. However, it is notable that the electronic signal has a delay of about 100 ns in comparison to the passive multipacting detection from the probe signal. This is an indication of SE sources inside the cavity, but outside of the designated area around the transmissive aperture. In this way, it might be possible that resonant multipacting inside the cathode gap is ignited by starting particles from other sources, but under the influence of a smaller local acceleration voltage, where the resonance condition can be fulfilled and particles are ejected.

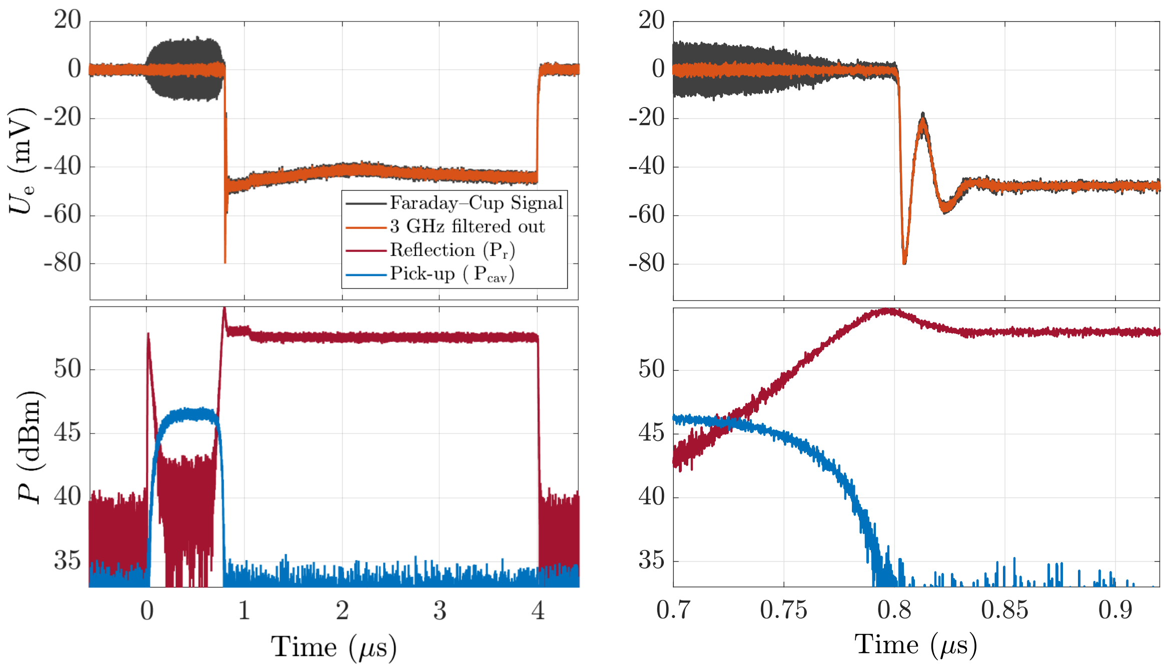

Figure 7.2: Measurement data of a steady state MEG current during a $4\,\mu$s RF pulse (left). Particular importance is given to the unstable onset region of resonant multipacting by zooming into a smaller time frame (right).

By looking at the upper surface of the complementary aperture plate, the assumption of other SE sources is solidified. Figure 7.3 shows a picture of that surface taken after the aforementioned experiments. A circular discolouration is barely visible, which indicates discharge between both cavity parts across the outside slit. This issue becomes problematic at a power level $P_{\mathrm{cav}} > 45\,\mathrm{dBm}$, and there are additional radiation losses also at smaller energies. Hence, the first cavity design is prone to unwanted features in the experimental procedure. Together with the fact that some source of free electrons must be available at smaller acceleration fields, it has been necessary to construct an improved MEG cavity for further testing.

Figure 7.3: Picture of the aperture plate taken after multipacting experiments. As a consequence of electronic discharge and heat, a circular discolouration has been created on top of the aluminium surface.

7.2 Main MEG Test Cavity in Pulse Mode Operation

This chapter is all about the results from parameter studies in use of the improved test setup including the "Main MEG Test Cavity" from Figure 6.3, which was operated by a pulsed power generator at first. With the goal of gaining fundamental understanding and experience in regards to the resonant multipacting process, different sets of suitable working parameters could be achieved. Thereby, the more important figures of merit are the output current and the longitudinal energy spectrum of the corresponding electron bunches. In the context of raw data acquisition and the general experimental procedure, the following settings are used consistently throughout all measurements:

Pulse Duration $t_{\mathrm{rf}} = 8\,\mu\mathrm{s}$

Near to maximally possible time of constant RF power supply, with the pulsed amplifier, for an increased probability of multipacting along the time period of one pulse.

Pulse Repetition Frequency $f_{\mathrm{rf}} = 100\,\mathrm{Hz}$

For the same reason of an increased success rate of detecting resonant electron emission, the repetition rate is set to the maximal value possible.

Sampling Rate $SPS = 10\,\mathrm{GS/s}$ (100 ps/point)

Reading of 100 kS over the course of $10\,\mu\mathrm{s}$ implies the best signal-to-noise ratio for measuring the DC cup voltage, while also providing sufficient data to limit statistical error sources within a single measurement.

Trigger Setting Edge trigger on U_e, or P_g

Each single measurement is triggered on the rising slope of either the induced Faraday Cup signal, or the provided generator power.

Another example of a measured MEG current signal, together with the corresponding power detection, is given in Figure 7.4. The acquired cup voltage is averaged by limitation of the upper measurement frequency to 200 MHz. This eliminates the most common noise components, which are transferred from other hardware elements, like the control electronics of the turbo pump for example. A gate voltage of $U_{\text{gate}} = -15\,\text{V}$ is applied to the grid in front of the measuring cup in all instances.

The single measurement here shows similar features compared to the results from Figure 7.2, whereas the trigger is shifted towards the current onset instead. For further quantitative studies in this chapter, the stable output current I_{out} is calculated from the averaged multipacting (MP) electron signal presented in the upper frame. Thereby, the induced voltage U_e drops off over the ohmic $50\,\Omega$ scope impedance following Eq. (6.9), equally and thus comparable for all measurements. Unfortunately it can not be accounted for charge accumulation on the retarding grid in front of the cup (cf. Figure 6.18), which naturally results in the detection of a decreased current overall. The initial cavity power $P_{\text{cav},0}$ could be reduced significantly in comparison to experiments with the prototype cavity in any case. Continuous UV irradiation of the designated cathode area furthermore enables the emission of primary electrons.

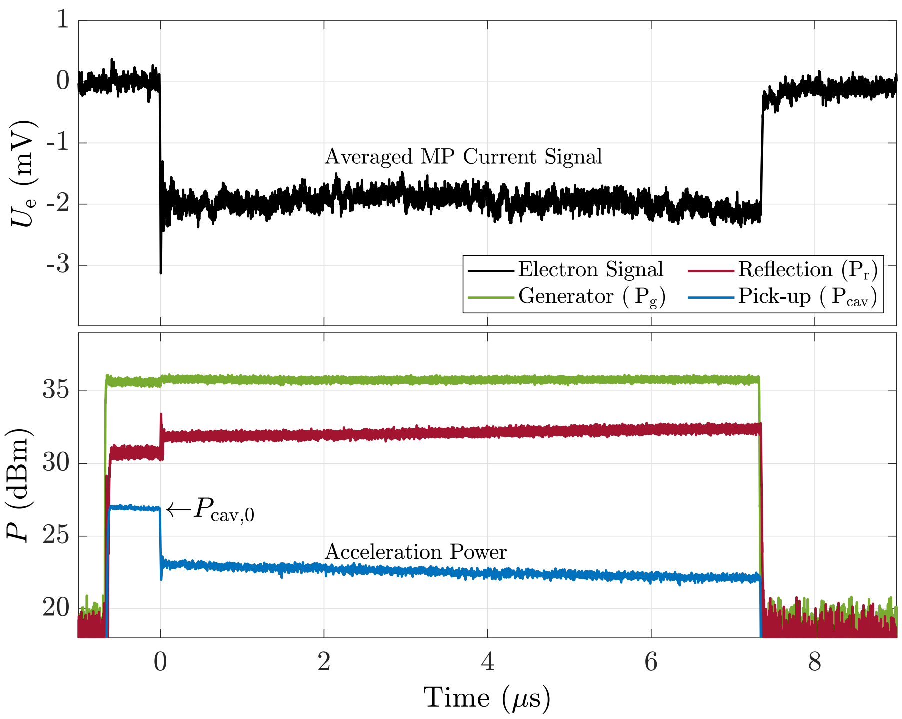

Figure 7.4: Exemplary set of MEG measurement data showing the induced voltage U_e of a steady state multipacting current from the improved cavity. In the bottom frame, corresponding power signals in regards to the forward power amplitude P_g, reflected power P_r and accepted power by the cavity P_{cav} are presented as functions of the same time.

7.2.1 MEG Resonance Condition and Stable Output Current

In analogy to the tracking simulations in Chapter 5, where the resonance condition is analysed in terms of cathode distance d and acceleration voltage U_0, results from similar parameter studies are presented here using the improved cavity design. Since the actual field gradient is unknown due to a questionable shunt impedance, the measured initial power $P_{\mathrm{cav},0}$ (cf. Figure 7.4) is used to represent the accelerating field strength. For a better clarification of the experimental procedure, Figure 7.5 is presented showing selected current measurements at $d = (1.20 \pm 0.01)$ mm and $\alpha \approx 0°$ under variation of the generator power. Thereby, the measured voltage from electron ejection of the gun U_e is assumed to be proportional to the total charge inside the cathode gap volume, as supported by prior calculations in Section 5.3, accordingly.

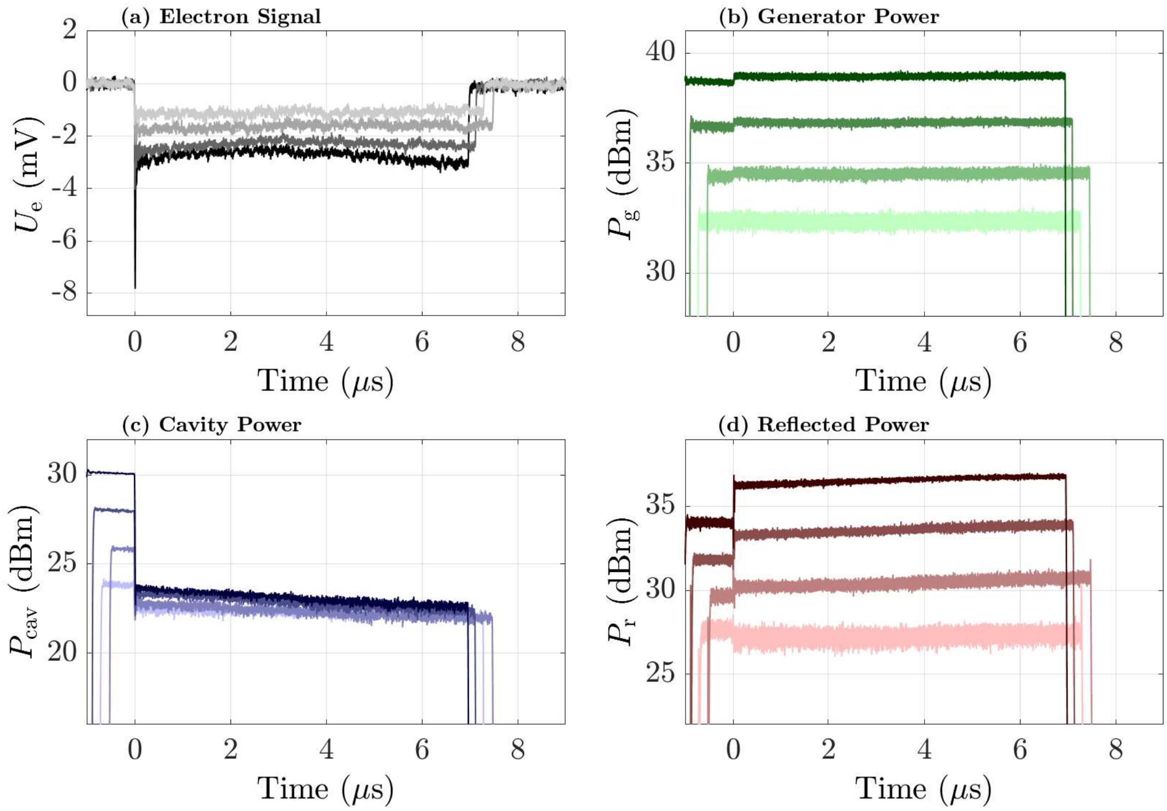

Figure 7.5: Steady state MEG current signals with changing input power starting inside an 8 μs RF pulse. Besides the Faraday Cup signal U_e (a), also the corresponding power signals of the generator (b), stored energy (c), and reflection at the coupler are shown accordingly. In doing so, measurements represented by a similar colour intensity are related to each other.

Any adjustments to the mechanical configuration in the experiment, like changing d, or α, influences the electrical cavity properties decisively as well. Therefore, Table 7.1 is given as an overview of the different individual measurement conditions in order to compare and interpret emerging results comprehensively. In the course of first investigations regarding the resonance condition and the corresponding MEG current profile, measurements in dependence of the cathode distance d are performed by ramping up the external power supply at each setting. This is done for two different loop angles α (cf. Figure 6.3b), which is supposed to change the

Material	α ($\pm 5°$)	d (mm ± 0.01)	κ_{in} (± 0.05)	κ_{out} (± 0.005)	Q_{L} ($\pm 2\%$)
Aluminium	45°	0.65	0.83	0.091	338
(Al)	”	0.80	0.98	0.098	321
	”	1.00	1.21	0.107	316
	”	1.20	1.29	0.107	303
	”	1.40	1.43	0.116	303
	”	1.60	1.50	0.117	302
	”	1.75	1.60	0.120	304
Aluminium	0°	0.65	2.20	0.052	177
(Al)	”	0.80	2.53	0.052	157
	”	1.00	3.01	0.057	149
	”	1.20	3.31	0.055	142
	”	1.40	3.39	0.056	134
	”	1.60	3.76	0.058	131
	”	1.75	3.92	0.058	132

Table 7.1: List of adjustable experimental parameters in association with the results in Figures 7.6 and 7.7. The resonance frequency is always tuned close to $f_0 = 2.998\,\mathrm{GHz}$, while obtaining the MEG resonance condition. Aluminium is the cathode material of choice here.

coupling strength κ_{in} and hence the loaded quality factor Q_{L}. Resonant multipacting alongside a steady state MEG current could be observed by transmission of sufficient input power over the entire span of selectable gap sizes in both coupling situations.

The measured cavity power P_{cav} maintaining the steady multipacting current is plotted in Figure 7.6. Because of better comparability with the charge tracking results from Figure 5.4, values are given in watts, here. At first glance, the remaining field energy inside the cavity increases with larger d and the resonance condition in terms of power enlarges as well. Both findings draw a congruent picture to theoretical expectations. The development of $P_{\mathrm{cav}}(d)$ can also be fitted by the analytically derived gap voltages semi-empirically. A constant C_α is used to modify U_{g} and $U_{\mathrm{g}}^{f,t}$, in regards to the coupling situation, respectively yielding:

$$C_{45} = 1.43 \cdot 10^{-7} \qquad (\text{for } \alpha \approx 45°)$$
$$C_0 = 3.33 \cdot 10^{-7} \qquad (\text{for } \alpha \approx 0°)$$

In consideration of wall losses only, causing a uniform accelerating voltage U_0, the transmitted power would dissipate as

$$P_{\mathrm{cav}} = C_\alpha \cdot U_0^2 = \frac{U_{\mathrm{g}}^2}{2R_{\mathrm{s}}} \tag{7.1}$$

where C_α mainly consisted of the shunt impedance R_{s}. Even though the R_{s}-over-Q ratio (cf. Eq. (3.34)) is changed a bit by adjustments to the cathode position, it should be nearly constant throughout the measurement procedure, since it is a fundamental quantity of the cavity geometry

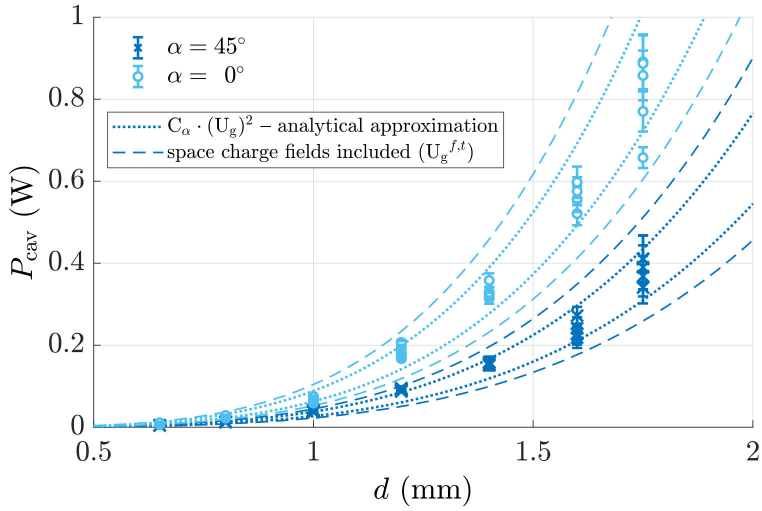

Figure 7.6: Acceleration power P_{cav} as a function of the gap distance d for different input power values and two coupling situations $\alpha \simeq 0°$, and 45°. The dotted lines represent modified fits including the theoretically expected resonance voltage U_{g}, whereas the dashed lines also involve space charge forces.

only. However, when the loaded quality factor decreases by ~50 % in the case of stronger coupling, power is transferred faster within the process of SE generation and beam loading. Precise quantifications of the realistic resonance condition can therefore not be derived without including the coupling situation. Additionally, the huge difference in C_α between both settings by a factor of ~2.3 is likely to be influenced by the measurement as well. It is unknown to what extent large multipacting currents are thereby affecting the field strength at outer positions, where the probe is positioned, and how it scales with the cathode field. Also different impacts of cavity detuning by beam loading may be changing the power transmission (cf. Section 3.4).

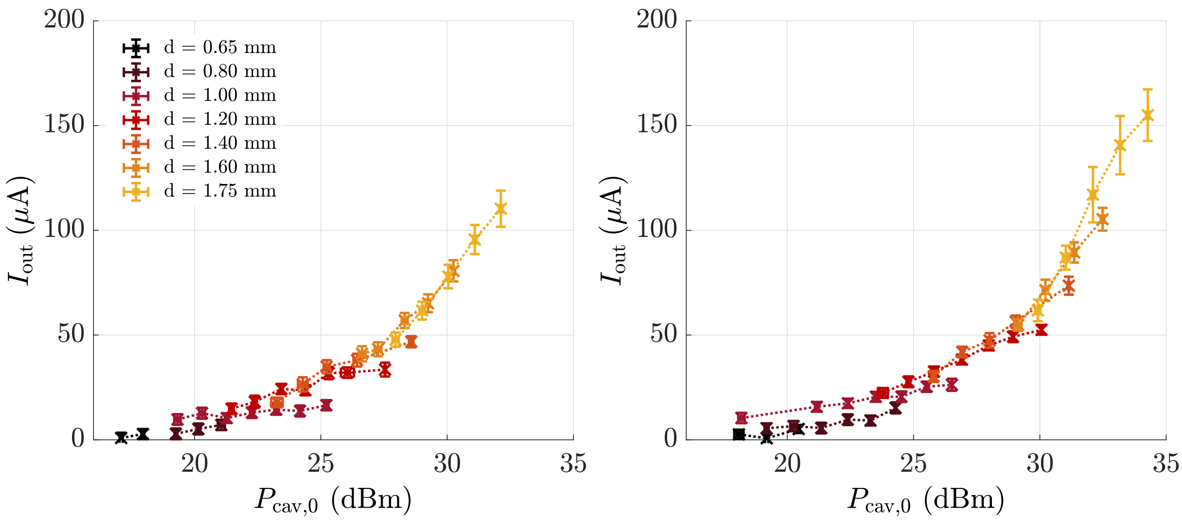

(a) $\alpha \simeq 45°$ (b) $\alpha \simeq 0°$

Figure 7.7: MEG output current I_{out} as a function of the initial cavity power $P_{\text{cav},0}$ for different gap sizes d as well as two loop angles $\alpha \simeq 45°$ (a), and $\alpha \simeq 0°$ (b). The dotted lines are displayed as a guide to the eye. Error bars indicate statistical uncertainties of a single measurement.

A closer look is given to the average output current I_{out} under steady state multipacting concerning the two coupling conditions. While Figure 7.7a shows the rather critically coupled situation around $\kappa_{\text{in}} \approx 1$, Figure 7.7b indicates the gun performance at a level of supercritical coupling. The current increases constantly with increased initial gradient in both illustrations. For faster cavity filling, however, more charge is collected due to the accessibility of resonant multipacting with more acceleration energy, similarly at all distances d. These findings strongly support our previous expectations and prove that modifications to both, gap voltage and gap size, affect the amount of output current significantly.

7.2.2 Influence of the Coupling Strength on the Current Gain

To further stress the question about gun performance in terms of coupling strength, measurements involving a greater span of loaded cavity quality factors were taken. A list of the underlying settings, together with the results from VNA characterisation, is presented in Table 7.2. Steady state multipacting currents are observed with all of the five coupling situations at three distinct gap distances d. Thereby, adjustments to the loop angle are tuning the coupling factor κ_{in} up to ≈ 3.5. Sometimes the wire became loose and had to be reattached to the feed-through, hence the conditions were not precisely reproducible. In the case of $\alpha \sim 30°$(*), a whole different loop including two windings was installed to access even higher κ_{in}. Additionally, it is noticed that frequent movement of the translators and therewith excessive friction of the contact

Material	d (mm ± 0.01)	α ($\pm 5°$)	κ_{in} (± 0.05)	κ_{out} (± 0.005)	Q_{L} ($\pm 2\%$)
Aluminium	0.80	75°	0.39	0.125	366
(Al)	”	60°	0.80	0.104	329
	”	45°	1.12	0.103	224
	”	0°	2.92	0.053	157
	”	30°(*)	4.26	0.049	55
Aluminium	1.20	75°	0.52	0.147	373
(Al)	”	60°	0.93	0.109	294
	”	45°	1.65	0.124	218
	”	0°	3.51	0.056	138
	”	30°(*)	4.03	0.055	48
Aluminium	1.60	75°	0.57	0.153	369
(Al)	”	60°	1.05	0.109	287
	”	45°	1.75	0.121	207
	”	0°	3.48	0.055	131
	”	30°(*)	6.62	0.053	35

Table 7.2: List of adjustable experimental parameters in association with the results from Figures 7.8 and 7.10. The main focus lies on varying coupling conditions κ_{in} by modifications to the loop angle α. An alternative type of coupler (cf. Figure 6.13c) was used for the measurements marked by (*).

springs on the cavity surface leads to slightly changed measurement conditions as well. The inner surface resistivity, and therefore the overall quality factor, is consequently inconsistent over time. However, κ_{in} and Q_{L} are determined directly after the corresponding measurements in any case, so their value is meaningful despite constructional uncertainties.

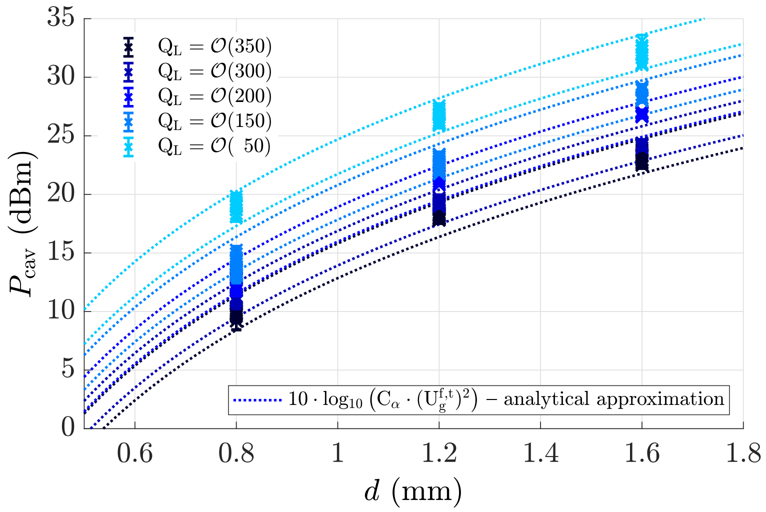

Figure 7.8: Acceleration power P_{cav} at three distinct gap distance d for different generator power and five coupling conditions, described by the order of loaded cavity quality $\mathcal{O}(Q_{\mathrm{L}})$. The dotted lines represent modified fits of the analytically expected voltage span $U_{\mathrm{g}}^{f,t}$ in logarithmic scale.

Similar to the aforementioned plots in Figure 7.6, featuring the resonant condition for two coupling strengths, Figure 7.8 shows the complementary results in consideration of more coupling scenarios. The measured power (in dBm) inside the cavity increases with d again for all different coupling strengths, which are classified by the order of loaded Q this time. Fitting the data semi-empirically with the estimated space charge gap voltage $U_{\mathrm{g}}^{f,t}$, and Eq. (7.1), results in individually modified power constants C_α. In order to evaluate their functional dependency on measurable quantities, Figure 7.9 is given. There, C_α is plotted against κ_{in}, the averaged Q_{L} and Q_0, and also the maximally achieved output current $I_{\mathrm{out,m}}$ at maximum d (cf. Figure 7.10c), in a first approach.

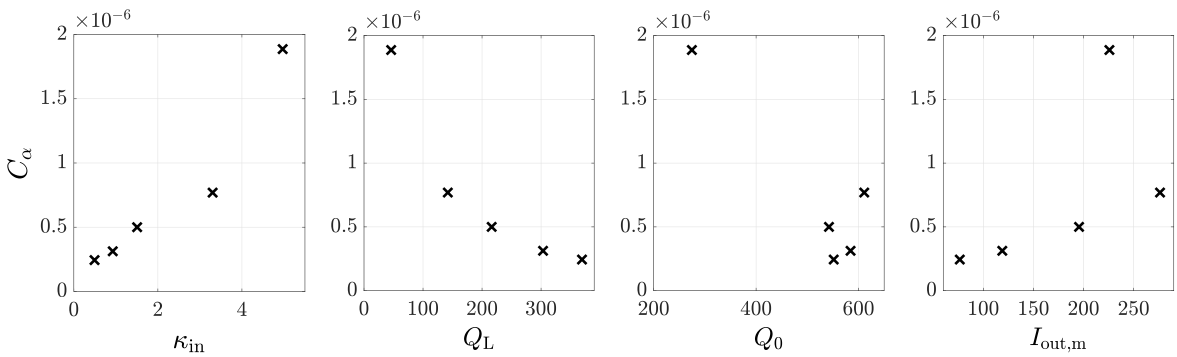

Figure 7.9: Fit modification constant C_α as a function of four measurement observables in connection to different coupling conditions. Q_0 is determined by means of Eq. (3.36).

The resulting illustrations indicate an explicit correlation of the form of the resonance condition, as it is represented by C_α, to the conditions that are related to external power losses, κ_{in} and Q_{L} specifically. If the data is not substantially influenced by measurement uncertainties and therewith unreliable, several power loss mechanisms are probably included in C_α at once. Coupling using the double-loop wire ($Q_{\mathrm{L}} = \mathscr{O}(50)$) leads to a totally different structure and stands out consequently.

While there are generally more uncertainties about the validity of a measured power inside the cavity amongst strong multipacting, relative differences in the actual MEG current between distinct measurements are more directly related to the gun performance. In accordance with the overview in Table 7.2, the output current I_{out} as a function of the acceleration voltage, rep-

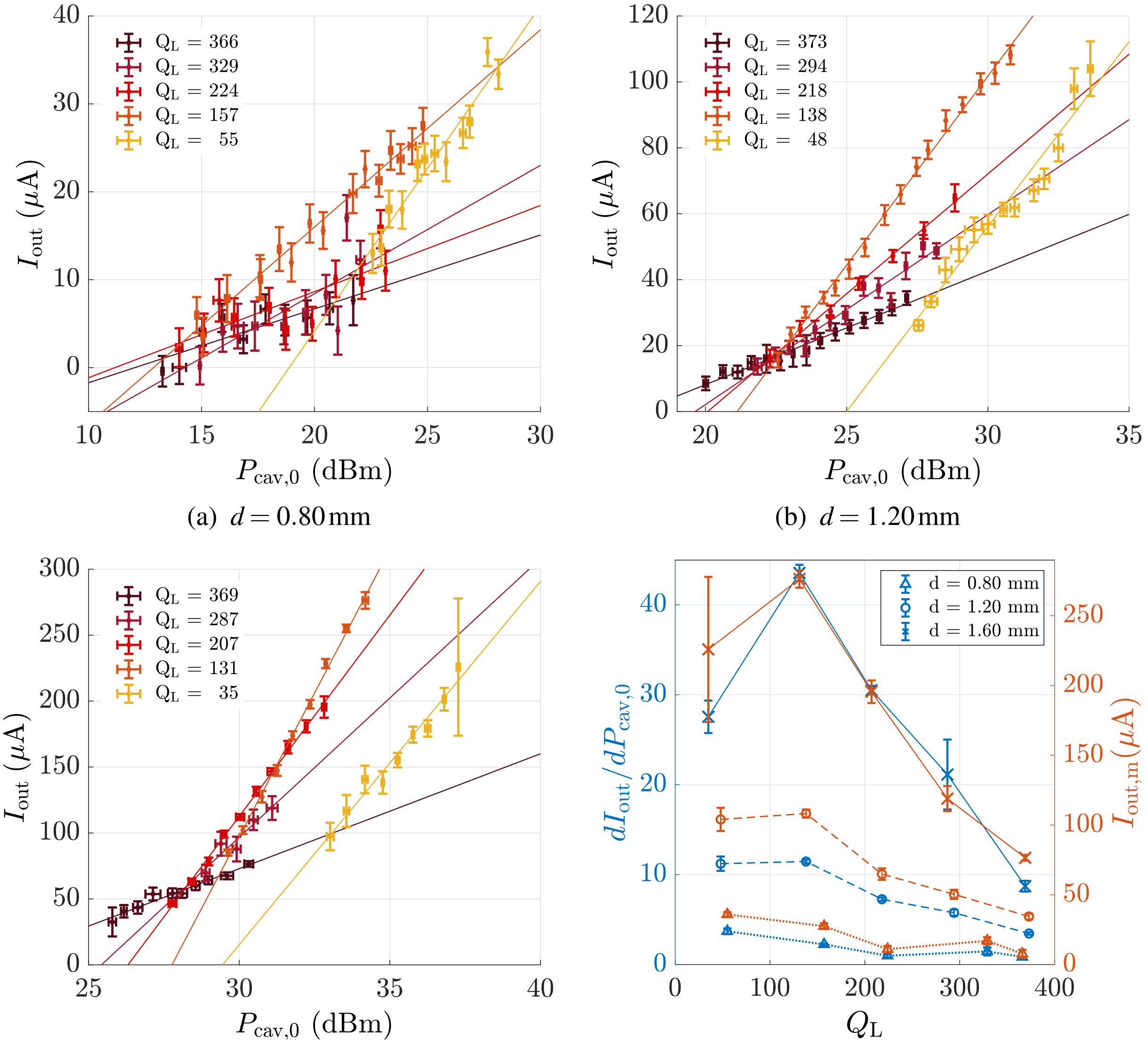

(a) $d = 0.80$ mm

(b) $d = 1.20$ mm

(c) $d = 1.60$ mm

(d) Slope and maximum of $I_{\mathrm{out}}(P_{\mathrm{cav},0})$

Figure 7.10: Output current I_{out} as a function of initial cavity power $P_{\mathrm{cav},0}$ for different coupling conditions in terms of the loaded quality factor Q_{L}. Results involving three cathode distances $d = 0.8$ (a), 1.2 (b) and 1.6 mm (c) are illustrated separately. The solid lines represent linear fits to the measurement data, whose derivative is plotted versus Q_{L} in (d), together with the maximally achieved current values $I_{\mathrm{out,m}}$.

resented by the initial cavity power $P_{\mathrm{cav},0}$, is given in Figure 7.10. For a better perceptibility concerning the different coupling conditions, a distinction between set gap sizes is made within Figures 7.10(a-c). Similarly amongst all the data appears to be an increased current generation with rising initial cavity power, which is driving the emission and acceleration process. Its functional development is thereby assumed to follow a linear behaviour with the logarithmic power value of $P_{\mathrm{cav},0}$. Both, the current growth rate $\mathrm{d}I_{\mathrm{out}}/\mathrm{d}P_{\mathrm{cav},0}$ as well as its overall obtainable amount $I_{\mathrm{out,m}}$, increase with smaller Q_{L}, thus stronger coupling (cf. Figure 7.10d). An exception to this is seen for the case of super-critically low quality in the order of 50. According to Eq. (3.45) it can be assumed that the energy is transferred to the electron cloud much faster there. An illustration of the underlying induced voltage at large I_{out}, similar initial cavity power and $d = 1.2\,\mathrm{mm}$, is presented in Figure 7.11a for comparison. It can be seen that for smaller Q_{L} the steady state is obtained faster after initial SE ignition, alongside lesser pronounced charge overload in the beginning. Furthermore, the case of $Q_{\mathrm{L}} = 48$ indicates a strong field gradient accompanied by the relatively small output current. Either a smaller fraction of excited particles meeting the resonance criteria, or remarkable cavity detuning by enhanced multipacting discharge and therewith larger external power losses result in a smaller current detection compared to the other measurement series. This would make the detected cavity power P_{cav} less comparable in general, since beam loading induced power losses were pronounced differently. However, in terms of the average MP current at saturation, coupling by an angle of $\alpha \approx 0°$ in

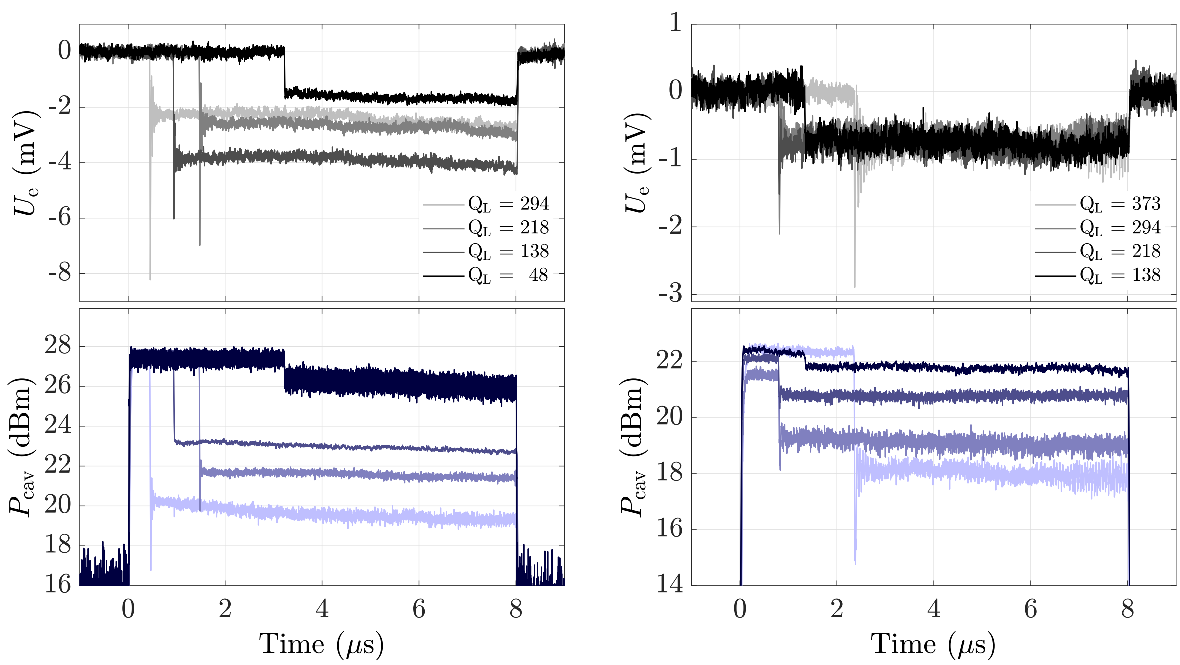

(a) Different I_{out} with same $P_{\mathrm{cav},0}$ (b) Intersection point of both, similar I_{out} and $P_{\mathrm{cav},0}$

Figure 7.11: Steady state MEG current signal U_{e} (top) and the corresponding cavity power P_{cav} (bottom) for the comparison of results from two remarkable experimental compositions. A situation in reference to Figure 7.10b of same $P_{\mathrm{cav},0}$ and varying Q_{L} (a) is illustrated alongside an intersection point (b), where also the registered multipacting currents are equal in saturation. Plots of same colour intensity are affiliated in this context.

connection with a quality factor around 130 suggests the best results so far.

Another noteworthy observation is related to the point in Figure 7.10b, where the same amount of output charge is measured under steady state multipacting at a quite similar initial field gradient for the involved coupling situations. By looking at the detected cavity power it is indicated that faster coupling results in an overall smaller power drop in continuity of the resonant condition involving similar gun charge. This gives rise to the possibility of coupling more energy into the system, since the steady multipacting state is remaining accessible at even larger gap voltages.

7.2.3 Current at High Gradient and Maximum Gap Size

Ultimately, the preceding charge collection study in special consideration of coupling strengths shows the highest obtainable output currents with the largest gap size, as illustrated in Figure 7.10c for $d = 1.6\,\mathrm{mm}$. In the course of various measurement procedures, not only this one, it is observed that the multipacting current becomes somewhat inconstant over time along the pulse duration of several microseconds, when large cathode distances are applied. To give a more detailed description of what happens exactly, Figure 7.12 is given.

After initiation of steady state multipacting the resulting current increases rapidly, whereby the acceleration energy suffers from overcharging due to strong charge amplification at rather high equivalent impact energies of the related electrons. Thereby, the cavity field reacts slower

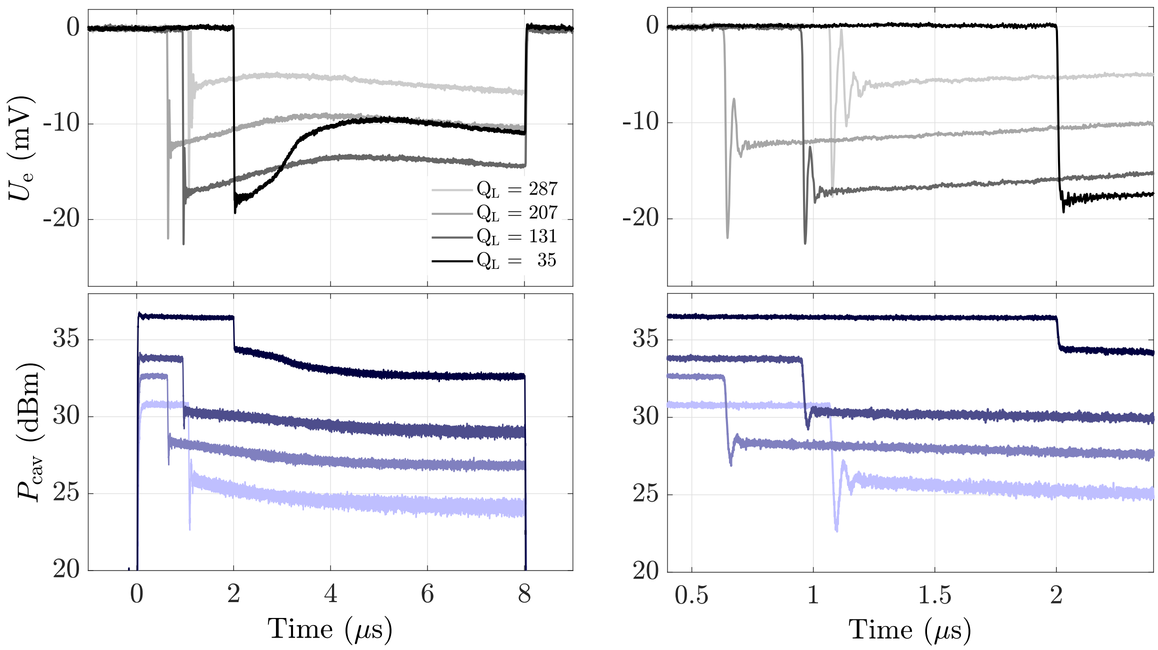

Figure 7.12: MEG current signal U_e (top) and the corresponding cavity power P_{cav} (bottom) are plotted over the course of an RF pulse involving nearly the highest possible field gradient in terms of steady state accessibility. The four plots on the left represent raw data in accordance with the maximum current $I_{out,m}$ at $d = 1.6\,\mathrm{mm}$ in the different coupling scenarios regarding Figure 7.10c (Second highest I_{out} for $Q_L = 35$). A closer look into the onset region is provided on the right side.

to the additional load at weaker coupling (larger Q_L) and therefore the saturation process is subject to more significant oscillations, as seen in the downsized frame on the right. While entering steady state conditions, the detected charge decreases further until entering another period of almost constant behaviour. This could again be explained by the sensitive power transmission into the cavity with respect to the strong multipacting discharge. Induction of heat and a changed inner resistance might thereby add mismatch to the generator and cavity impedances. In the case of $Q_L = 35$, where the double-loop wire (cf. Figure 6.13c) is used for coupling, the resonance frequency could have been shifted even more substantially. The MEG current signal is decreased significantly in that case. All this of course under the assumption that energies inside the cavity are measured correctly by the probe, which might as well be detuned in the process of heavy electron discharge.

7.2.4 Energy Spectra of the MEG Current

By variable application of a constant negative gate voltage to the grid, which is mounted in front of the Faraday Cup, as seen in Figure 6.18, some information about the kinetic electron energy distribution can be gained. Single charge collection measurements have therefore been taken collectively to give an idea of the longitudinal energy spread within the output beam under different conditions. Only electrons, whose energy after release is sufficient to overcome the gate potential barrier are thereby contributing to the measured multipacting current, others are deflected. This voltage U_{gate} is directly related to the electron energy by definition of the electronvolt (eV) and leads to an integrated spectrum presented in Figures 7.13 and 7.14, where the amount of current I_{out}, passing the grid at given negative U_{gate}, is displayed. It needs to be mentioned that a significant number of electrons is physically stopped by the grid material, but this can be assumed as equally pronounced in all experiments. However, derivation of I_{out} from the deflection measurements with respect to the retarding potential U_{gate} results in a longitudinal energy distribution within the electron bunch approximately.

Material	d (mm ± 0.01)	κ_{in} (± 0.05)	Q_L ($\pm 2\%$)	$P_{\text{cav},0}$ (dBm ± 0.1)	E_μ (eV± 4)
Aluminium	0.80	2.92	157	22.8	46
(Al)	0.80	1.12	224	22.4	41
	1.20	3.51	138	24.8	35
	1.20	3.51	138	28.1	48
	1.20	3.51	138	30.3	66
	1.60	3.21	129	30.6	64
	1.60	3.21	129	32.6	104
	1.60	3.48	131	32.4	109

Table 7.3: Overview of the underlying experimental parameters and results in regards to the longitudinal energy distribution measurements from Figures 7.13 and 7.14. Thereby, E_μ denotes the expectation value obtained from a Gaussian fit to the measured kinetic energy spectrum.

For comparison, as well as interpretation of the recorded spectra, Table 7.3 lists some key parameters in description of the experimental conditions. Some measurements have been taken alongside previously shown studies, so there is some overlap with Tables 7.1 and 7.2. The expectation value E_μ is obtained from fitting the Gaussian error function to the integrated energy spectra in Figures 7.13 and 7.14. It hereby represents a value, whereat the energy distribution of bunch particles most likely revolves around.

In view of Figure 7.13, the measured multipacting current at $d = 0.8\,\mathrm{mm}$ is given as a function of the deflecting gate voltage for two coupling situations. Even though the statistical error is relatively large at small currents, a decrease with rising U_{gate} is clearly indicated within the first 100 volts. The resulting energy spectra on the right side show small deviations between both test series with an $E_\mu < 50\,\mathrm{eV}$. Regarding the numerical results from Figure 5.14a it is not expected at such low energies. Also the spread is large as a consequence of repulsive space charge fields. Furthermore, it is observed that for voltages $|U_{\mathrm{gate}}| < 15\,\mathrm{V}$ the detected current is comparatively small, since secondary emission and reflection at the Faraday Cup surface creates holes, thus charge losses from escaping electrons (cf. Figure 6.18). A gate voltage of -15 V is consequently used for charge collection measurements in general.

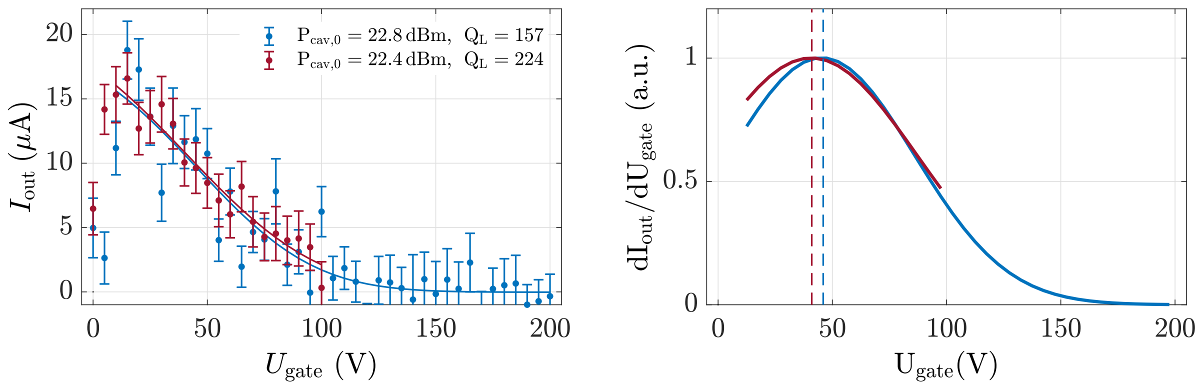

Figure 7.13: Measured integrated energy spectra (left) and their normalised derivatives (right) for multipacting currents involving two different quality factors Q_{L}, and a cathode distance of $d = 0.8\,\mathrm{mm}$. The solid lines are fits in approximation of a Gaussian distribution.

With larger cathode distances, as illustrated in Figure 7.14, the derived kinetic energy increases overall, since more power can be spent for acceleration. In order to maintain a total SE yield of $G \simeq 1$ for steady state multipacting, a sufficiently large number of electrons must thereby carry energies around the $\Sigma_{\mathrm{c,I}}$ point of the aluminium cathodes. Thus, bunches are never being accelerated towards more than a few hundred eV, when ejected out of the cavity. However, both graphics indicate that the overall energy increases with the initial cavity field, as it is suggested by ASTRA calculations in Section 5.4. The scales are way apart in comparison, but it is unclear weather the material properties were taken into account realistically enough for the calculation and if the planar field approximation is sufficient. Additionally, the Faraday Cup is a real object, which is more than a cm away from the point of beam ejection. Space charge forces, together with an accumulated repulsive load on the grid, may spread the longitudinal phase space of the particle distribution furthermore.

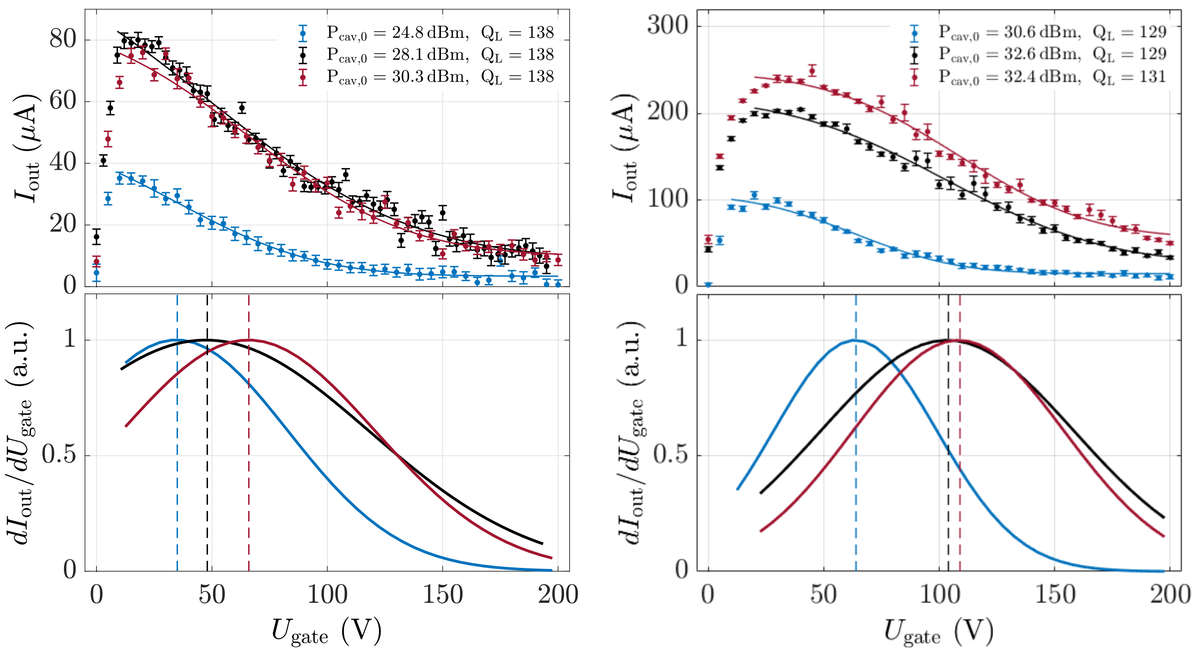

(a) $d = 1.20\,\mathrm{mm}$ (b) $d = 1.60\,\mathrm{mm}$

Figure 7.14: Measured integrated energy spectra (top) and their normalised derivatives (bottom) for multipacting currents sustained by different initial cavity power $P_{\mathrm{cav},0}$ at cathode gap sizes of 1.2 (a), and 1.6 mm (b). The solid lines model a Gaussian distribution once more.

The aforementioned low energy values around 50 eV are also observed by Li et al. [114], who used a similar method to obtain the energy distribution from MEG currents. They conclude that electrons from higher order multipacting modes, where particles need multiple RF half-cycles to reach the subsequent emission surface, are mainly contributing to the stationary MEG current. Low primary energies of less than 50 eV at the aperture position can only be achieved, as long as the total SE gain G is about one, in any case. Hence, secondary generation must be sufficient in the respected energy region.

7.3 Continuous MEG Operation

For their unique mode of operation, multipacting electron guns are theoretically not limited to working under time restrictions, as it is presented so far. In fact, by using a DC/RF power source and delivering the generator power constantly, a pulsed multipacting current can be generated over longer periods of time. This section is covering charge collection studies using an up to 10 W (40 dBm) continuous-wave (CW) amplifier for constant operation of the ”Main MEG Test Cavity”. Thereby, the following settings are used in the procedure of raw data acquisition:

Measurement Period $T_{\mathrm{m}} = 1\,\mathrm{ms}$

The total data acquired within a single measurement is set two orders of magnitude higher in comparison to the pulsed mode operation to possibly observe long time effects in the MEG current.

Sampling Rate $SPS = 100\,\mathrm{MS/s}$ (10 ns/point)

For measuring the induced DC cup voltage, 100 kS are still taken into account over the course of 1 ms. The upper frequency is set to 200 MHz at the same time.

Trigger Setting Edge trigger on P_g

Since the CW amplifier has a long rise time compared to the ignition time of resonant multipacting, single measurements can hardly be triggered on the rising slope of the induced Faraday Cup signal. Thus, one measurement is taken on the falling slope of the switched off power supply with a 200 μs delay to subtract a 800 μs signal from the background.

Global Experimental Conditions

Even though the UV irradiation is not necessarily needed to initiate multipacting for the significantly increased RF time period, it is used for all measurements anyway. The gate voltage thereby remains at $U_{\mathrm{gate}} = -15\,\mathrm{V}$ and the inside pressure before measuring is watched to be $P_{\mathrm{vac}} \simeq 10^{-7}$ mbar at most, because of the increased amount of current in CW operation accompanied by a rise of static pressure.

Within the experimental procedure, no features on small time scales besides the constant Faraday Cup voltage increase in the presence of resonant multipacting currents, could be observed. An example of the underlying measurement data is therefore moved to the appendix, Figure A.10. Output current values I_{out} stem from the averaged cup signal U_e, together with Eq. (6.9), in the time of steady state multipacting.

7.3.1 Comparison of Different Cathode Materials

The modular design of our MEG allows for the replacement of both, cathode attachment on the translator tip (L1), and the opposing aperture plate. Therefore, current measurements involving other materials as well as changed dimensions can be performed. This section is presenting the results from charge collection studies in regards to alternative cathode materials of identically

Material	α ($\pm 5°$)	d (mm ± 0.01)	κ_{in} (± 0.05)	κ_{out} (± 0.005)	Q_L ($\pm 2\%$)
Aluminium	0°	0.80	2.05	0.068	142
(Al)	”	1.00	2.16	0.067	130
	”	1.20	2.85	0.075	134
Copper	0°	0.80	3.13	0.078	158
(Cu)	”	1.00	3.68	0.078	147
	”	1.20	4.03	0.079	141
Stainless	0°	0.80	0.99	0.075	104
Steel	”	1.00	1.06	0.075	97
	”	1.20	1.18	0.079	96

Table 7.4: List of the underlying experimental parameters in association with the results from Figures 7.15 and 7.16 regarding CW operation with three different cathode materials.

sized attachments. A list of key parameters, as the basis of corresponding measurements, is given in Table 7.4.

Respective results including the detected cavity power P_{cav} in Figure 7.15 and the measured output current I_{out} in Figure 7.16 are based on ramping up the power supply within the allowed region of steady state multipacting for three different gap sizes and all materials. Thereby, the recorded resonance condition shows the familiar development $P_{cav} \sim U_g^2$ with respect to the cathode distance at least qualitatively. The data does not fit the modified gap voltage $C_\alpha \cdot (U_g^{f,t})^2$ quite well any more and also the curves are less comparable for strongly different coupling strengths of each material. Higher unloaded quality factors can be achieved by using copper, which benefits from smaller wall losses due to its comparably small surface resistivity and skin depth [115].

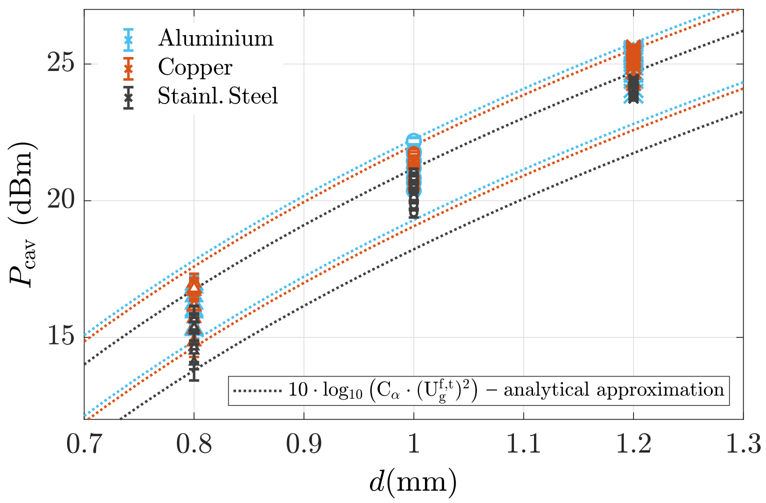

Figure 7.15: Acceleration power P_{cav} during resonant multipacting at three distinct gap distance d for varied generator power and three alternative cathode materials in CW operation. The dotted lines represent modified fits of the analytically expected voltage span $U_g^{f,t}$ in logarithmic scale.

However, previous results indicate best performance in terms of multipacting currents for large coupling constants and $Q_L \approx 100$. A minimum loop angle relative to the magnetic field orientation has thus been adjusted for the current measurements here. With the results from Figure 7.16, I_{out} is plotted against the approximate transmitted power from the generator $P_{g,in}$ according to the limit of P_{cav} in Eq. (3.45), since $P_{cav,0}$ could not be detected directly in CW operation. For each material, except steel, the measured current expectedly increases with d. The data thereby indicates a general current maximum, at given power, independent of the gap size, where I_{out} follows an exponential trend as a function of $P_{g,in}$ for acceleration voltages in the upper region of the resonance condition.

Even thought the time under operation is kept as low as possible, stainless steel suffers from long-term effects, which are limiting the achievable current with time under resonant multipcting. It is described in Section 7.3.2 explicitly. Copper on the other hand promises the highest output current, even in comparison to aluminium, whereas both show similar acceleration power across all gap sizes. This can only be explained by a higher charge density inside the cathode volume as a consequence of the changed material properties. When, for copper, the equivalent impact energy needed to sustain resonant SE generation at $\Sigma_{c,I}$ would be smaller, more charges built up at smaller gap voltages as well. That, in turn, weighted the charge growth rate ahead of responsive beam loading losses at a generally lower power level and thus more particles could be accelerated with the same amount of field energy (cf. Figure 5.8b). It could also be possible that the overall SEY was higher, hence more electrons are generated outside the resonance condition due to an increased SE probability. However, these presumed characteristics do not fit into the picture of technical materials discussed in Section 2.2.5, but it is possible that the evolution of oxide layers on the metal surface is forcing the overall yield towards larger values, and thus greater emission currents [116].

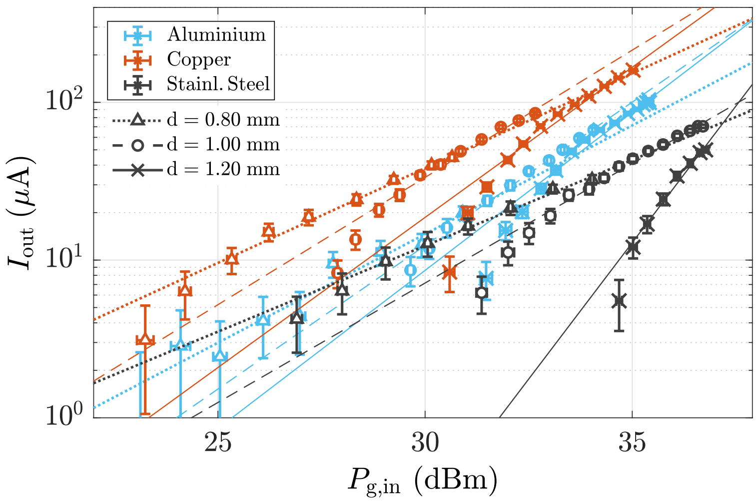

Figure 7.16: Output current I_{out} as a function of the initially transmitted generator power $P_{g,in}$ for combinations of different cathode materials and gap sizes d in CW operation. The lines represent exponential fits to the current data, applied to given measurement series individually.

Energy Spectra in Consideration of the Cathode Material

For the investigation of bunch energy distributions with respect to the cathode material, single measurements of I_{out} have been taken by gradually increasing the gate voltage U_{gate}. The resulting functions are presented in Figure 7.17 for two distinct gap sizes, whereby their general course can be explained similarly to the results in Section 7.2.4. However, the main subject here is the inclusion of alternative SE materials.

The input power in terms of transmission into the cavity is increased in comparison to earlier investigations. Thus, expectation values E_μ of the respective longitudinal energy distributions are increased as well. By looking at Figure 7.17a, copper measurements indicate a higher kinetic particle energy with similar initial cavity power compared to aluminium, whereas stainless steel shows relatively small energies and energy spread at even higher gap voltages. This is most likely related to the equivalent impact energy in maintaining the resonant condition for each individual material, together with the phase range density, in which particles are able to generate a positive net amount of secondary electrons. In a regime of small total bunch charge, differences in the longitudinal energy spread might also be stronger influenced by the materials' SE properties, concluded from the narrow spectra involving steel. Comparison of copper and steel for $d = 1.2$ mm in Figure 7.17b points towards higher possible energies with increasing field strength. Hence, equivalent impact energies from the upper region of the resonance condition are represented.

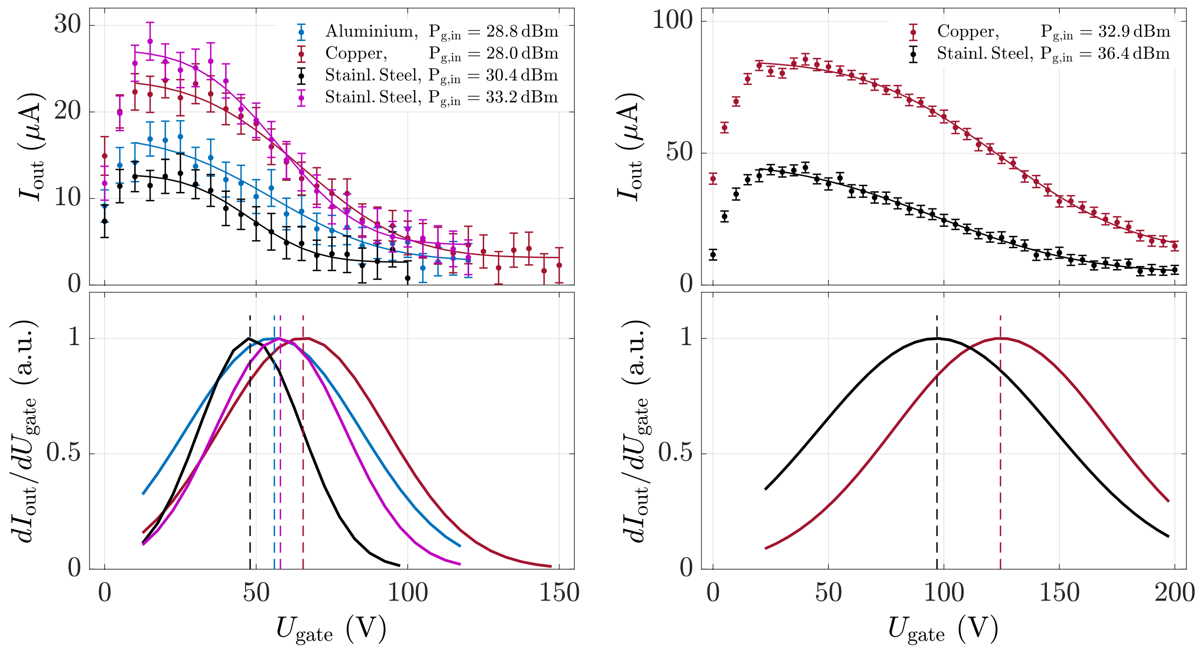

(a) $d = 0.80$ mm (b) $d = 1.20$ mm

Figure 7.17: Measured integrated energy spectra (top) and their normalised derivatives (bottom) for different cathode materials at gap sizes of 0.8 (a), and 1.2 mm (b), in CW operation. The solid lines represent fits involving the Gaussian error function, while the dashed lines indicate most probable energy values E_μ within the electron distribution.

Current from Copper Cathodes at High Gradient and Maximum Gap Size

Besides the studies using continuous MEG operation, a lot of effort went into the generation of resonant multipacting currents in the pulsed mode with copper and steel as well. The success rate in detecting the characteristic voltage increase was thereby found to be significantly lower, which can be traced back to the fact that initial multipacting ignition is less likely there. Photon absorption for copper and steel is generally higher at smaller wavelengths, hence a sufficient amount of starting electrons is not accomplished by customary UV lamps.

In the course of many tests only one measurement series has lead to the detection of resonant MEG currents, as it is illustrated in Figure 7.18 for copper at $d = 1.6$ mm. The steady state accessibility in the current onset is governed by the available initial energy leading to a strong increase within the first few RF cycles again, which is followed by larger oscillations especially at higher initial field gradients. At this point, the rate of charge growth and beam loading losses are unequal and thus their mutual response time becomes delayed. Following the early current drop, a signal increase progressing into the saturation state is observed for all initial power levels on a larger time scale, which could be explained by changing environmental conditions. Local heat induction, or modified energy levels in the surface layer by massive electron bombardment could thereby change the secondary emission properties, as suggested by [117]. Generally, this kind of observation is made at gap sizes $d \geq 1.2\,\mathrm{mm}$, where usually more charges are involved. At the same time, the corresponding acceleration power is the same for all cases, while the overall output current depends on the initial cavity power. Different numbers of electrons can therefore be emitted, in preservation of the resonance condition, during each individual measurement. Excess energy is transferred to the acceleration of these electrons.

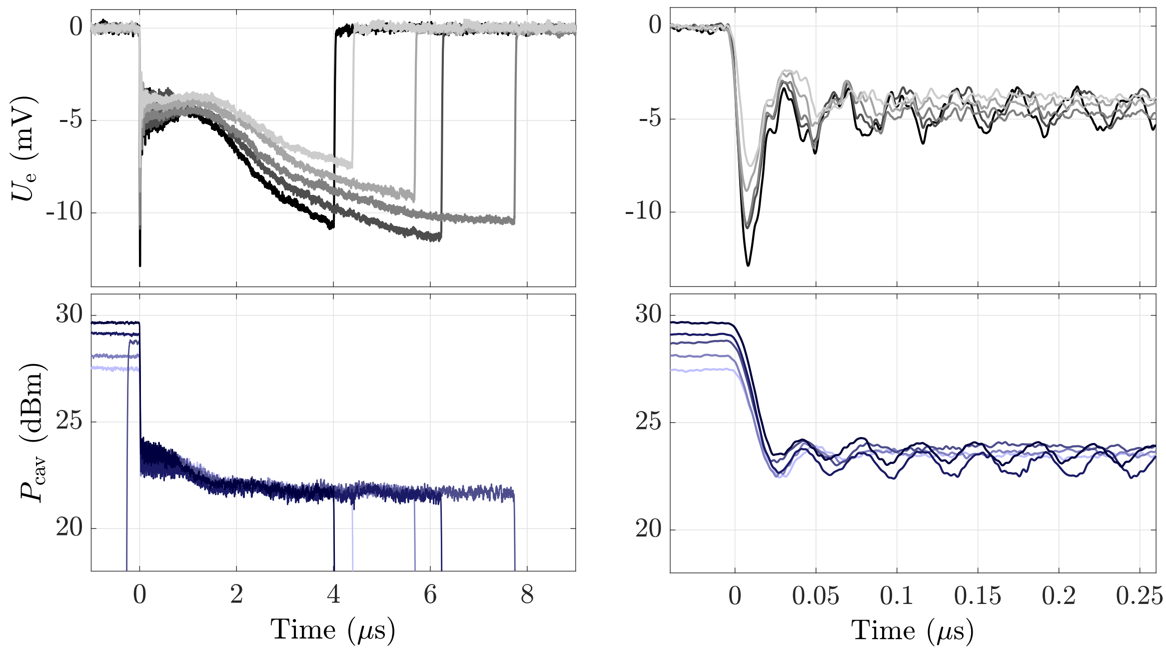

Figure 7.18: Successful multipacting current series in pulse mode operation involving copper cathodes. The current signal U_e and the corresponding cavity power P_{cav} are plotted over the course of an RF pulse for different initially applied power at $d = 1.6\,\mathrm{mm}$. A smaller time frame including the multipacting onset region is provided on the right side.

7.3.2 Time Dependent Current Degradation and Recovery

Previously presented results suggest the causation of long-term effects on the output current in connection to the accumulated time of gun operation and secondary emission. Therefore, charge collection studies with respect to the time under test have been performed, before the replacement of the cathodes with an new set of attachment and aperture plate, respectively. For each different kind of material some sets of time-dependent data have thereby been taken after the experimental procedures of Section 7.3.1. The corresponding results including CW MEG operation at $d = 1.2\,\mathrm{mm}$ are shown in Figure 7.19.

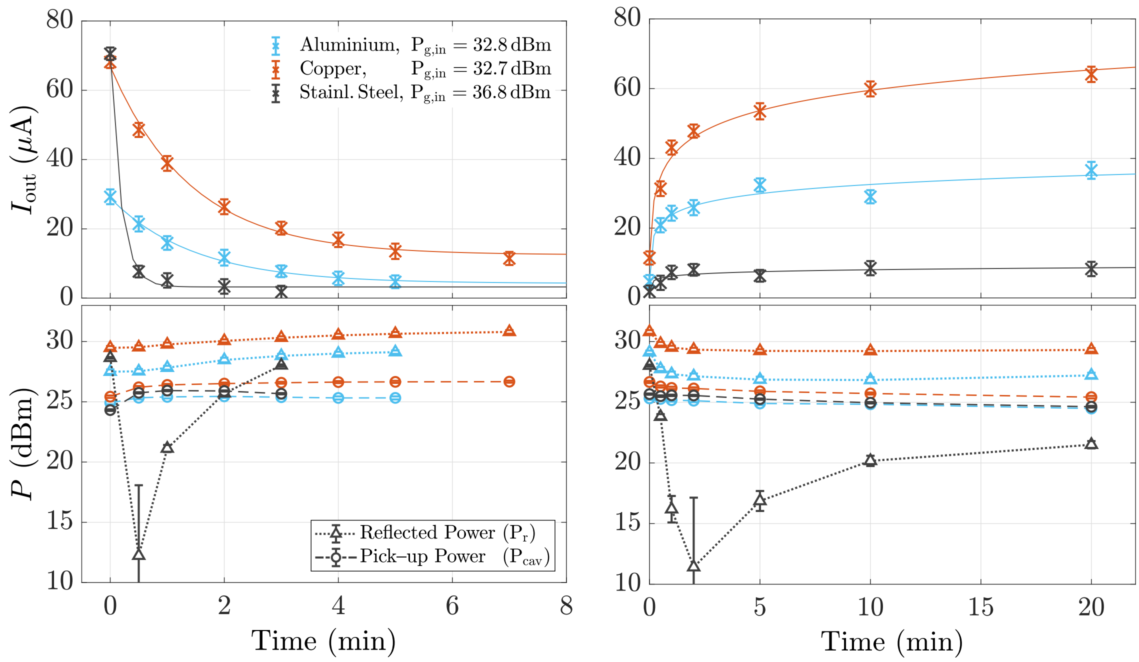

(a) Degradation period (b) Recovery period

Figure 7.19: Output current I_{out} (top) and the corresponding power values (bottom) of the reflected wave P_r and the cavity mode P_{cav} during steady state multipacting at $d = 1.2$ mm in CW operation involving different cathode materials. While in (a) continuous multipacting also occurred between single measurements, the energy supply in (b) is stopped at those times. Solid lines indicate exponential fits to the data, whereas dotted and dashed lines are guiding the eye.

Thereby, the output current I_{out} of consecutive measurements is given as a function of time under non-stop stationary multipacting discharge. Tests involving aluminium and copper are performed at comparable initial cavity power, whereas the steel cathodes are operated at higher energies for a larger current gain. To check for cavity detuning the respective values of power reflection and transmission are displayed simultaneously in both illustrations. However, the I_{out} with time under test in Figure 7.19a follows an exponentially decreasing behaviour across all measurement series, which is especially significant for the steel cathodes. At the same time both, P_r and P_{cav}, are slightly increasing in general, thus confirming changes in total electron numbers, but no severe detuning effect. That is not true in case of steel cathodes, where the power reflection drops substantially after high charge generation. A dynamical effect on the intrinsic cavity properties can therefore not be excluded for steel cathodes.

By looking at Figure 7.19b, where the first data point is equal to the last point of the degradation period and the observables are given with time of no multipacting, steel cathodes are seemingly unrecoverable in terms of maximum output currents. At least not within recovery times of minutes to hours. As for aluminium and copper, however, recoverable starting I_{out} values suggest only temporal material changes, that are affecting secondary emission. The according time constants are thereby in the same order compared to the current degradation period as well. Since also the corresponding power values are slightly decreasing within the recovery period, it can be concluded that the resonance condition is hardly influenced by those effects.

7.3.3 Limitation on Long-Term Operation

Even though there are conditions leading to significantly decreased multipacting currents, which has been reported many times [118, 119, 120], the efficiency of our MEG cathodes is at least partially recoverable. It has thereby not been tested how these effects would limit their overall performance with even longer times of operation, or over several recovery periods. Pictures of the used cathodes, presented in Figure 7.20, show remarkable surface discolourations already after up to 10 minutes of cumulated time under test, which might also be a consequence of low base vacuum ($\sim 10^{-7}$ mbar) and the occurrence of current arcs. However, it can be expected that contamination by even longer periods of use would still not prevent the presence of steady state multipacting. The exact current-power (*I*-*P*) characteristics are likely to change in this case.

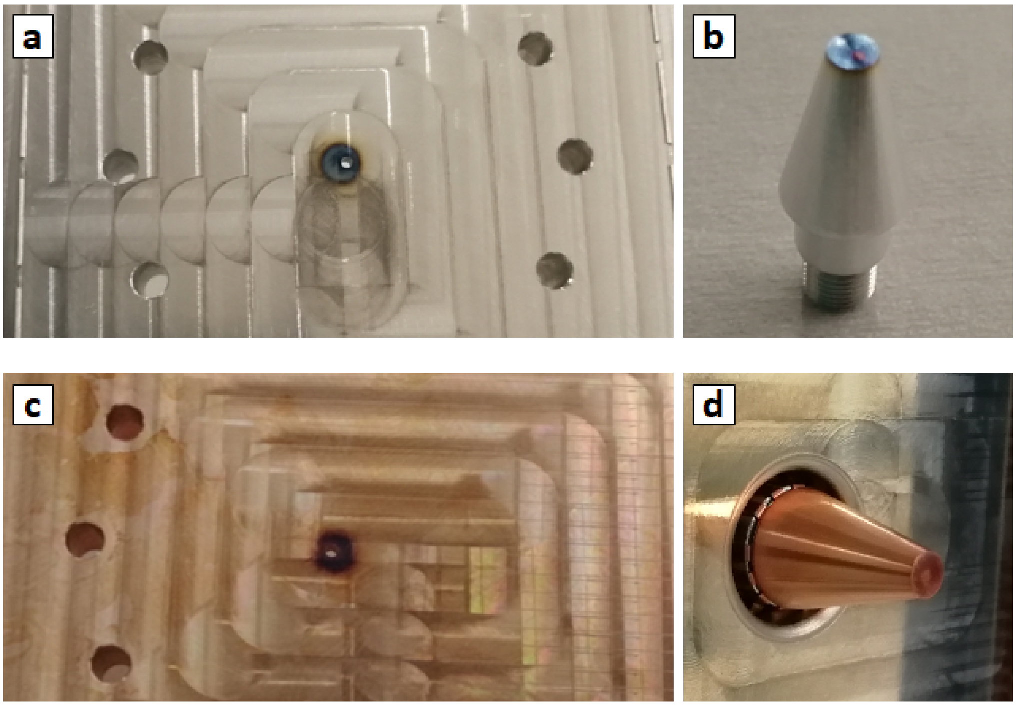

Figure 7.20: Visible effects of permanent electronic discharge on several cathode surfaces, made of aluminium (a,b) and copper (c,d), by continuous resonant multipacting and/or current arcs.

Figures 7.21 (Al & Cu) and 7.22 (Steel) are given to show detailed *I*-*P* curves after CW MEG operation on a relatively small time scale of minutes. Thereby, the respective measurement series are taken directly after continuous multipacting with a time lag of less than 10 seconds between the single measurements, where the power supply is switched off. Each of the presented sets of *I*-*P* characteristics shows variation with further time under operation. For aluminium, where at $d = 0.8$ mm only small currents are generated, the performance in terms of output current is increased. The effect is thereby still measurable until 1.5 hours after the last power transmission. By looking at Figure 7.21b, the I_{out} for copper remains almost unchanged. Small currents in the beginning of each measurement series, together with the relaxation time between single measurements, might be sufficient to regenerate temporary material effects. Also the amount of transmitted power within the CW operation phase seems to be a

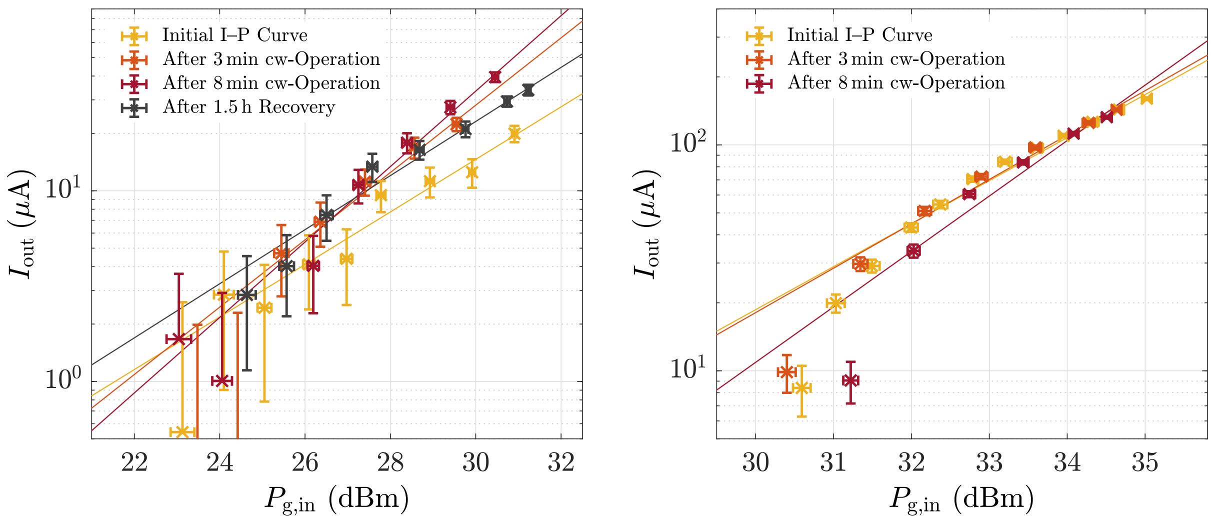

(a) Aluminium, $d = 0.80$ mm

(b) Copper, $d = 1.20$ mm

Figure 7.21: Output current I_{out} as a function of the initially transmitted generator power $P_{g,in}$ for aluminium at $d = 0.8$ mm (a) and copper at $d = 1.2$ mm (b), before and after time under continuous steady state multipacting. The lines indicate exponential fits to the data.

key factor in this regard. However, current degradation is consistently observed for steel (cf. Figure 7.22), where I_{out} is decreased drastically at $d = 1.0$ mm, and not even measurable any more at a small gap size of 0.8 mm, after a 3 min multipacting period. Unfortunately, the studies involving material dependent measurements and continuous operation were realised very late into the whole working process. Dedicated long-term studies including weeks of CW operation are necessary for a deeper understanding of material related effects in an MEG environment.

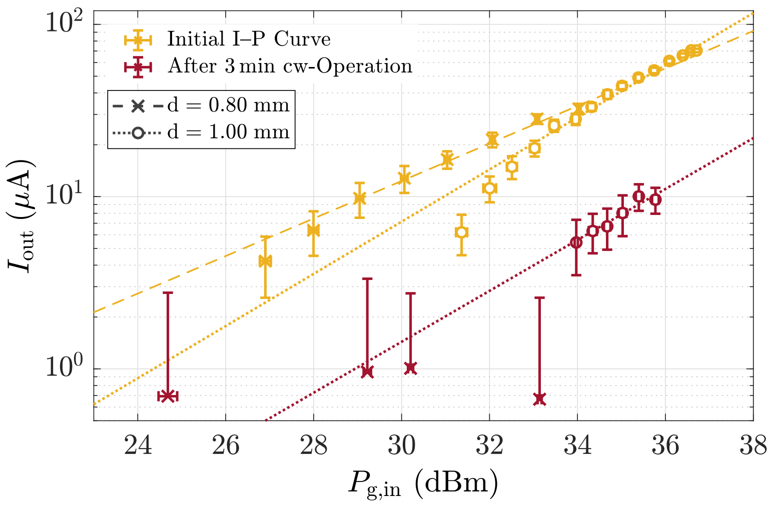

Figure 7.22: Output current I_{out} as a function of the initially transmitted generator power $P_{g,in}$ for stainless steel before and after 3 min under continuous steady state multipacting at $d = 0.8$ and 1.0 mm. Lines illustrate an exponential curve shape once more.

8 Summary and Outlook

In this thesis, we investigated the resonance condition and average output current with a self-developed multipacting electron gun for micro-pulse generation at 2.998 GHz. Thereby, it was possible to successfully operate the MEG either within up to 10μs long RF pulses or under continuous wave operation and show stationary multipacting with less than 10 W initial power supply. Even though measurements regarding the feasibility and quantification of stationary MEG operation were performed at other institutes recently [17, 114], we have developed a unique test setup to characterise emission properties with respect to a wide span of adjustable gap sizes and coupling scenarios.

Congruent with supporting particle tracking simulations are the voltage square dependency of the cavity field during resonant multipacting with increasing cathode distance from 0.65 to 1.75 mm, as well as a consequently increase of the detected multipacting current on average. It is also found that the coupling condition in terms of loaded cavity quality has a major influence on both, the multipacting onset and also the steady state resonance condition, whereby power transmission with $Q_L \simeq 137$ results in a maximum measured output current of $I_{\mathrm{out,m}} \simeq 278\,\mu$A at a large gap size $d = 1.6$ mm. Compared to thermionic DC guns for instance, where currents over 1 A can be achieved [121], this value is relatively small. The advantage of a multipacting gun moreover lies in its substantially lower level of complexity, operating resources and power consumption. From fitting the instantaneous accelerating power as a function of d, constants C_α in regards to power losses could be derived, which are correlated to the coupling strength, but needed further investigation to fully understand their dependencies. However, it is observed that faster cavity filling, relative to the responsive beam loading losses, leads to an overall larger beam current due to the steady state accessibility at higher gap voltages.

Longitudinal energy spectra of the electron bunches could approximately be taken by the application of a retarding potential in beam direction. Results from stationary current measurements indicate increased particle energies with higher cavity gradients and larger cathode distances. Small peak values of 35 to 124 eV furthermore suggest the appearance of higher order multipcating modes. The assumption that also material dependent surface properties are affecting the bunch energy distribution is solidified through consideration of different cathode materials. Thereby, emission from steel generally shows lower particle velocities in comparison to copper and aluminium. From experiments under CW operation it is measured that copper offers the best performance in terms of sheer output, whereby larger currents could be detected at smaller initial field gradients because of a higher unloaded quality factor, and thus faster coupling under similar Q_L. Furthermore, current degradation from continuous electron bombardment on the emission surfaces is lesser pronounced for copper, whereas the beam current from steel cathodes dies out almost completely after several minutes of operation. The degradation effect was found to be recoverable with a similar time constant of minutes in case of copper and aluminium, even thought material damage is implied by considerable surface discolourations.

Future development of more efficient cathode designs including enhanced emission properties can be performed in our experimental setup without much effort. Vast areas of possible improvement are suggested and could be investigated as well. According to [122], additional oxide layers from MgO or GaP, which offer substantially increased maximum SEY of tens to hundreds per incident electron, are enhancing the overall output current density above $1500\,\mathrm{A/cm^2}$. With these coatings they show that multipacting currents may originate from primary electrons over $10\,\mathrm{keV}$ as well, thus implying that an MEG could also be operated far away from the $\delta \simeq 1$ point. By use of much higher generator power in the order of kilowatts, highly energetic electron beams could eventually be produced that way. If more complex or expensive samples including special preparation steps are to be used in our setup, the amount of material could be further reduced by adding an exchangeable part to the aperture plate around the cathode area. Inclusion of exotic emission layers, like CVD diamond [123], or systematic surface treatment in general, would be facilitated in this way. External irradiation for the ignition of resonant multipacting with different surfaces properties can be reconfigured from the outside by use of other light sources, if needed.

A way of generally increasing the overall output current might also be possible through the installation of a voltage controlled variable attenuator to the generator line (R_B in Figure 6.16). The MEG current signal could thereby be used to immediately increase the input power once multipacting sets in and beam loading would be compensated, if the response time of the attenuator was sufficiently small. More power available after the initial charge increase would then generate larger currents at resonance also when the cavity reacts slower for larger Q-values. The framework of long-term characterisation regarding lifetime and performance hereby exists as well, and it is recommended to also perform tests after weeks or months of CW operation, to fully understand the effect of current degradation with respect to the cathode material. Our setup is currently not constructed to achieve UHV conditions. Improvements to the vacuum and creating 10^{-8}-10^{-9} mbar inside pressure could eliminate surface damage from current arcs. Additionally, simulations of higher precision would be beneficial to derive key quantities, by comparison with the empirical findings, more effectively.

For a possible application of the presented MEG as a particle source for accelerators, immediate boosting of the electron velocities, as proposed in [124] for example, is inevitable to avoid bunch blow-up by internal space charge forces. This way, also the transverse phase space could eventually be investigated and the MEG became better comparable to other bunched electron sources in terms of beam quality. In a first approach, our MEG could be installed as an electron source of the universities' test accelerator SALOME (Simple Accelerator for Learning Optics and the Manipulation of Electrons) [125], which already provides necessary elements for transverse beam characterisation measurements.

A Appendix

A.1 ASTRA Input Decks

```
&NEWRUN
  Head='MPGUN '
  RUN=001,
  Distribution = 'dist.dat'
  Lmagnetized=.F
  Lproject_emit=.F
  EmitS=.T
  PhaseS=.T
  T_PhaseS=.T
  Step_width=250,
  Step_max=50000
  DensityS=.F
  TrackS=.T
  CathodeS=.F
  RefS=.T
  Track_All=.T
  Lmonitor=.F
  TcheckS=.T
  Sub_EmitS=.T
  LandFS=.F
  check_ref_part=.F ,
  Z_min=-0.011,
  AUTO_PHASE=F ,
  H_max=0.001 ,
  H_min=0.0 ,
  Max_step=400
  ZSTART=0.00, ZSTOP=2.0
  Zemit=100
  Zphase=100
 /
 &SCAN
  LScan=.F,
  Scan_para='MaxE(1)',
  S_min=-1.5, S_max=-0.8, S_numb=71  ,
  FOM(1)='charge',
  FOM(2)='stat tot ele'
  FOM(3)='stat act'
  FOM(4)='stat sec'
  FOM(5)='length'
  FOM(6)='stat los'
  FOM(7)='mean energy'
  FOM(8)='momentum'
  FOM(9)='rms energy'
  FOM(10)='TOF'
/
```

```
/
 &CHARGE
  Loop=.F,
  LSPCH=.T
  N_min=10
  Nrad=15, Nlong_in=15
  Cell_var=2.0
  min_grid=0.5e-6
  Max_scale=0.1
  Lmirror=.T
 /
 &Aperture
  LApert=.T
  File_Aperture(1)='RAD'
  Ap_Z1(1)=-0.01,    Ap_Z2(1)= 0.0
  Ap_R(1)=-1.4,
  SE_d0(1)=2.0,
  SE_Epm(1)=0.4,
  SE_fs(1)=1.7,
  SE_Tau(1)=0.0,
  SE_Esc(1)=4.0,
  File_Aperture(2)='RAD'
  Ap_Z1(2)=1.2E-3,    Ap_Z2(2)= 3.2E-3
  Ap_R(2)=0.5,
  SE_d0(2)=2.0,
  SE_Epm(2)=0.4,
  SE_fs(2)=1.7,
  SE_Tau(2)=0.0,
  SE_Esc(2)=4.0,
  File_Aperture(3)='RAD'
  Ap_Z1(3)=4.2E-3,    Ap_Z2(3)= 5.2E-3
  Ap_R(3)=-10.0,
  File_Aperture(4)='RAD'
  Ap_Z1(4)=-0.01,    Ap_Z2(4)= 0.0
  Ap_R(4)=1.4,
  File_Aperture(5) = 'walls_10mm.dat'
  Max_Secondary=1E6,
  LClean_Stack=.F
 /
 &CAVITY
  Loop=.F
  LEFieLD=.T,
  FILE_EFieLD(1)='capacitor_field_1.20mm.dat' ,
  MaxE(1)=0.7 ,
  Phi(1)=0.0 ,
  Nue(1)=2.998 ,
  C_pos(1)=0.0  ,
  C_Smooth(1)=20
  T_dependence(1)='fill'
  T_null(1)=106.0
  C_Tau(1)=10.6
  E_stored(1)=4.1E-7
 /
```

Figure A.1: Example of ASTRA input decks for simulations in the MEG default settings.

A.2 Technical Drawings

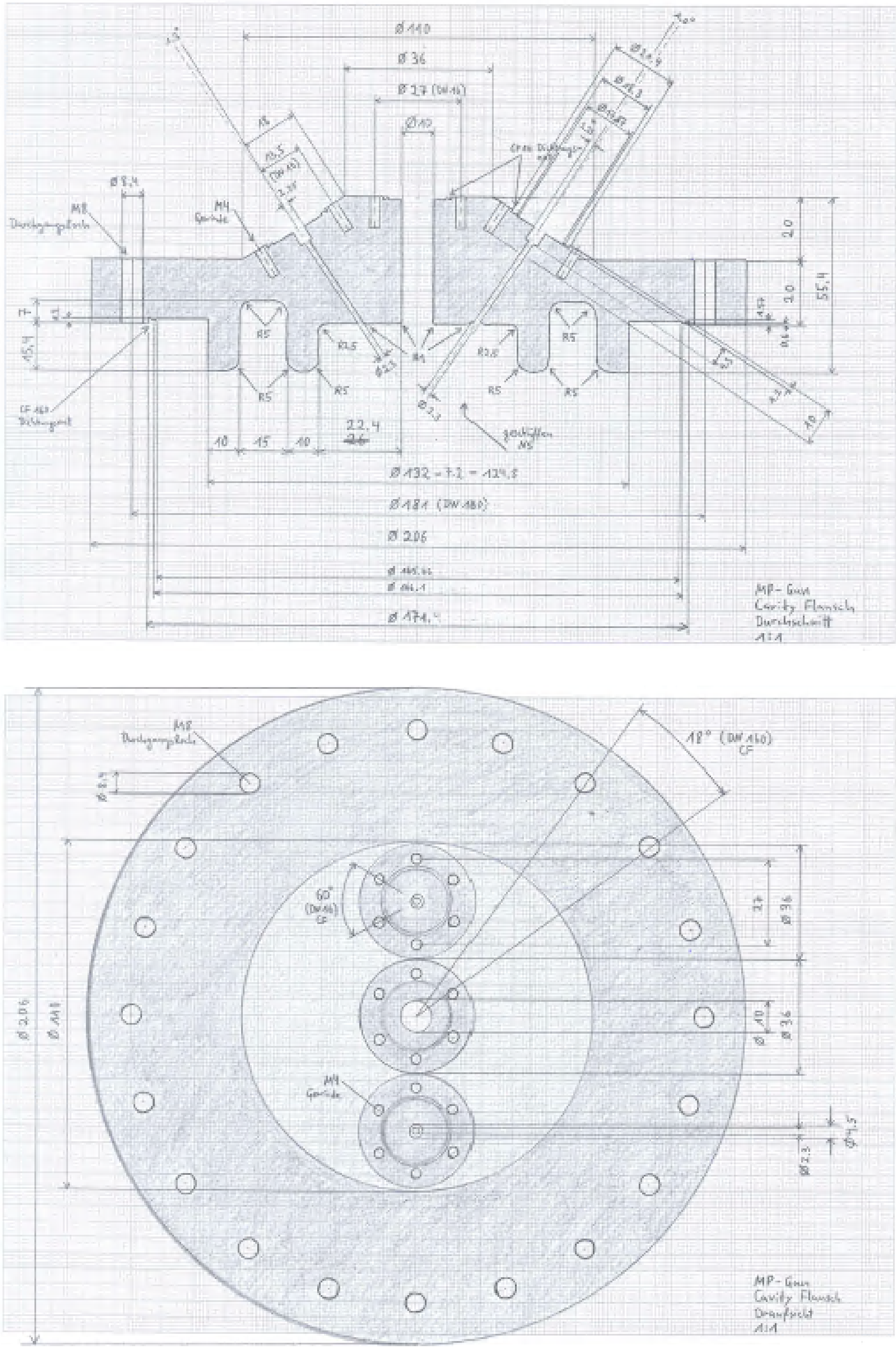

Figure A.2: Supplemental drawings of the prototype cavity design for construction in cross section (top) and top view (bottom).

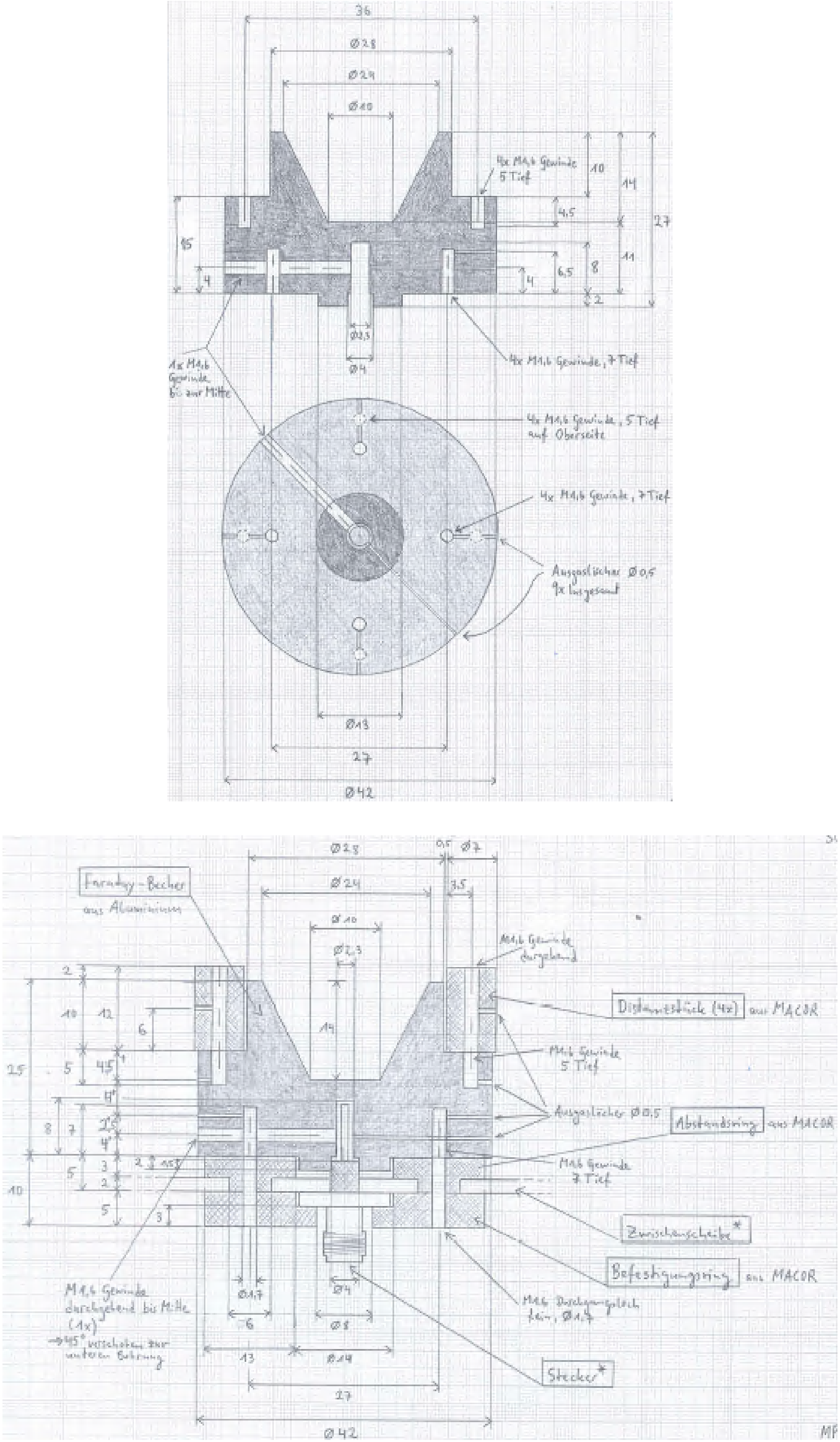

Figure A.3: Supplemental drawings of Faraday Cup (top) and its assembly as a whole (bottom).

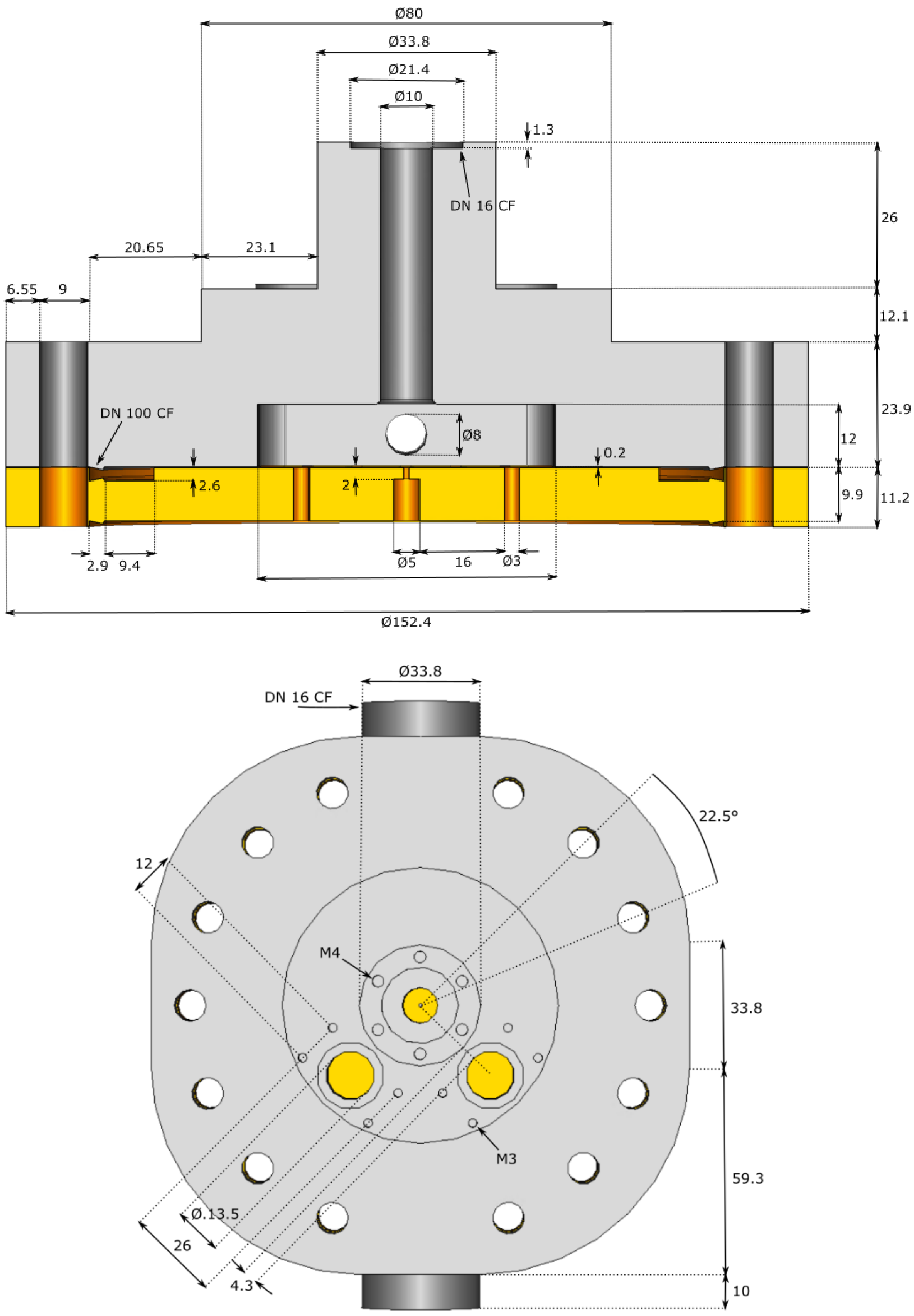

Figure A.4: Cross section (top) and top view (bottom) of the surrounding flange and its opposing aperture plate as part of the main test cavity. The dimensions are millimetre.

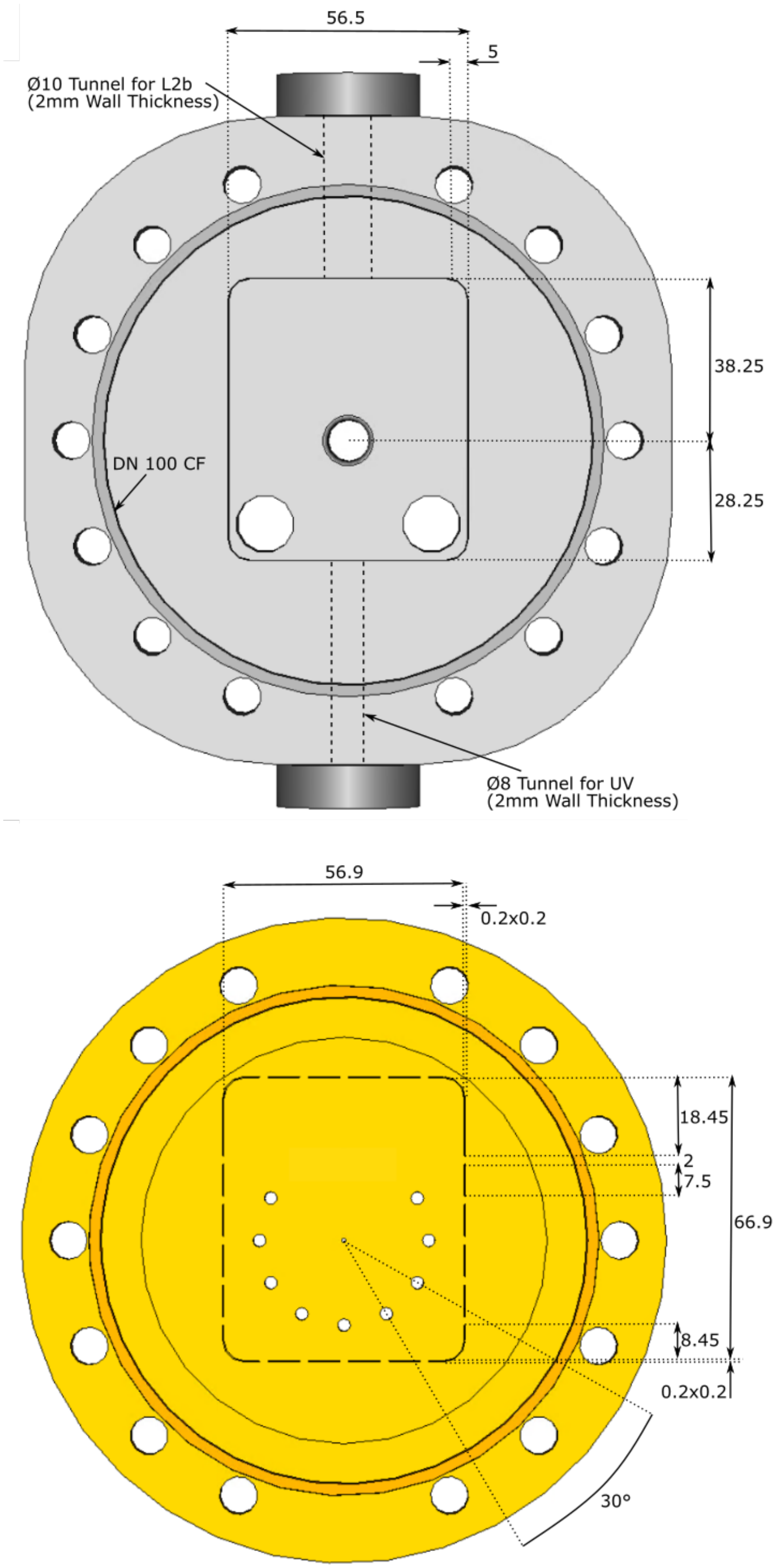

Figure A.5: Rear side of the cavity flange (top) and inner side of the aperture plate (bottom) including a 0.2 x 0.2 mm edge for RF contact at the cavity border.

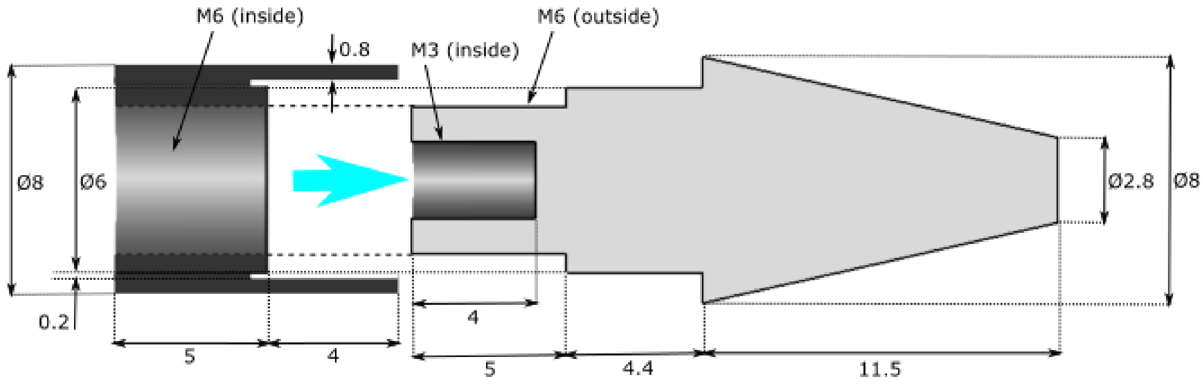

Figure A.6: Cathode plug (right) and adapter (left) as the attachment on translator L1 for the main test cavity. The $CuBe_2$ contact spring is thereby fixed in between.

A.3 Supplemental Data Sets

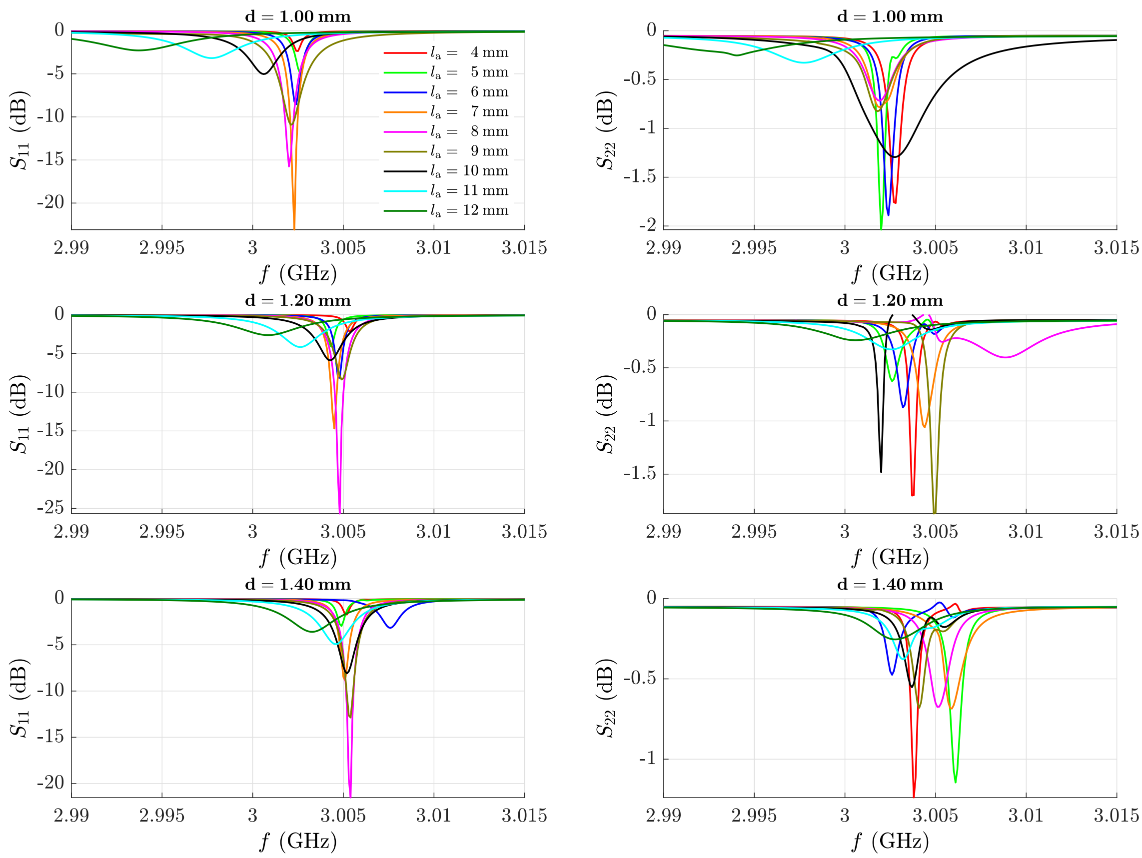

Figure A.7: Magnitude of the reflection coefficients S_{11} (left) and S_{22} (right) from single simulations regarding the results in Figure 6.7.

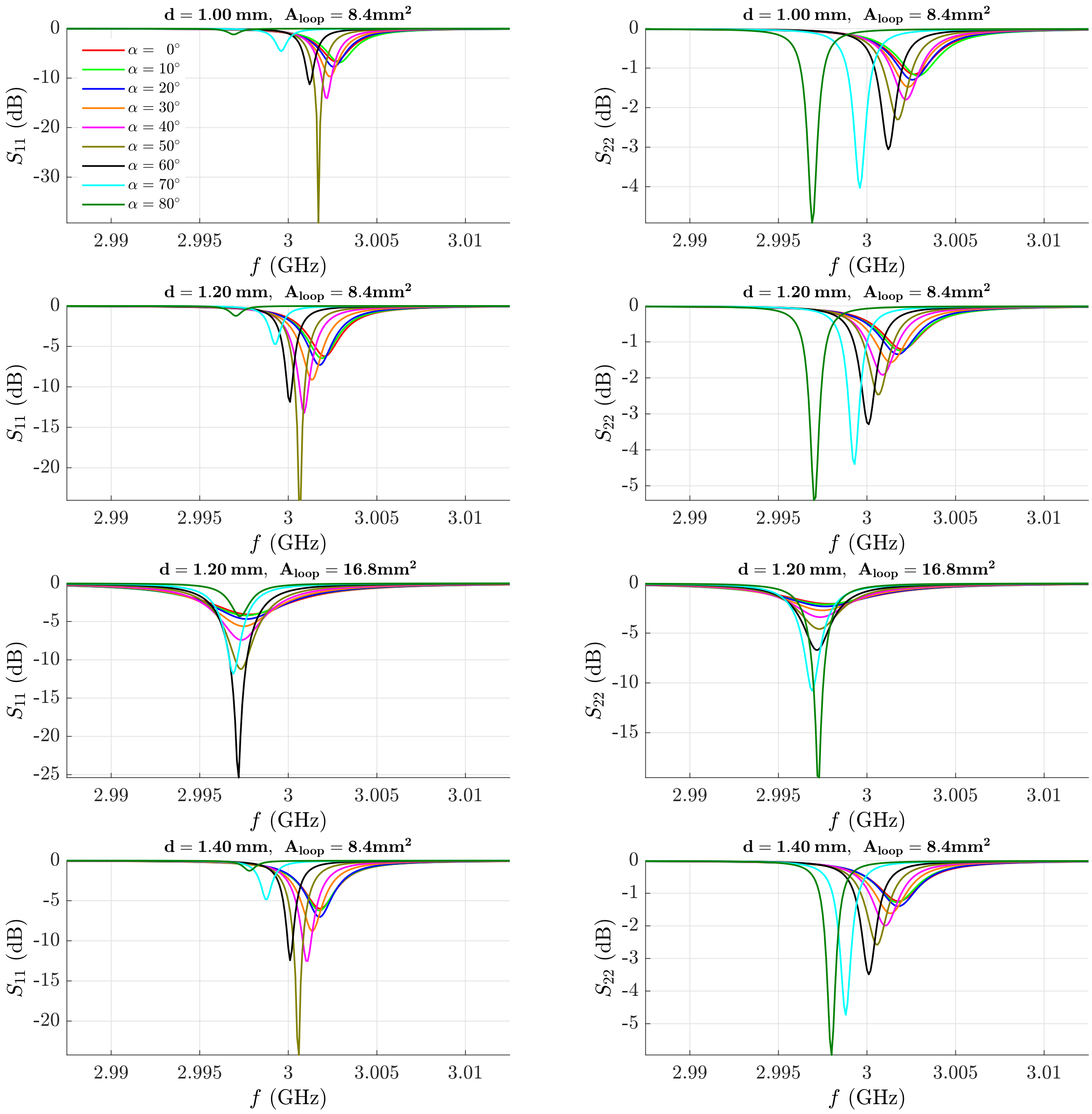

Figure A.8: Magnitude of the reflection coefficients S_{11} (left) and S_{22} (right) from single simulations regarding the results in Figure 6.8.

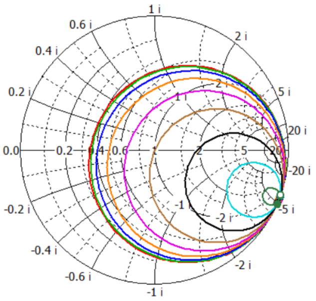

(a) S_{11}, $d = 1.0\,\text{mm}$, $A_{\text{loop}} = 8.4\,\text{mm}^2$

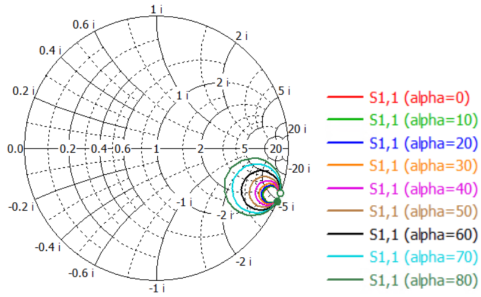

(b) S_{22}

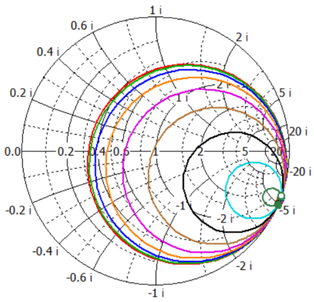

(c) S_{11}, $d = 1.2\,\text{mm}$, $A_{\text{loop}} = 8.4\,\text{mm}^2$

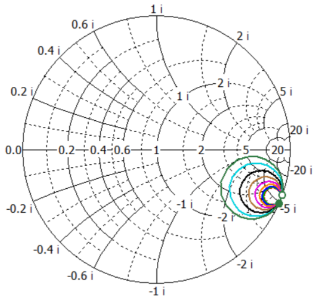

(d) S_{22}

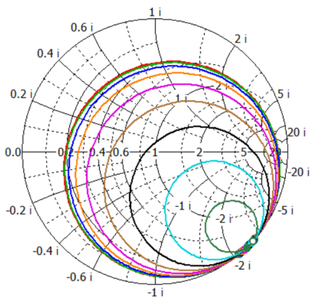

(e) S_{11}, $d = 1.2\,\text{mm}$, $A_{\text{loop}} = 16.8\,\text{mm}^2$

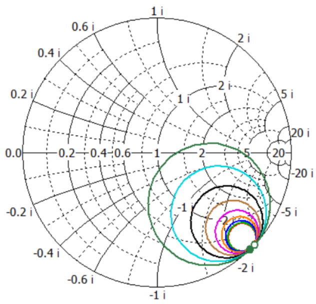

(f) S_{22}

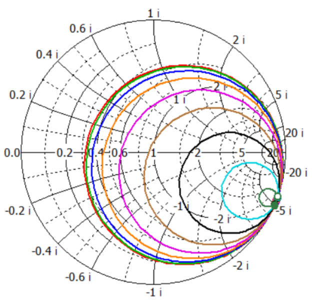

(g) S_{11}, $d = 1.4\,\text{mm}$, $A_{\text{loop}} = 8.4\,\text{mm}^2$

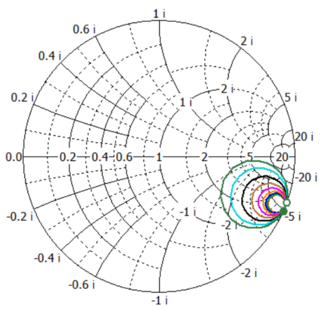

(h) S_{22}

Figure A.9: Smith-charts showing the reflection circles of S_{11} (left) and S_{22} (right) from single simulations regarding the results in Figure 6.8.

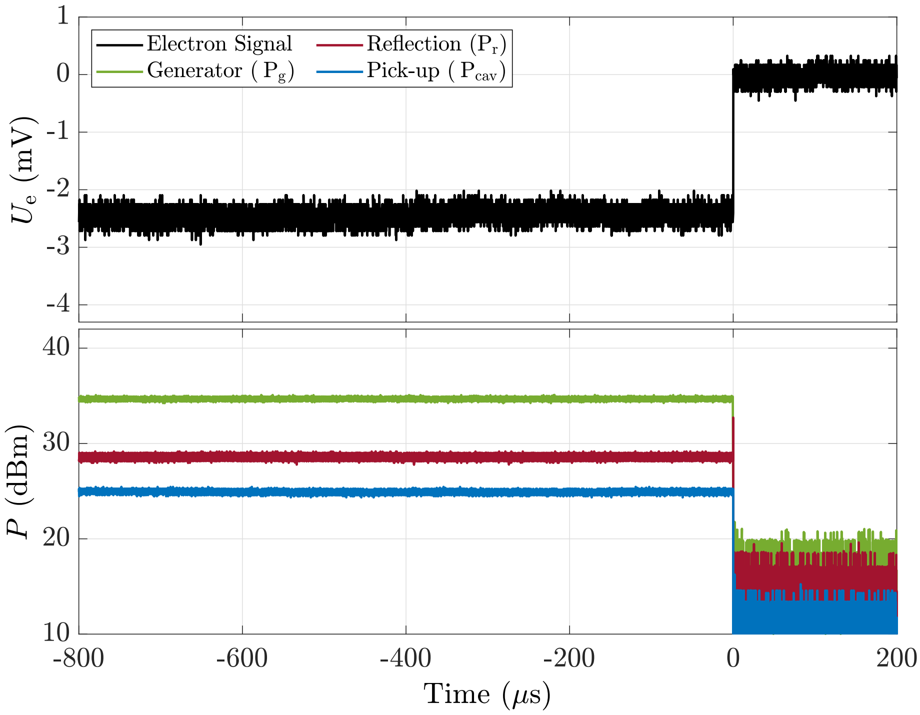

Figure A.10: Exemplary set of MEG measurement data showing the induced voltage U_e of a steady state multipacting current in CW operation with the improved cavity. In the bottom frame, corresponding power signals regarding the forward power amplitude P_g, reflected power P_r and accepted power by the cavity P_{cav} are presented as functions of the same time.

References

[1] P. T. Farnsworth, "Television by electron image scanning", *Journal of the Franklin Institute*, vol. 218, no. 4, pp. 411–444, 1934. DOI:https://doi.org/10.1016/S0016-0032(34)90415-4

[2] W. J. Gallagher, "The multipactor electron gun", *Proceedings of the IEEE*, vol. 57, no. 1, pp. 94–95, 1969. DOI:10.1109/PROC.1969.6886

[3] M. S. Livingston, "Early History of Particle Accelerators**Work done under the auspices of the U.S. Department of Energy.", ser. Advances in Electronics and Electron Physics, L. Marton and C. Marton, Eds. Academic Press, 1980, vol. 50, pp. 1 – 88. DOI:https://doi.org/10.1016/S0065-2539(08)61061-6

[4] R. F. Mould, "The early history of X-ray diagnosis with emphasis on the contributions of physics 1895-1915", *Physics in Medicine and Biology*, vol. 40, no. 11, pp. 1741–1787, 1995. DOI:10.1088/0031-9155/40/11/001

[5] U. Amaldi, *Particle Accelerators: From Big Bang Physics to Hadron Therapy*. Springer, 2015. DOI:10.1007/978-3-319-08870-9

[6] A. W. Chao, K. H. Mess, M. Tigner, and F. Zimmermann, *Handbook of Accelerator Physics and Engineering*, 2nd ed. WORLD SCIENTIFIC, 2013. DOI:10.1142/8543

[7] D. A. Edwards and H. T. Edwards, "Particle Colliders for High Energy Physics", *Reviews of Accelerator Science and Technology*, vol. 01, no. 01, pp. 99–120, 2008. DOI:10.1142/S179362680800006X

[8] J. Rossbach, J. R. Schneider, and W. Wurth, "10 years of pioneering X-ray science at the Free-Electron Laser FLASH at DESY", *Physics Reports*, vol. 808, pp. 1 – 74, 2019, 10 years of pioneering X-ray science at the Free-Electron Laser FLASH at DESY. DOI:https://doi.org/10.1016/j.physrep.2019.02.002

[9] R. Baskar, K. Lee, R. Yeo, and K. Yeoh, "Cancer and radiation therapy: current advances and future directions", *International journal of medical sciences*, vol. 9, no. 3, pp. 193 – 199, 2012. DOI:https://doi.org/10.7150/ijms.3635

[10] P. Musumeci *et al.*, "Advances in bright electron sources", *Nuclear Instruments and Methods in Physics Research Section A: Accelerators, Spectrometers, Detectors and Associated Equipment*, vol. 907, pp. 209–220, 2018, advances in Instrumentation and Experimental Methods (Special Issue in Honour of Kai Siegbahn). DOI:https://doi.org/10.1016/j.nima.2018.03.019

[11] R. Mehnert, "Review of industrial applications of electron accelerators", *Nuclear Instruments and Methods in Physics Research Section B: Beam Interactions with Materials*

and Atoms, vol. 113, no. 1, pp. 81–87, 1996, accelerators in Applied Research and Technology. DOI:https://doi.org/10.1016/0168-583X(95)01344-X

[12] C. Hernandez-Garcia, P. G. O Shea, and M. L. Stutzman, "Electron sources for accelerators", *Physics today*, vol. 61, no. 2, p. 44, 2008. DOI:https://doi.org/10.1063/1.2883909

[13] F. M. Mako and W. Peter, "A high-current micro-pulse electron gun", in *Proceedings of International Conference on Particle Accelerators*, 1993, pp. 2702–2704 vol.4.

[14] S. K. Guharay, L. K. Len, and F. Mako, "High-current micro-pulse electron guns and accelerator applications", in *PACS2001. Proceedings of the 2001 Particle Accelerator Conference (Cat. No.01CH37268)*, vol. 3, 2001, pp. 2084–2086 vol.3. DOI:10.1109/PAC.2001.987284

[15] F. Mako, "Novel particle and radiation sources and advanced materials", *AIP Conference Proceedings*, vol. 1721, no. 1, p. 050001, 2016. DOI:10.1063/1.4944023

[16] L. Liao, M. Zhang, M. Zhao, and Q. Gu, "Novel design of a micro-pulse electron gun", *Nuclear Instruments and Methods in Physics Research Section A: Accelerators, Spectrometers, Detectors and Associated Equipment*, vol. 729, pp. 381–386, 2013. DOI:https://doi.org/10.1016/j.nima.2013.07.064

[17] D. Yang *et al.*, "Design and Research of a Micro-Pulse Electron Gun", in *38th Int. Free Electron Laser Conf.(FEL'17), Santa Fe, NM, USA, August 20-25, 2017*. JACOW, Geneva, Switzerland, 2018, pp. 466–469.

[18] C. Kittel, *Introduction to Solid State Physics*, 8th ed. Wiley, 2004, ISBN 978-0-471-41526-8.

[19] N. W. Ashcroft and N. D. Mermin, *Solid State Physics*. Saunders College, 1976, ISBN 0-03-083993-9 (College Edition).

[20] C. Hugenschmidt, "Positrons in Surface Physics", 2016. DOI:10.1016/j.surfrep.2016.09.002

[21] H. B. Michaelson, "The work function of the elements and its periodicity", *Journal of Applied Physics*, vol. 48, no. 11, pp. 4729–4733, 1977. DOI:10.1063/1.323539

[22] D. M. Trucchi and N. A. Melosh, "Electron-emission materials: Advances, applications, and models", *MRS Bulletin*, vol. 42, no. 7, p. 488–492, 2017. DOI:10.1557/mrs.2017.142

[23] S.-D. Liang, *Quantum Tunneling and Field Electron Emission Theories*. World Scientific, 2014, ISBN 978-9814440219.

[24] C. Herring and M. H. Nichols, "Thermionic Emission", *Rev. Mod. Phys.*, vol. 21, pp. 185–270, 1949. DOI:10.1103/RevModPhys.21.185

[25] O. W. Richardson, *The emission of electricity from hot bodies*. Longmans, Green and Company, 1921.

[26] S. Dushman, "Electron Emission from Metals as a Function of Temperature", *Phys. Rev.*, vol. 21, pp. 623–636, 1923. DOI:10.1103/PhysRev.21.623

[27] M. Reiser, *Theory and Design of Charged Particle Beams*, 2nd ed. John Wiley & Sons, Ltd, 2008. DOI:https://doi.org/10.1002/9783527622047

[28] J. W. Lewellen and J. Noonan, "Field-emission cathode gating for rf electron guns", *Phys. Rev. ST Accel. Beams*, vol. 8, p. 033502, 2005. DOI:10.1103/PhysRevSTAB.8.033502

[29] E. W. Müller, "Elektronenmikroskopische Beobachtungen von Feldkathoden", *Zeitschrift für Physik*, vol. 106, no. 9-10, pp. 541–550, 1937. DOI:https://doi.org/10.1007/BF01339895

[30] R. H. Fowler and L. Nordheim, "Electron emission in intense electric fields", *Proceedings of the Royal Society of London. Series A, Containing Papers of a Mathematical and Physical Character*, vol. 119, no. 781, pp. 173–181, 1928. DOI:10.1098/rspa.1928.0091

[31] W. Schottky, "Über kalte und warme Elektronenentladungen", *Z. Physik*, vol. 14, pp. 63–106, 1923. DOI:10.1007/BF01340034

[32] R. G. Forbes, "Simple good approximations for the special elliptic functions in standard Fowler-Nordheim tunneling theory for a Schottky-Nordheim barrier", *Applied Physics Letters*, vol. 89, no. 11, p. 113122, 2006. DOI:10.1063/1.2354582

[33] J.-H. Han, "Dynamics of Electron Beam and Dark Current in the Photocathode RF Guns", 2005, Ph.D. Thesis.

[34] J. W. Wang and G. A. Loew, "Field emission and rf breakdown in high-gradient room temperature linac structures". DOI:10.2172/663321

[35] F. Wooten, *Optical properties of solids*. Academic press, 1972.

[36] A. Einstein, "Über einen die Erzeugung und Verwandlung des Lichtes betreffenden heuristischen Gesichtspunkt", *Annalen der Physik*, vol. 322, no. 6, pp. 132–148, 1905. DOI:10.1002/andp.19053220607

[37] W. Spicer and A. Herrera-Gómez, "Modern theory and applications of photocathodes. SLAC-Pub 6306", 1993.

[38] R. A. Powell, W. E. Spicer, G. B. Fisher, and P. Gregory, "Photoemission Studies of Cesium Telluride", *Phys. Rev. B*, vol. 8, pp. 3987–3995, 1973. DOI:10.1103/PhysRevB.8.3987

[39] J. S. Fraser, R. L. Sheffield, E. R. Gray, and G. W. Rodenz, "High-Brightness Photoemitier Injector for Electron Accelerators", *IEEE Transactions on Nuclear Science*, vol. 32, no. 5, pp. 1791–1793, 1985.

[40] A. Arnold and J. Teichert, "Overview of Superconducting Photoinjectors", *Physical Review Special Topics - Accelerators and Beams*, vol. 14, 2011. DOI:10.1103/PhysRevSTAB.14.024801

[41] K. Batchelor *et al.*, "Performance of the Brookhaven photocathode rf gun", *Nuclear Instruments and Methods in Physics Research Section A: Accelerators, Spectrometers, Detectors and Associated Equipment*, vol. 318, no. 1, pp. 372 – 376, 1992. DOI:https://doi.org/10.1016/0168-9002(92)91084-M

[42] P. Michelato, "Photocathodes for RF photoinjectors", *Nuclear Instruments and Methods in Physics Research Section A: Accelerators, Spectrometers, Detectors and Associated Equipment*, vol. 393, no. 1, pp. 455 – 459, 1997, free Electron Lasers 1996. DOI:https://doi.org/10.1016/S0168-9002(97)00545-7

[43] F. Stephan *et al.*, "Detailed characterization of electron sources yielding first demonstration of European X-ray Free-Electron Laser beam quality", *Phys. Rev. ST Accel. Beams*, vol. 13, p. 020704, 2010. DOI:10.1103/PhysRevSTAB.13.020704

[44] J.-H. Han, K. Flöttmann, and W. Hartung, "Single-side electron multipacting at the photocathode in rf guns", *Phys. Rev. ST Accel. Beams*, vol. 11, p. 013501, 2008. DOI:10.1103/PhysRevSTAB.11.013501

[45] E. L. Murphy and R. H. Good, "Thermionic Emission, Field Emission, and the Transition Region", *Phys. Rev.*, vol. 102, pp. 1464–1473, 1956. DOI:10.1103/PhysRev.102.1464

[46] H. Chen *et al.*, "Surface-Emission Studies in a High-Field RF Gun based on Measurements of Field Emission and Schottky-Enabled Photoemission", *Phys. Rev. Lett.*, vol. 109, p. 204802, 2012. DOI:10.1103/PhysRevLett.109.204802

[47] Z. M. Yusof, M. E. Conde, and W. Gai, "Schottky-Enabled Photoemission in a rf Accelerator Photoinjector: Possible Generation of Ultralow Transverse Thermal-Emittance Electron Beam", *Phys. Rev. Lett.*, vol. 93, p. 114801, 2004. DOI:10.1103/PhysRevLett.93.114801

[48] A. Dekker, "Secondary Electron Emission", in *Advances in Research and Applications*, ser. Solid State Physics, F. Seitz and D. Turnbull, Eds. Academic Press, 1958, vol. 6, pp. 251 – 311. DOI:https://doi.org/10.1016/S0081-1947(08)60728-6

[49] L. Austin and H. Starke, "Über die Reflexion der Kathodenstrahlen und eine damit verbundene neue Erscheinung secundärer Emission", *Annalen der Physik*, vol. 314, no. 10, pp. 271–292, 1902. DOI:10.1002/andp.19023141003

[50] M. A. Furman and M. T. F. Pivi, “Probabilistic model for the simulation of secondary electron emission”, *Phys. Rev. ST Accel. Beams*, vol. 5, p. 124404, 2002. DOI:10.1103/PhysRevSTAB.5.124404

[51] A. Shih, J. Yater, C. Hor, and R. Abrams, “Secondary electron emission studies”, *Applied Surface Science*, vol. 111, pp. 251 – 258, 1997, proceedings of the International Vacuum Electron Sources Conference ’96. DOI:https://doi.org/10.1016/S0169-4332(96)00729-5

[52] G. F. Dionne, “Origin of secondary-electron-emission yield-curve parameters”, *Journal of Applied Physics*, vol. 46, no. 8, pp. 3347–3351, 1975. DOI:10.1063/1.322061

[53] V. Baglin *et al.*, “The Secondary Electron Yield of Technical Materials and its Variation with Surface Treatments”, in *7th European Particle Accelerator Conference (EPAC 2000)*, no. LHC-Project-Report-433. CERN-LHC-Project-Report-433, 2000, p. 6, https://cds.cern.ch/record/466534.

[54] H. Seiler, “Secondary electron emission in the scanning electron microscope”, *Journal of Applied Physics*, vol. 54, no. 11, pp. R1–R18, 1983. DOI:10.1063/1.332840

[55] J. R. Young, “Penetration of Electrons in Aluminum Oxide Films”, *Phys. Rev.*, vol. 103, pp. 292–293, 1956. DOI:10.1103/PhysRev.103.292

[56] Y. Lin and D. C. Joy, “A new examination of secondary electron yield data”, *Surface and Interface Analysis*, vol. 37, no. 11, pp. 895–900. DOI:10.1002/sia.2107

[57] E. M. Baroody, “A Theory of Secondary Electron Emission from Metals”, *Phys. Rev.*, vol. 78, pp. 780–787, 1950. DOI:10.1103/PhysRev.78.780

[58] J. R. M. Vaughan, “Multipactor”, *IEEE Transactions on Electron Devices*, vol. 35, no. 7, pp. 1172–1180, 1988. DOI:10.1109/16.3387

[59] A. J. Hatch and H. B. Williams, “Multipacting Modes of High-Frequency Gaseous Breakdown”, *Phys. Rev.*, vol. 112, pp. 681–685, 1958. DOI:10.1103/PhysRev.112.681

[60] Lay-Kee Ang, Y. Y. Lau, R. A. Kishek, and R. M. Gilgenbach, “Power deposited on a dielectric by multipactor”, *IEEE Transactions on Plasma Science*, vol. 26, no. 3, pp. 290–295, 1998. DOI:10.1109/27.700756

[61] E. Somersalo, D. Proch, P. Ylä-Oijala, and J. Sarvas, “Computational methods for analyzing electron multipacting in RF structures”, *Part. Accel.*, vol. 59, pp. 107–141, 1998.

[62] R. A. Kishek and Y. Y. Lau, “Multipactor Discharge on a Dielectric”, *Phys. Rev. Lett.*, vol. 80, pp. 193–196, 1998. DOI:10.1103/PhysRevLett.80.193

[63] J. H. Han, M. Krasilnikov, and K. Flöttmann, “Secondary electron emission in a photocathode rf gun”, *Phys. Rev. ST Accel. Beams*, vol. 8, p. 033501, 2005. DOI:10.1103/PhysRevSTAB.8.033501

[64] R. A. Kishek, Y. Y. Lau, L. K. Ang, A. Valfells, and R. M. Gilgenbach, “Multipactor discharge on metals and dielectrics: Historical review and recent theories”, *Physics of Plasmas*, vol. 5, no. 5, pp. 2120–2126, 1998. DOI:10.1063/1.872883

[65] L. K. Len and F. M. Mako, “Self-bunching electron guns”, in *Proceedings of the 1999 Particle Accelerator Conference (Cat. No.99CH36366)*, vol. 1, 1999, pp. 70–74 vol.1.

[66] J. D. Jackson, *Classical Electrodynamics*, 3rd ed. Wiley, ’98, ISBN 978-0-471-30932-1.

[67] H. Wiedemann, *Particle accelerator physics*, 4th ed. Springer, 2015. DOI:10.1007/978-3-319-18317-6

[68] K. Wille, *Physik der Teilchenbeschleuniger und Synchrotronstrahlungsquellen*, 2nd ed. Teubner, 1996, ISBN 978-3-519-13087-4.

[69] G. Dôme, “RF Engineering for Particle Accelerators: RF Theory”, *Proc. CAS CERN Accelerator School*, vol. 1, pp. 1–74, 1992. DOI:https://doi.org/10.5170/CERN-1992-003

[70] J. Holzbauer, “RF Theory and Design-Notes”, *US Particle Accelerator School, Grand Rapids*, 2012, https://uspas.fnal.gov/materials/12MSU/RF_Design_Lecture_Notes.pdf.

[71] J. W. Nilsson and S. Riedel, *Electric Circuits*, 9th ed. USA: Prentice Hall Press, 2010, ISBN 978-0136114994.

[72] R. Yorke, *Electric Circuit Theory: Applied Electricity and Electronics*, 1st ed., P. Hammond, Ed. Elsevier, 1981. DOI:https://doi.org/10.1016/C2013-0-03407-X

[73] E. Jensen, “RF Cavity Design”, pp. 405–429, 2014, contribution to the CAS - CERN Accelerator School: Advanced Accelerator Physics Course, Trondheim, Norway, 18-29 Aug 2013. DOI:https://doi.org/10.5170/CERN-2014-009.405

[74] H. Klein, “RF Engineering for Particle Accelerators: Basic Concepts I”, *Proc. CAS CERN Accelerator School*, vol. 1, pp. 97–122, 1992. DOI:https://doi.org/10.5170/CERN-1992-003

[75] T. P. Wangler, *RF Linear accelerators*, 2nd ed. John Wiley & Sons, 2008. DOI:https://doi.org/10.1002/9783527623426

[76] D. Alesini, “Power coupling”, pp. 125–147, 2011, contribution to the CAS - CERN Accelerator School: Specialised Course on RF for Accelerators; 8 - 17 Jun 2010, Ebeltoft, Denmark. DOI:https://doi.org/10.5170/CERN-2011-007.125

[77] J. Gao, “Analytical formula for the coupling coefficient β of a cavity-waveguide coupling system”, *Nuclear Instruments and Methods in Physics Research Section A: Accelerators, Spectrometers, Detectors and Associated Equipment*, vol. 309, no. 1, pp. 5 – 10, 1991. DOI:https://doi.org/10.1016/0168-9002(91)90085-5

[78] A. Gamp, "RF Engineering for Particle Accelerators: Servo Control of RF cavities under beam loading", *Proc. CAS CERN Accelerator School*, vol. 1, pp. 396–415, 1992. DOI:https://doi.org/10.5170/CERN-1992-003

[79] P. B. Wilson and J. E. Griffin, "High energy electron linacs; application to storage ring RF systems and linear colliders", *AIP Conf. Proc.; (United States)*, vol. 87, pp. 450–555, 1982. DOI:10.1063/1.33620

[80] R. Garoby, "Beam loading in rf cavities", *Lect. Notes Phys.*, vol. 400, no. CERN-PS-91-33-RF, pp. 509–541. 34 p, 1991. DOI:10.1007/3-540-55250-2 42

[81] J. E. Leiss, "Beam Loading in Linear Accelerators", *IEEE Transactions on Nuclear Science*, vol. 12, no. 3, pp. 566–579, 1965. DOI:10.1109/TNS.1965.4323696

[82] J. Zhao *et al.*, "Theoretical analysis and simulation of the influence of self-bunching effects and longitudinal space charge effects on the propagation of keV electron bunch produced by a novel S-band Micro-Pulse electron Gun", *AIP Advances*, vol. 6, no. 6, p. 065327, 2016. DOI:10.1063/1.4955144

[83] F. M. Mako and L. K. Len, "Self-bunching electron guns", *AIP Conference Proceedings*, vol. 474, no. 1, pp. 41–50, 1999. DOI:10.1063/1.59030

[84] D. Yang *et al.*, "Study on the maximum stable output of a novel s-band micro-pulse electron gun", *AIP Advances*, vol. 8, no. 7, p. 075313, 2018. DOI:10.1063/1.5028150

[85] Z. Kui, L. Xiangyang, Q. Shengwen, Z. Jifei, L. Xing, and Y. Ziqin, "Study on the steady operating state of a micro-pulse electron gun", *Review of Scientific Instruments*, vol. 85, no. 9, p. 093304, 2014. DOI:10.1063/1.4895604

[86] A. L. Gilardini, "Multipacting discharges: Constant-k theory and simulation results", *Journal of Applied Physics*, vol. 78, no. 2, pp. 783–795, 1995. DOI:10.1063/1.360336

[87] F. Tecker, "Longitudinal Beam Dynamics", 2016. DOI:10.5174/CERN-2014-009.1

[88] S. Riyopoulos, D. Chernin, and D. Dialetis, "Effect of random secondary delay times and emission velocities in electron multipactors", *IEEE Transactions on Electron Devices*, vol. 44, no. 3, pp. 489–497, 1997. DOI:10.1109/16.556160

[89] R. Kishek and Y. Y. Lau, "Interaction of Multipactor Discharge and rf Circuit", *Phys. Rev. Lett.*, vol. 75, pp. 1218–1221, 1995. DOI:10.1103/PhysRevLett.75.1218

[90] R. A. Kishek, Y. Y. Lau, and D. Chernin, "Steady state multipactor and dependence on material properties", *Physics of Plasmas*, vol. 4, no. 3, pp. 863–872, 1997. DOI:10.1063/1.872177

[91] C. D. Child, “Discharge From Hot CaO”, *Phys. Rev. (Series I)*, vol. 32, pp. 492–511, 1911. DOI:10.1103/PhysRevSeriesI.32.492

[92] I. Langmuir, “The Effect of Space Charge and Residual Gases on Thermionic Currents in High Vacuum”, *Phys. Rev.*, vol. 2, pp. 450–486, 1913. DOI:10.1103/PhysRev.2.450

[93] N. Chauvin, “Space-Charge Effect”, no. arXiv:1410.7991, pp. 63–83. 21 p, 2014, contribution to the CAS-CERN Accelerator School: Ion Sources, Senec, Slovakia, 29 May - 8 June 2012, edited by R. Bailey. DOI:10.5170/CERN-2013-007.63

[94] K. Schindl, “Space charge”, 2006. DOI:10.5170/CERN-2006-002.305

[95] K. Floettmann, “Private communication”, 2021.

[96] J. W. Luginsland, Y. Y. Lau, R. J. Umstattd, and J. J. Watrous, “Beyond the Child–Langmuir law: A review of recent results on multidimensional space-charge-limited flow”, *Physics of Plasmas*, vol. 9, no. 5, pp. 2371–2376, 2002. DOI:10.1063/1.1459453

[97] S. Riyopoulos, D. Chernin, and D. Dialetis, “Theory of electron multipactor in crossed fields”, *Physics of Plasmas*, vol. 2, no. 8, pp. 3194–3213, 1995. DOI:10.1063/1.871151

[98] R. A. Kishek and Y. Y. Lau, “A novel phase focusing mechanism in multipactor discharge”, *Physics of Plasmas*, vol. 3, no. 5, pp. 1481–1483, 1996. DOI:10.1063/1.872027

[99] K. Floettmann, “A Space Charge Tracking Algorithm”, Hamburg, Germany, Mar. 2017, Version 3.2, http://www.desy.de/ mpyflo/Astra_manual/Astra-Manual_V3.2.pdf.

[100] C. Runge, “Über die numerische Auflösung von Differentialgleichungen”, *Math. Ann.*, vol. 4, pp. 167–178, 1895. DOI:10.1007/BF01446807

[101] W. Kutta, “Beitrag zur Näherungsweisen Integration Totaler Differentialgleichungen”, *Z. Math. Phys.*, vol. 46, pp. 435–453, 1901.

[102] J. C. Butcher, “Implicit Runge-Kutta Processes”, *Math. Comp.*, vol. 18, pp. 50–64, 1964. DOI:10.1090/S0025-5718-1964-0159424-9

[103] R. A. Kishek, “Ping-Pong Modes: A New Form of Multipactor”, *Phys. Rev. Lett.*, vol. 108, p. 035003, 2012. DOI:10.1103/PhysRevLett.108.035003

[104] L. Liao, M. Zhang, and M.-H. Zhao, “Multipacting saturation in parallel plate and micro-pulse electron gun”, vol. 39, no. 2, p. 027003, 2015. DOI:10.1088/1674-1137/39/2/027003

[105] C. Henkel, K. Flöttmann, W. Hillert, and V. Miltchev, “Design Studies of an S-Band Multipacting Electron Gun”, in *9th International Particle Accelerator Conference*, 2018, p. THPML054. DOI:10.18429/JACoW-IPAC2018-THPML054

[106] CST, “Microwave studio”, 2021, http://www.cst.com.

[107] K.-J. Bathe, *Finite Element Method*. American Cancer Society, 2008. DOI:https://doi.org/10.1002/9780470050118.ecse159

[108] L. Young, “Optimum Quarter-Wave Transformers”, *IRE Transactions on Microwave Theory and Techniques*, vol. 8, no. 5, pp. 478–482, 1960. DOI:10.1109/TMTT.1960.1124774

[109] F. Caspers, “RF engineering basic concepts: S-parameters”, pp. 67–93, 2012, Contribution to the CAS - CERN Accelerator School: Specialised Course on RF for Accelerators; 8 - 17 Jun 2010, Ebeltoft, Denmark. DOI:10.5170/CERN-2011-007.67

[110] “Microwave amps”, 2021, http://www.microwaveamps.co.uk.

[111] P. H. Smith, *Electronic applications of the Smith Chart in waveguide, circuit, and component analysis*. New York, NY: McGraw-Hill, 1970, https://cds.cern.ch/record/103989.

[112] F. Caspers, “RF engineering basic concepts: the Smith chart”, pp. 95–116, 2012, Contribution to the CAS - CERN Accelerator School: Specialised Course on RF for Accelerators; 8 - 17 Jun 2010, Ebeltoft, Denmark. DOI:10.5170/CERN-2011-007.95

[113] C. Henkel, K. Flöttmann, W. Hillert, and V. Miltchev, “Characterization of an Electron Gun Test Setup Based on Multipacting”, in *Proc. 10th International Particle Accelerator Conference (IPAC’19), Melbourne, Australia, 19-24 May 2019*, ser. International Particle Accelerator Conference, no. 10. JACoW Publishing, 2019, pp. 1961–1963. DOI:doi:10.18429/JACoW-IPAC2019-TUPTS013

[114] B. Li *et al.*, “The first energy spread measurement of electron beam produced by MPG”, *Results in Physics*, vol. 7, pp. 3984 – 3990, 2017. DOI:https://doi.org/10.1016/j.rinp.2017.10.030

[115] H. A. Wheeler, “Formulas for the Skin Effect”, *Proceedings of the IRE*, vol. 30, no. 9, pp. 412–424, 1942. DOI:10.1109/JRPROC.1942.232015

[116] L. E. McAllister, “Secondary Electron Emission from Copper and Copper Oxide Surfaces”, *Phys. Rev.*, vol. 21, pp. 122–130, 1923. DOI:10.1103/PhysRev.21.122

[117] R. Cimino *et al.*, “Nature of the Decrease of the Secondary-Electron Yield by Electron Bombardment and its Energy Dependence”, *Phys. Rev. Lett.*, vol. 109, p. 064801, 2012. DOI:10.1103/PhysRevLett.109.064801

[118] R. Valizadeh, O. B. Malyshev, S. Wang, S. A. Zolotovskaya, W. Allan Gillespie, and A. Abdolvand, “Low secondary electron yield engineered surface for electron cloud mitigation”, *Applied Physics Letters*, vol. 105, no. 23, p. 231605, 2014. DOI:10.1063/1.4902993

[119] S. Wang, “Secondary electron yield measurements of anti-multipacting surfaces for accelerators”, Ph.D. dissertation, Loughborough University, 2016.

[120] J. Tuckmantel *et al.*, “Improvements to power couplers for the LEP2 superconducting cavities”, in *Proceedings Particle Accelerator Conference*, vol. 3, 1995, pp. 1642–1644 vol.3. DOI:10.1109/PAC.1995.505313

[121] K. Togawa *et al.*, “CeB_6 electron gun for low-emittance injector”, *Phys. Rev. ST Accel. Beams*, vol. 10, p. 020703, 2007. DOI:10.1103/PhysRevSTAB.10.020703

[122] J. A. Nation *et al.*, “Advances in cold cathode physics and technology”, *Proceedings of the IEEE*, vol. 87, no. 5, pp. 865–889, 1999. DOI:10.1109/5.757258

[123] J. Zhai, C. Tang, and S. Zheng, “Multipactor electron gun with CVD diamond cathodes”, in *Epac*, vol. 6, 2006, p. 3203.

[124] M. Zhong, S. Zheng, and C. Tang, “The primary experiment of multipactor electron-gun-based accelerator”, *Proc. PAC’09*, 2009.

[125] V. Miltchev, D. Riebesehl, J. Roßbach, M. Trunk, and O. Stein, “SALOME: An Accelerator for the Practical Course in Accelerator Physics”, p. WEPRO114. 3 p, 2014.

Acknowledgments

First of all I would like to thank Prof. Dr. Wolfgang Hillert for the opportunity to work on this interesting topic, the great supervision of my work in general and serving as a role model in terms of guidance and teaching. Moreover, I would like to thank Dr. Klaus Flöttmann for helpful advice at any time and the introduction to a valuable network of people at DESY. A big thank you also to Dr. Velizar Miltchev for his support and proofreading of my thesis. Their inspiring influence throughout many discussions made this work to what it is.

Furthermore, this work would not have been possible without the provision of great scientific infrastructure of both, Universität Hamburg and DESY. Special thanks are thereby given to Stephan Fleig and his team from the mechanical workshop, who did a good job in fabricating crucial parts of my setup, Gerd Tews, who helped with the commissioning of the gun, and also Michaela Marx, who assisted me with IT related issues and introduced me to the CST software. I also thank Fenna Reinholdt for her patient guidance through several bureaucratic procedures.

For providing very valuable courses and assisting PhD students in most situations I would like to thank the PIER Helmholtz Graduate School including its coordinators Stefanie Tepass and Mirko Siemssen. I am also very thankful due to many engaged PhD students contributing to the Doktorandeninitiative DOIT, who stand up for the needs of their fellow students and organise social events for all of us to have a great time.

I really enjoyed this special time thanks to all my friends and colleagues in office and around campus, Philipp Amstutz, Immo Bahns, Andrea Bellandi, Dr. Vanessa Grattoni, Max Kellermeier, Dr. Willi Kuropka, Dr. Christoph Lechner, Patrick Rauer, Jan Oliver Rieger, Dr. Mathias Vogt, and many more! Especially Dr. Florian Christie, who also encouraged me to start working in accelerator physics in the first place.

Last but not least, I am very greatful for all the support and encouragement from my friends and family, especially my fiancée Svenja, who was there for me with love and patience during these challenging times.

Eidesstattliche Versicherung

Hiermit versichere ich an Eides statt, die vorliegende Dissertationsschrift selbst verfasst und keine anderen als die angegebenen Hilfsmittel und Quellen benutzt zu haben.

Die eingereichte schriftliche Fassung entspricht der auf dem elektronischen Speichermedium.

Die Dissertation wurde in der vorgelegten oder einer ähnlichen Form nicht schon einmal in einem früheren Promotionsverfahren angenommen oder als ungenügend beurteilt.

Hamburg, 14. Juli 2021

Christian Henkel